Effect of Kawrgosk Oil Refinery on Some Physicochemical Characteristics, Microbial Population and Biochemical Properties of Surface Soils

Nashmeel Saeed Khudhur

Department of Environmental Science, College of Science, University of Salahaddin, Kurdistan Region, Iraq.

A R T I C L E   I N F O

A B S T R A C T

Effect of Kawrgosk Oil Refinery byproducts on physicochemical, microbiological and certain soil enzymes was studied. Contamination of the Refinery affected physicochemical, biological and enzymatic properties of soil. Soil pH slightly increased to 8.42 ± 0.173, moisture content and organic matter were significantly lower than control 0.84 ± 0.116 % and 15.04 ± 0.301 g.Kg^{-1} respectively. Refinery contamination caused reduction in bacterial population to 0.04×10^7 cfu.g^{-1} dry soil and fungal population to 2×10^3 cfu.g^{-1} dry soil and reduced dehydrogenase activity to 0.020 TPF µg.g^{-1} when compared to control. Whereas, the Refinery contamination was increased oil residue to 2.6 ± 0.000 µg.kg^{-1}, Fe to 31.50 ± 0.433 g.kg^{-1}, Ni to 0.116 ± 0.002 g.kg^{-1}, As to 0.300 ± 0.003 g.kg^{-1} and Cd to 0.227 ± 0.002 g.kg^{-1} in comparing with control. The ranges of soil enzymes were: dehydrogenase 0.020-157.651 TPF µg.g^{-1} in both Tobzawa and Agholane Gichka soils; urease 162-396.96 µg N-NH$_4^+$.g^{-1} in both Jideda Zab and Agholane Gawra soils; nitrate reductase 3.126-4.658 µg N-NO$_2$.g^{-1} in Agholane Gichka and Jideda Zab soils; whereas, catalase 0.5-1 ml KMnO$_4$.g^{-1}.20 min^{-1} in both Girdarasha and Tobzawa soils respectively. Significant positive correlation (r= 0.582 at p<0.05) between total bacteria and organic matter was observed. Highly positive correlation (r= 0.863 at p<0.01) between total bacteria and dehydrogenase activity was observed. A negative correlation among: the studied heavy metals with dehydrogenase and nitrate reductase; oil residues, microbial population with dehydrogenase, urease and catalase activities were other findings of the study. Higher dehydrogenase activity was observed in sandy soils than loamy soils in Agholane Gawra, Kawrgosk and Agholane Gichka soils which have higher sand contents 63.77, 69.29 and 68.25% respectively.

1. INTRODUCTION

Soil is a dynamic system in which continuous interaction takes place between soil minerals, organic matter and organisms. Each of these three major soil components influences the physicochemical and biological properties of terrestrial system (Anjaneyulu *et al.*, 2011). Soil is a favourable habitat for microorganisms; spatially fertile soil is inhabited by tremendous number of microorganisms. All kinds of organic matters deposited on soil can be decomposed by soil microorganisms, releasing different kinds of enzymes, responsible for various oxidation-reduction reactions to release the nutrients (Nath and Samanta, 2012). Enzyme activities have been used as indicators of soil quality and changes in biogeochemical function. Since enzymes catalyse all biochemical transformations, measurements of soil enzyme activities are useful indicators of biological activity as well as to understand how

human activity is changing biogeochemical cycles in ecosystems (Verchot and Borelli, 2005). Soil itself has no any enzyme activity for solubilisation as well as mobilization of minerals. But the huge number of microorganisms present in soil makes it possible to recycle the nutrients from both organic and inorganic substances (Nath and Samanta, 2012). Technologies, industrial and economic progress leads to emission of pollutants into natural environment including oil compounds and heavy metals. Soil pollution with crude oil has become an important problem of our days (Lipinska *et al*., 2013). The growing threat to the natural soil environment is growing which is caused by oil products due to leakage from tanks and pipes, truck tanks, during distribution process as well as by car and railway transport and petrol station in addition to the direct emission of these pollutants, dusts of burning gases along with oil have managed to add toxic and harmful substances to the soils (Marinescu *et al*., 2010). Toxicity of crude oil or petroleum products varies widely, depending on their composition, concentration, and environmental factors and on the biological state of the organisms at the time of the contamination (Eze *et al*., 2014). Soil pollution with heavy metals and trace elements has been reported to have toxic effects on soil biology and biochemical processes. The sources of these contaminants can come from various industrial activities among them deposition from air pollutants as a result of different fuels burning (Utobo and Tewari, 2015). Development of biological indicators to assess changes in soil quality is an increasingly important research area in the world. Assessment of soil enzymatic activities is of particular importance due to high and rapid development in the oil industry at the last century in Kurdistan Region of Iraq, and occurring of many different problems among them environmental pollution which

began to raise serious questions that need rapid solutions. Soil pollution is one of these environmental problems due to such oil industrial activities because of using huge amount of consumable fuel in the power plants and oil refinery and releasing high rate of fume, solid particulates and toxic gases more than other industries. The existence of these industries such as Kawrgosk Oil Refinery, west of Erbil city is more hazardous effects to the environment of the Erbil city, urban area and the agricultural terrains. Therefore, it has been found an importance to carry out this study to evaluate effects of oil refinery on environment of some related areas with particular reference to some soil characteristics.

2. MATERIALS AND METHODS

2.1. Study area and sample collection

Erbil Refinery is located in Khabat district, at Kawrgosk village, 40 km west of Erbil city, and it occupies a land of 2.5 Km² to the left of upper Zab River. The refinery is composed at this stage of three production lines for crude Oil refining, production, storage, distribution and supply of petroleum products as per applied standards, which represent the first plant for crude oil refining in Kurdistan region. Construction of this refinery started in 2005. The refinery produces the following oil products: naphtha, kerosene, gasoil (desel), fuel oil, gasoline and liquid gas (after operating the second production line), these products are stored and distributed in storage tanks then transported through loading stations by tankers, or may be pumped through a pipe to Erbil Depot according to the request (KAR website, 2015). For the present study, twelve sites were studied; Kawrgosk Oil Refinery and ten different sites located at different distances from the centre of the Refinery and a control soil was selected in the Greenhouse of College of Science faraway from pollution sources (Figure 1).

Figure 1: Map showing the studied area in Erbil City in Kurdistan Region of Iraq.

During October 2014, triple surface soil sample (0-15 cm depth) from each site was collected into polyethylene bags using plastic garden trowel. The samples were analysed as soon as possible. Soils were air-dried, crushed and sieved through 2-mm stainless sieve to remove debris (Pansu and Gautheyrou, 2006).

2.2. Determination of soil physicochemical properties

Hydrometer method was used for particle size distribution and determination of soil textural classes using ISSS triangle. The pH and EC of the soils were determined in 1:5 (soil: water suspension) using a calibrated pH-meter (JENWAY 3505) and an electrical conductivity meter (JENWAY 4510) according to the method given in (Ryan *et al*., 2001). Gravimetric method was used for soil moisture content determination as described by (Jaiswal, 2003). Walkly-Black procedure 1934 was followed for determination of soil organic matter as given by (Pansu and Gautheyrou, 2006).

2.3. Determination of soil oil content

Oil content in the soil samples was determined by toluene extraction method

according to (Amadi *et al*., 1996). For 10 g of soil, 200 ml of toluene was added and shake vigorously for 30 minutes by shaker; the liquid phase was extracted and measured spectrophotometrically at 420 nm. A standard curve of the absorbance of different known concentration of petroleum hydrocarbons in the extractants was derived using fresh crude oil, appropriately diluted with the solvent. Petroleum hydrocarbons concentration in soil was then calculated and expressed in $\mu g.Kg^{-1}$.

2.4. Determination of soil heavy metals

Soil heavy metal contents were determined by using X-Ray fluorescence method using a portable XRF instrument model (CIT 3000). Soil samples were dried in air, sieved through 2 mm sieve to remove non-soil particles and then XRF measured (Ulmanu *et al*., 2011). The X-ray fluorescence method is a non-destructive analytical technique, allowing both qualitative and quantitative analysis of heavy metals in soils (Derzi and Naji, 2014) based on the phenomenon of the emission of x-rays by the atoms of a sample when excited by an external source of radiation. This technique can be used for screening the metal contamination in soil with significant accuracy and reduced overall costs. Results expressed in $g.Kg^{-1}$.

2.5. Counting of soil microorganisms

Soil microbial populations including bacterial and fungal populations were counted by standard plate method using serial dilution technique. One gram of each soil sample was serially diluted $(10^{-3}-10^{-7})$ and one ml was poured into petri plates of sterile nutrient agar (pH 7.2) and incubation period of 24 hours at 30 °C for total bacterial count as given by (Harley and Prescott, 1996). For total fungal count, 0.1 ml from the diluted sample was spread with a sterile spreader on potato dextrose agar containing 0.002% Chloramphinicol for 7 days at 25 °C (Aneja, 2003). After incubation period, colonies formed on the surface of growth media were counted by colony counter. Results of soil total bacterial population expressed as $cfu.g^{-1}$ dry soil multiplied by 10^7, and soil total fungal population expressed as $cfu.g^{-1}$ dry soil multiplied by 10^3.

2.6. Estimation of soil enzyme activity

2.6.1. Estimation of dehydrogenase

The dehydrogenase activity was determined by the modified procedure of Casida 1977 given by (Anjaneyulu *et al*., 2011). For 5 g of soil in a test tube, 2.5 ml of sterile distilled water and 1ml of 3% aqueous solution of triphenyl tetrazolium chloride (TTC) was added and incubated at 30 °C for 24 hours. The triphenyl tetrazolium formazone end product was measured at 485 nm. The results expressed as μg $TPF.g^{-1}$ dry $soil.24h^{-1}$.

2.6.2. Estimation of urease

Urease activity was determined by the modified method of Hoffmann and Teicher 1961 described by (Uzun and Uyanoz, 2011). For 1 g of soil, 0.25 ml toluene, 0.75 ml citrate buffer (pH 6.7) and 1 ml of 10% urea substrate solution were added and incubated for 3 hours at 37 °C. Formation of ammonium was found out spectrophotometrically at 636 nm (Bashour and Sayegh, 2007). Results expressed as μg $N-NH_4^+.g^{-1}$ dry $soil.3h^{-1}$.

2.6.3. Estimation of nitrate reductase

Estimation of nitrate reductase was done according to (Nath and Samanta, 2012). Into 150 ml conical flasks, 50 ml of peptone water media amended with 1% KNO_3 were poured and then inoculated with 5 grams of different soil samples. The flasks were all incubated at 30 °C for 3 hours and then 10 ml of each soil suspensions were centrifuged at 5000 rpm for 10 minutes and 1 ml of the supernatants were treated with 1 ml of sulphanilamide. After 20 minutes, 1 ml of N (naphthyl) Ethelene

Diamine Dihydrochloride (NEDD) was added to each sample and left for development of a pink colour. Intensity of the pink colour was measured at 540 nm and un-inoculated media (with sulphanilamide and NEDD) used as blank. Results expressed in µg $N-NO_2.g^{-1}$ dry soil.$3h^{-1}$.

2.6.4. Estimation of catalase

The catalase activity was determined by $KMnO_4$ titration method as described by (Kumar, 2004). Two grams of oven-dried soil was mixed with 40 ml of distilled water and put on rotary shaker. Then 5 ml of 0.3% H_2O_2 was added and the slurry was shaken for 20 minutes at 150 rpm. The remaining peroxide was stabilized by adding 5 ml 3 N H_2SO_4 and 25 ml of filtered aliquots were titrated with 0.1 N $KMnO_4$. Results were expressed as ml of 0.1 N $KMnO_4.g^{-1}$ dry soil.20 min^{-1}, equivalent to the peroxide decomposed per gram of oven-dry soil.

2.7. Statistical analysis

Results were analysed using SPSS (version 18) and Microsoft excel 2010. Data is reported as mean ± standard error. One way ANOVA accompanied with Duncan's test was used for comparing the means. Person's correlation was done to test the relationship among the studied parameters from the different sites and the results considered statistically significant at ($p<0.05$) level (Le, 2003).

3. RESULTS AND DISCUSSION

3.1. Soil physicochemical properties

Soil moisture influences both the microbial and enzymatic activity (Aneja, 2003). From the studied soils, moisture content was ranged between 0.84±0.116 and 10.26±0.116 % in both Oil Refinery and control soils respectively (table 1) and same results obtained by Brzezinska et al. (1998) and Barua et al. (2011).

Soil pH considered as a chemical quality indicator of soil (Martinez et al., 2010). It influences a number of factors affecting microbial activity, like solubility and ionization of inorganic and organic soil solution constituents, and these will in turn affect soil enzyme activity (Paul, 2007). As shown in table 1, soil pH of the studied sites was ranged from 7.39±0.003 to 8.42±0.058 in Chaluke Gawra and Shewarash Zab respectively, indicating neutral to slightly alkaline soils, and this finding come in agreement with those obtained by Khudhur and Abdulla (2016). Soil electrical conductivity is used as an overall indicator of the level of macro- and micronutrients in the soil. The range of soil EC was 20±0.577 to 199±2.598 $µS.cm^{-1}$ in both Jideda Zab and Gaenj soils respectively (table 1) and Khudhur and Abdulla (2016) obtained a range of 14±1.155 to 231±1.155 $µS.cm^{-1}$ at different distances from Kawrgosk Oil Refinery which may confirm present finding.

Soil organic matter has important effects on microorganism's activities and soil enzymes has considered as an indicator of soil quality because of its character of nutrient sink and source that can enhance soil physical and chemical properties, also promote biological activity (Fontaine et al., 2003). By the present study, the highest organic matter 77.27±0.07 $g.Kg^{-1}$ was observed in Agholane Gichka soil, whereas the lowest organic matter was 15.04±0.301 $g.Kg^{-1}$ in Oil Refinery soil (table 1). Das and Varma (2011) stated that soil enzyme activities are often closely related to soil organic matter and microbial activities, relating to this, Agholane Gichka soil has the highest bacterial population 24.81×10^7 $cfu.g^{-1}$ dry soil and dehydrogenase activity 157.651 TPF $µg.g^{-1}$ dry soil.$24h^{-1}$ (table 3), and this statement may confirm our finding with regard to the close correlation of organic matter with enzymatic activities including dehydrogenase, urease and catalase (Figure 2). Soil organic

matter protects soil microorganisms against the effect of hydrocarbons which lead to lower inhibition of microbial biomass. Organic matter and clay content can absorb hydrocarbons and decrease bio-availability during their aqueous phase. Higher organic matter level can provide enough substrate to support higher microbial biomass, hence higher enzyme production (Alrumman *et al*., 2015).

Table 1: Soil physicochemical properties (mean ± S.E.) of the studied sites.

Sites	*Moisture %*	*Clay %*	*Silt %*	*Sand %*	*Texture class*	*pH*	*EC µS.cm⁻¹*	*Organic matter g.Kg⁻¹*
Shewarash Zab	3.81 ± 0.029^d	7.75	43.94	48.31	L	**8.42±0.058[a]**	54±0.577[e]	25.53±0.008[f]
Agholane Gawra	2.51 ± 0.029^{gh}	**0.00**	36.23	63.77	S L	8.04±0.006[c]	59±0.577[d]	30.70±0.001[e]
Kawrgosk	2.30 ± 0.029^h	**0.00**	30.71	**69.29**	S L	7.84±0.173[d]	76±0.577[b]	41.91±0.292[d]
Gaenj	1.32 ± 0.006^i	7.63	45.77	46.60	L	7.98±0.520[d]	**199±2.598[a]**	22.94±0.560[g]
Agholane Gichka	3.33 ± 0.038^{ef}	**0.00**	31.75	68.25	S L	7.84±0.116[d]	65±0.577[c]	**77.27±0.079[a]**
Jideda Zab	2.77 ± 0.038^{fg}	39.49	42.12	18.38	Si C L	7.74±0.116[e]	**20±0.577[h]**	47.38±0. 397[b]
Girdarasha	5.73 ± 0.038^b	42.43	39.78	**17.79**	C L	7.75±0.145[e]	28±0.289[g]	32.43±0.412[e]
Khabat	4.25 ± 0.534^e	**52.22**	**23.50**	24.28	C	7.53±0.203[f]	75±0.866[b]	31.56±0.452[e]
Chaluke Gawra	4.75 ± 0.145^c	41.56	36.36	22.08	C	**7.39±0.003[g]**	27±0.577[g]	26.39±0.401[f]
Tobzawa	2.24 ± 0.173^h	9.67	**48.34**	41.99	L	8.30±0.029[ab]	39±1.155[f]	44.50±0.144[c]
Oil Refinery	**0.84±0.116[j]**	40.34	32.78	26.89	C	8.24±0.173[b]	21±0.289[h]	**15.04±0.301[i]**
Control	**10.26±0.116[a]**	17.87	33.19	48.93	L	8.38±0.006[ab]	66±0.577[c]	16.63±0.471[h]

Different letters means significant differences between the studied sites.
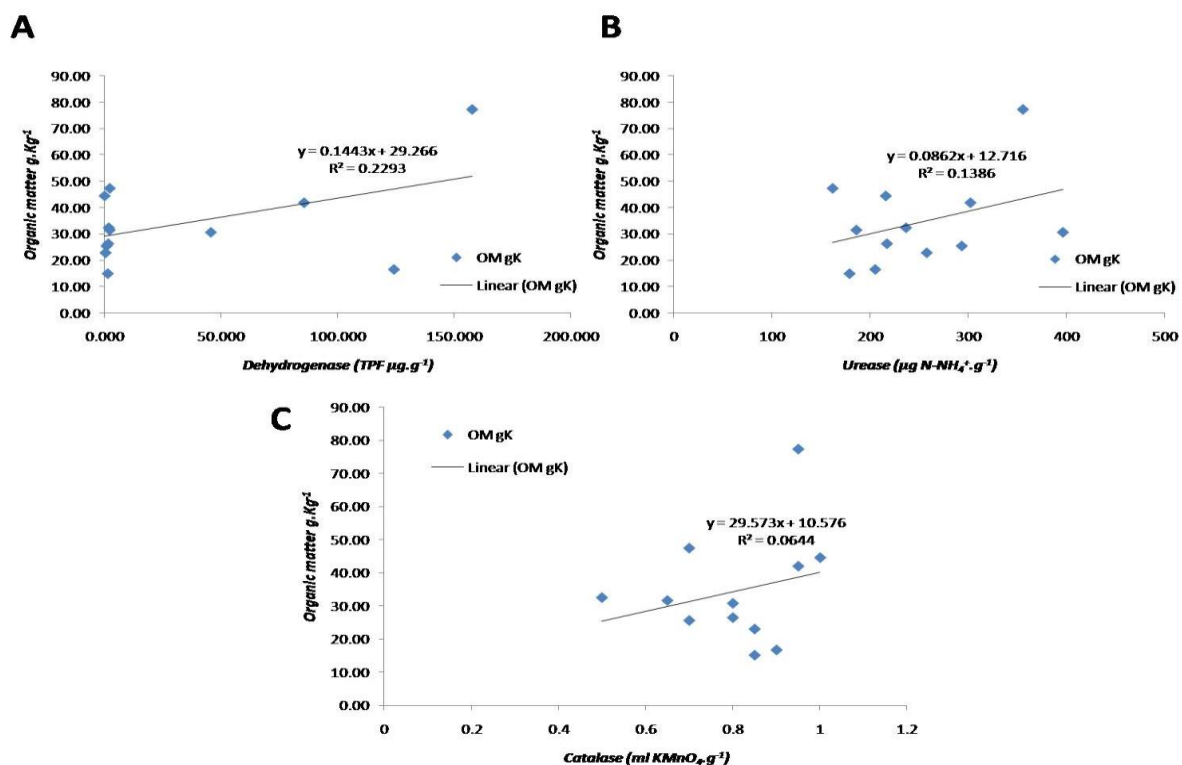
Figure 2: Correlation between: soil organic matter and enzymatic activities: (A) Dehydrogenase, (B) Urease and (C) Catalase.

3.2. Soil oil content

It is for a long time that oil materials and its derivatives cause soil pollution as a result of transportation or storage. Oil pollution results from rapid population growth and industrialization process vastly around

exploration and refining installations typically via transfer of oil materials (Khakbaz et al., 2012). Results of oil residues of the studied soils were tabulated in table 2. The highest oil content was 2.6 ± 0.000 $\mu g.Kg^{-1}$ in Oil Refinery soil and this come in agreement with a study conducted by Khudhur and Abdulla (2016)

who found the highest oil residue 0.0022 $mg.Kg^{-1}$ five kilometers away from Kawrgosk Oil Refinery and this may refer to the direct emission of some pollutants and dusts of burning gases along with oil into such area (Khakbaz et al., 2012).

Table 2: Levels of oil residues ($\mu g.kg^{-1}$) and heavy metals: Fe, Ni, As and Cd ($g.kg^{-1}$) expressed as (mean ± S.E.) in the studied sites.

Sites	Oil residues	Fe	Ni	As	Cd
Shewarash Zab	0.9±0.000	26.60±0.173[cd]*	0.108±0.001[de]	0.173±0.001[i]	0.221±0.001[bc]
Agholane Gawra	0.8±0.000	27.05±0.015[c]	0.112±0.001[cde]	0.214±0.001[e]	0.223±0.001[b]
Kawrgosk	0.8±0.000	26.35±0.245[d]	0.108±0.001[de]	0.176±0.001[h]	0.226±0.002[ab]
Gaenj	1.1±0.000	22.80±0.520[fg]	0.117±0.001[ab]	0.197±0.001[f]	0.210±0.000[d]
Agholane Gichka	1.2±0.000	23.00±0.289[f]	**0.119±0.001[a]**	0.257±0.001[c]	0.209±0.001[d]
Jideda Zab	1.2±0.000	21.60±0.173[g]	0.106±0.002[e]	**0.161±0.000[j]**	0.214±0.001[d]
Girdarasha	1.3±0.000	26.70±0.491[d]	0.109±0.000[de]	0.215±0.001[e]	0.217±0.002[c]
Khabat	0.8±0.000	23.70±0.491[f]	0.109±0.001[de]	0.218±0.001[d]	0.213±0.001[d]
Chaluke Gawra	1.1±0.000	29.00±0.289[b]	0.114±0.001[cd]	0.262±0.001[c]	0.226±0.002[ab]
Tobzawa	0.7±0.000	25.60±0.462[e]	0.118±0.003[a]	0.272±0.001[b]	0.218±0.002[c]
Oil Refinery	**2.6±0.000**	**31.50±0.433[a]**	0.116±0.002[bc]	**0.300±0.003[a]**	**0.227±0.002[a]**
Control	**0.2±0.000**	**6.25±0.072[h]**	**0.085±0.002[f]**	0.185±0.001[g]	**0.165±0.001[e]**

* Different letters means significant differences between the studied sites.

3.3. Soil heavy metals

Soil texture represents abiotic factor and one of the most important factors that influences the distribution of organic matter and ultimately play decisive role in retention of heavy metals in soil ecosystem (Sethi and Gupta, 2014). Soil texture classes were: loamy in Shewarash Zab, Gaenj, Tobzawa and Control soils; silty loam in Agholane Gawra, Kawrgosk and Agholane Gichka soils; silty clay loam in Jideda Zab; clayey loam in Girdarasha soil and clayey in Khabat, Chaluke Gawra and Oil Refinery soils (table 1).

The anthropogenic processes results to soil contamination with heavy metal are numerous among them refining process which releases numerous different metals into the atmosphere and have locally increased the levels of Cd, Co, Cr, Pb, As and Ni in soil up to dangerous levels (Ross, 1994). Consequently, there are substantial air pollution emissions, and a notable odor normally accompanies the presence of a refinery (Sharma and Agrawal, 2005). From the present study, the highest Fe

level of 31.50 ± 0.433 $g.Kg^{-1}$ was obtained in Oil Refinery, while the lowest level of 6.25 ± 0.072 $g.Kg^{-1}$ was obtained in control (table 2). Ni was ranged between 0.085 ± 0.002 and 0.119 ± 0.001 $g.Kg^{-1}$ in the soils of Control and Agholane Gichka respectively. However, As was highest in Oil Refinery soil by a value of 0.300 ± 0.003 $g.Kg^{-1}$ and lowest in Jideda Zab soil by a value of 0.161 ± 0.000 $g.Kg^{-1}$, as well as the highest Cd content 0.227 ± 0.002 $g.Kg^{-1}$ was observed in Oil Refinery while the lowest Cd content 0.165 ± 0.001 $g.Kg^{-1}$ was in control soil. The anthropogenic sources of soil contamination by arsenic and cadmium can be derived from: metalliferous mining and smelting, industry, atmospheric deposition, agriculture and waste disposal (Rasheed and Saleh, 2016).

3.4. Soil microorganisms

In soil environment, changes in microbial populations can precede detectable changes in the soil's physicochemical properties. The impact of some chemicals on soil health is dependent on microbial activities. For example,

the concentration of heavy metals in soil will not change over small time periods, but their bioavailability may. In this way, soil enzymes are acting as important indicators of soil (Das and Varma, 2011). Moreover, fungal communities in the soil are an important component because of their participation in regulating microbial activities in polluted soils (Pečiulytė and Volodkienė, 2009). Table 3 shows that the maximum total bacterial population was in Agholane Gichka by a count

of 24.81×10^7 cfu.g^{-1} dry soil and the minimum population was 0.04×10^7 cfu.g^{-1} dry soil in Oil Refinery soil and total fungal population was ranged between $2 – 39 \times 10^3$ cfu.g^{-1} dry soil in both Oil Refinery and Kawrgosk soils respectively as the same results observed by Khudhur and Abdulla (2016) and this may refer to the least amount of total organic matter in this area (table 1) which affect fungal population and diversity.

Table 3: Microbial populations and enzymatic activities in the studied sites.

Sites	Total bacteria ($\times 10^7$ cfu.g^{-1} dry soil)	Total fungi ($\times 10^3$ cfu.g^{-1} dry soil)	Dehydro-genase (TPF µg.g^{-1}.24h^{-1})	Urease (µg N-NH$_4^+$.g^{-1} .3h^{-1})	Nitrate reductase (µg N-NO$_2$.g^{-1} .3h^{-1})	Catalase (ml KMnO$_4$.g^{-1} .20min^{-1})
Shewarash Zab	1.24	13	0.823	293.76	3.660	0.70
Agholane Gawra	2.59	12	45.602	**396.96**	3.712	0.80
Kawrgosk	0.72	**39**	85.562	302.64	3.254	0.95
Gaenj	1.42	20	0.422	258.00	3.226	0.85
Agholane Gichka	**24.81**	11	**157.651**	356.16	**3.126**	0.95
Jideda Zab	2.68	5	2.229	**162.00**	**4.658**	0.70
Girdarasha	1.87	11	1.787	236.88	3.916	**0.50**
Khabat	1.82	16	2.189	186.24	3.162	0.65
Chaluke Gawra	0.58	24	1.586	217.44	3.738	0.80
Tobzawa	2.22	5	1.386	216.24	3.688	**1.00**
Oil Refinery	**0.04**	**2**	**0.020**	179.28	3.623	0.85
Control	13.96	15	124.116	205.44	3.833	0.90

3.5. Soil enzyme activity

By the present study, activity of dehydrogenase ranged from high to low levels in the research sites (table 3). Maximum dehydrogenase activity was 157.651 TPF µg.g^{-1} dry soil.24h^{-1} in Agholane Gichka and the minimum activity was 0.020 TPF µg.g^{-1} dry soil.24h^{-1} in Tobzawa soil. Since, dehydrogenase is an enzyme that is particularly sensitive to the action of toxic compounds and it can indicate type and significance of pollution in soils (Nwaogu *et al*., 2012). Therefore, in our studies, the low activity of dehydrogenases in the soils is an indicator of decreased microbiological activity in the environment.

Urease enzyme is responsible for hydrolysis of urea fertilizers applied to soil into NH_3 and CO_2 with the concomitant rise in soil pH. Soil urease originates mainly from plants and

microorganisms found as both intra- and extra-cellular enzymes (Uzun and Uyanoz, 2011). As shown in table 3, the least activity of urease was in Jideda Zab by a level of 162 µg N-NH$_4^+$.g^{-1} dry soil.3h^{-1}, while the highest activity of urease was observed in Agholane Gawra soil which was 396.96 µg N-NH$_4^+$.g^{-1} dry soil.3h^{-1} and this result come in agreement with the observation of Płóciniak (2009).

Nitrate reductase activity of soil is the product of microbial secretion to its nearest soil particles. It is useful for maintaining nitrogen ratio in atmosphere as well as removal of hazardous nitrate compounds of soil (Nath and Samanta, 2012). Lowest nitrate reductase activity 3.126 µg N-NO$_2$.g^{-1} dry soil.3h^{-1} was detected in Agholane Gichka and the greatest activity was 4.658 µg N-NO$_2$.g^{-1} dry soil.3h^{-1} in Jideda Zab soil and this may refer to the

activity of anaerobic microbial population in this area.

Catalase activities were ranged between 0.5 – 1 ml $KMnO_4.g^{-1}.20$ min^{-1} in both Girdarasha and Tobzawa soils respectively. Soil catalase activity shows a significant correlation with organic carbon content, soil microbial biomass, oxygen consumption, carbon dioxide evolution and dehydrogenase activity (Nwaogu *et al*., 2012).

The magnitude of the observed changes in the intensity of enzymatic activity together with the distance from the Oil Refinery depended on the enzyme type and properties of the studied soils. The obtained results were reflected in the values of the coefficients of linear correlation among the activity of the studied enzymes, physicochemical properties, oil residues and the content of heavy metals in the soils (table 4).

Table 4: Person's correlation among: physicochemical, microbial population and enzymatic activities in the studied soils.

	Total bacteria	*Total fungi*	*Dehydro-genase*	*Urease*	*Nitrate reductase*	*Catalase*
Moisture	0.374	0.081	0.382	-0.177	0.199	-0.193
pH	0.096	-0.358	0.132	0.116	0.048	0.362
EC	0.041	0.386	0.080	0.241	-0.558	0.214
Organic matter	0.604*	-0.036	0.483	0.372	-0.127	0.254
Fe	-0.522	-0.021	-0.536	0.159	-0.141	-0.172
Ni	-0.154	-0.130	-0.321	0.251	-0.347	0.128
As	0.086	-0.367	-0.082	-0.094	-0.270	0.298
Cd	-0.560	0.073	-0.528	0.184	-0.085	-0.152
Total bacteria	1	-0.129	0.864**	0.331	-0.227	0.364
Total fungi	-0.128	1	0.244	0.273	-0.445	0.181
Oil residues	-0.212	-0.387	-0.336	-0.223	0.044	-0.140
Dehydrogenase	0.864**	0.244	1	0.478	-0.313	0.515
Urease	0.333	0.273	0.478	1	-0.415	0.234
Nitrate reductase	-0.227	-0.445	-0.313	-0.415	1	-0.357
Catalase	0.364	0.181	0.515	0.234	-0.357	1

* Correlation is significant at the 0.05 level (2-tailed).
** Correlation is significant at the 0.01 level (2-tailed).

The observed increase in soil enzymatic activity was connected with the relatively high content of organic matter and microbial population in the soil (tables 2 and 3 and figures 2, 3 and 4). The correlation between total bacterial population and organic matter was significantly positive when r value was 0.582 at (p<0.05) and the correlation between total bacteria and dehydrogenase enzyme activity was highly positive when r value was 0.863 at (p<0.01). In this regard, Płóciniak (2009) demonstrated that the activity level of

enzymes in the soil is closely depends on the presence of carbon substrates, as well as dehydrogenase activity has been referred as indirect indicator of the number and activity of soil bacterial and fungal populations (Brzezinska, 2006). Jezierska *et al*. (2004) reported significant correlations between dehydrogenase activity, organic carbon content and crop yields in light and medium-heavy textured soils.
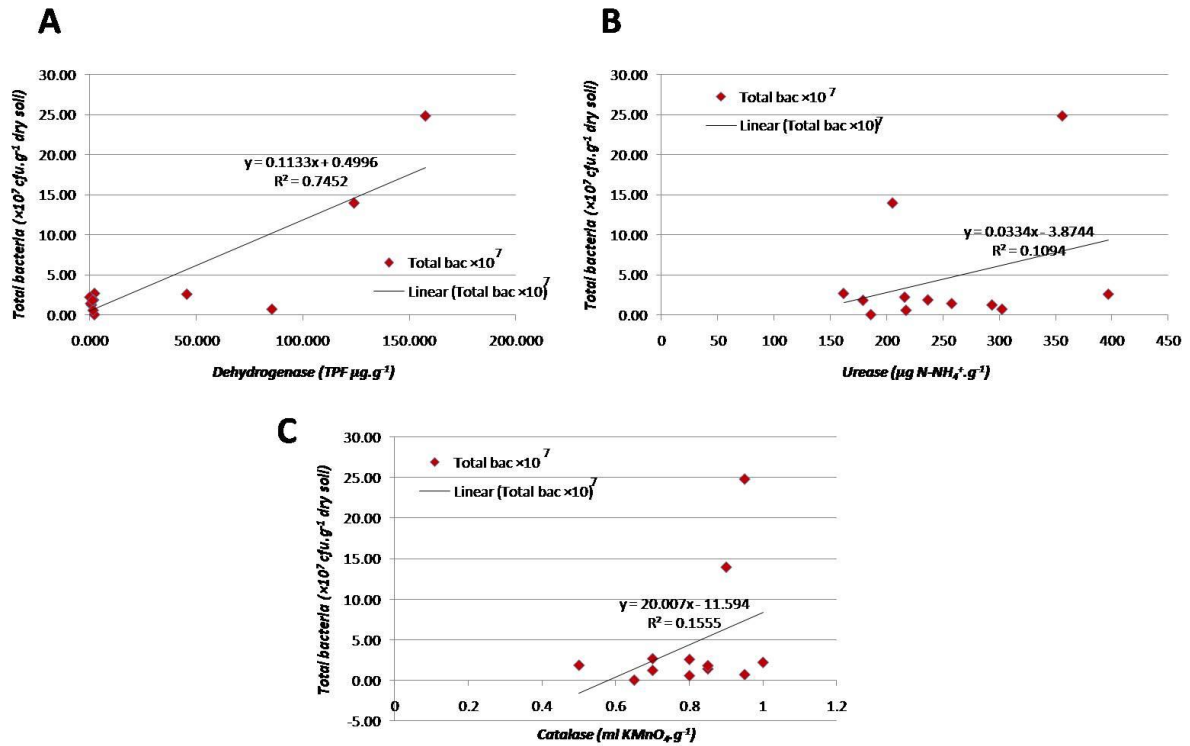
Figure 3: Correlation between: total bacterial population and enzymatic activities: (A) Dehydrogenase, (B) Urease and (C) Catalase.
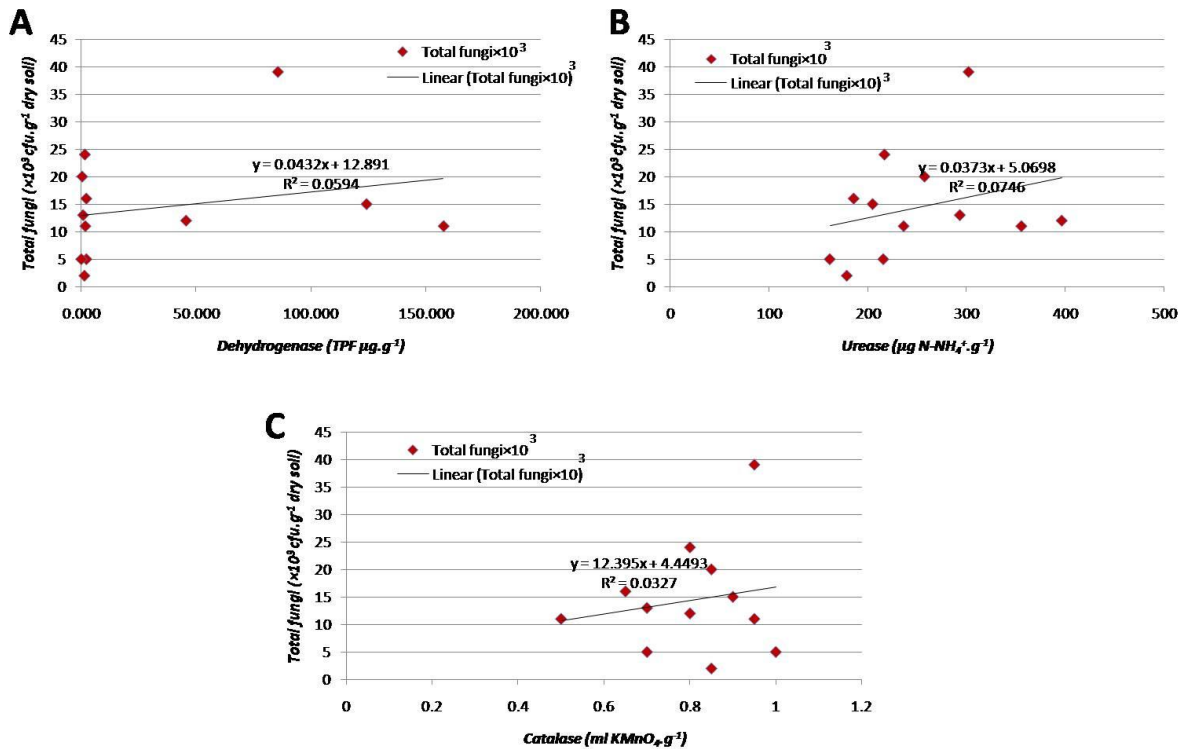
Figure 4: Correlation between: total fungal population and enzymatic activities: (A) Dehydrogenase, (B) Urease and (C) Catalase.

Moreover, we found a negative correlation among the studied heavy metals with dehydrogenase and nitrate reductase in the studied area because enzymes are characterized by high susceptibility to unfavorable environmental conditions particularly contents of heavy metals as stated by Płóciniak (2009). More findings in our study are the negative correlations among oil residues with microbial population, dehydrogenase, urease and catalase activities (Figure 5). Hawrot *et al.* (2005) recorded regardless of pollution rate, higher dehydrogenase activity in sandy soils than loamy soil and this may confirm our finding as shown in tables 1 and 3 regarding to the soils of Agholane Gawra, Kawrgosk and Agholane Gichka which has the higher sand content 63.77%, 69.29% and 68.25% respectively.
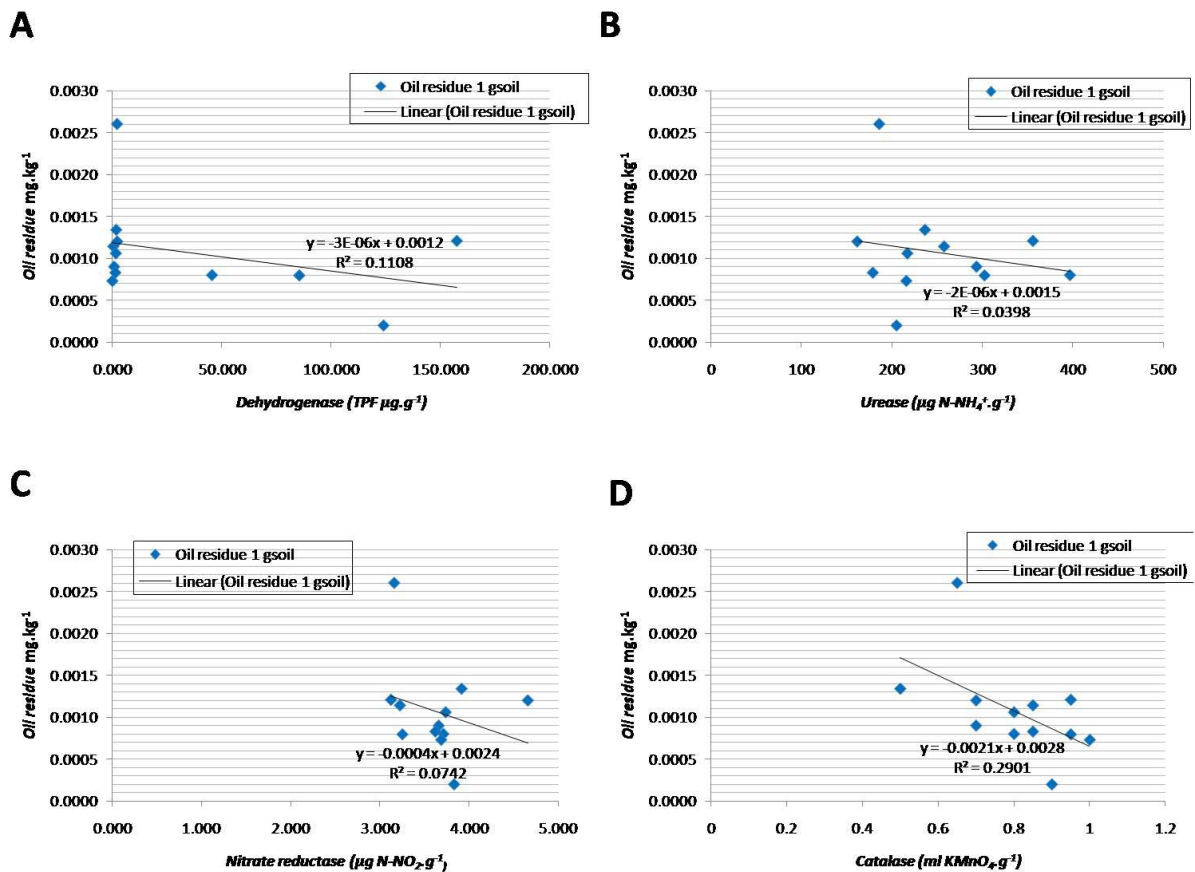
Figure 5: Correlation between: oil residue and enzymatic activities: (A) Dehydrogenase, (B) Urease, (C) Nitrate reductase and (D) Catalase.

4. CONCLUSIONS

The following were concluded by this study:

1. Soil content of oil residues and heavy metals Fe, Ni, As and Cd, as well as microbial population and the activity of the examined soil enzymes, showed considerable variability depending on the intensity of exerted anthropogenic pressure.

2. High inactivation of the examined enzymes particularly dehydrogenase in soils exposed to higher anthropogenic influence (area of Oil Refinery) indicates that the contamination of the soil environment by oil residues and heavy metals reached levels that reduce microbial population.

3. Influence of oil residue and heavy metals on microbial population and enzymatic activity is related to soil physicochemical properties.

4. A significant correlation between dehydrogenase activity and total bacteria, and the content of organic matter and total bacteria was confirmed.

5. With the increase of oil residue and heavy metals content of the soils, the enzymatic activity was decreased.

6. Dehydrogenase has proven to be the best indicator for estimating the drop of microbial activity in such soils.

7. Measuring soil enzymatic activities can provide information about the function and structure of soil microbial communities in contaminated soils.

5. RECOMMENDATION

1. Conducting further studies on determining total hydrocarbons and polycyclic aromatic hydrocarbons in different depths of soil in these areas and determining their effects on soil biochemical properties.

2. Determing these pollutants from air and effluents of Oil Refinery.

REFERENCES

ALRUMMAN SA, Standing DB and Paton GI. 2015. Effects of hydrocarbon contamination on soil microbial community and enzyme activity. *J. King Saud University – Science*, 27: 31-41.

AMADI A, Abbey SD and Nma A. 1996. Chronic effects of oil spill on soil properties and microflora of a rainforest ecosystem in Nigeria. *Water, Air and Soil Pollution*, 86: 1-11.

ANEJA KR. 2003. Experiments in Microbiology, Plant Pathology and Biotechnology. 4th edition, New Age International Publishers.

ANJANEYULU E, Ramgopal M, Narasimha G and Balaji M. 2011. Effect of pig iron slag particles on soil physico-chemical, biological and enzyme activities. *Iranica J. Energy & Environment*, 2(2): 161-165.

BARUA D, Buragohain J and Sarma SK. 2011. Certain physico-chemical changes in the soil brought about by contamination of crude oil in two oil fields of Assam, NE India. *European J. Experimental Biology*, 1(3): 154-161.

BASHOUR II and Sayegh AH. 2007. Methods of Analysis for Soils of Arid and Semi-Arid Regions. Food and Agriculture Organization of the United Nations, Rome.

BRZEZINSKA M. 2006. Biological activity and accompanying processes in organic soils irrigated with purified municipal sewage (Field and model experiments) (in Polish). *Acta Agrophysica, Rozprawyi monografie*, 2: 1-164.

BRZEZINSKA M, Stepniewska Z and Stepniewski W. 1998. Soil oxygen status and dehydrogenase activity. *Soil Biology and Biochemistry*, 30: 1783-1790.

DAS SK and Varma A. 2011. Role of Enzymes in Maintaining Soil Health. In: Soil Enzymology, edited by Shukla G and Varma A, Springer-Verlag Berlin Heidelberg, pp 25-42.

Derzi N and Naji AM. 2014. Mineralogical and heavy metal assessment of Iraqi soils from urban and rural areas. *J. Al-Nahrain University*, 17(2): 55-63.

EZE VC, Onwuakor CE and Orok FE. 2014. Microbiological and physicochemical characteristics of soil contaminated with used petroleum products in Umuahia, Abia State, Nigeria. *J. Applied & Environmental Microbiology*, 2(6): 281-286.

FONTAINE S, Marotti A and Abbadie L. 2003. The priming effect of organic matter: a question of microbial competition. *Soil Biology & Biochemistry*, 35: 837-843.

HARLEY JP and Prescott LM. 1996. Laboratory Exercises in Microbiology. 3rd edition, McGraw-Hill, U.S.A.

HAWROT M, Nowak A and Klodka D. 2005. Changes of dehydrogenases activity in soils polluted with diesel fuel. *Polish J. Microbiol*ogy, 24(1): 49-53.

JAISWAL PC. 2003. Soil, Plant and Water Analysis. Kalyani Publisher.

JEZIERSKA-Tys S, Frąc M and Fidecki M. 2004. Influence of sewage sludge fertilization on the enzymatic activity of brown soil (in Polish). *Annales UMCS, Sect. E*. 59(3): 1175-1181.

KAR website, 2015: http://www.kar-k.com/index.php/foo/oil-petrochemical/erbil-refinery

KHAKBAZ PP, Mahdeloei S and Heidari A. 2012. Soil pollution control management techniques and methods. *Annals of Biological Research*, 3 (7): 3101-3109.

KHUDHUR NS and Abdulla NQF. 2016. Soil fungal population study related to oil pollution along different distances from Kawrgosk Oil Refinery of

Erbil-Iraq, *Al-Anbar J. Agricultural Science*, 14(2), in press.

KUMAR A. 2004. Industrial pollution and management, In, Study of correlation of physical, chemical and biological characteristics with catalase activity in industrially polluted and unpolluted soils of Warangal (D.T.) A.P. by Kumari BL and Charya MA, APH Publishing. New Delhi, pp. 134-138.

LE, CT 2003. Introductory Biostatistics. John Wiley & Sons, Inc., Hoboken, New Jersey. 536 pp.

LIPINSKA A, Kucharski J and Wyszkowska J. 2013. Urease activity in soil contaminated with polycyclic aromatic hydrocarbons. *Pol. J. Environ. Stud.*, 22(5): 1393-1400.

MARINESCU M, Toti M, Dumitru M, Ignat P, Anghel A and Marinescu M. 2010. Soil pollution with crude oil - a case study in Braila County, Scientific Papers, UASVM Bucharest, Series A, Vol. LIII, 2010, ISSN 1222-5339.

MARTINEZ MM, Gutiérrez V, Jannsens M and Ortega R. 2010. Biological soil quality indicators: a review. *Current Research, Technology and Education Topics in Applied Microbiology and Microbial Biotechnology*, pp. 319-328.

NATH R and Samanta R. 2012. Soil pH, microbial population, nitrate reductase and alkaline phosphatase activities of different environment of Dibrugarh district, Assam. *Advances in Applied Science Research*, 3(3): 1772-1775.

NWAOGU LA, Agha NC and Ihejirika CE. 2012. Investigation on the long term effects of palm oil mill effluent pollution on soil catalase activity and dehydrogenase activity of soil microorganisms. *J. Bio. & Env. Sci.*, 2(4): 10-14.

PANSU M and Gautheyrou J. 2006. Handbook of Soil Analysis: Mineralogical, Organic and Inorganic Methods. Springer-Verlag Berlin Heidelberg.

PAUL EA. 2007. Soil Microbiology, Ecology, and Biochemistry. 3rd edition, Elsevier Inc., UK.

PEČIULYTĖ D and Volodkienė VD. 2009. Effect of long-term industrial pollution on microorganisms in soil of deciduous forests situated along a pollution gradient next to a fertilizer factory: 2. Abundance and diversity of soil fungi. *EKOLOGIJA*, 55(2): 133-141.

PŁÓCINIAK AM. 2009. Effect of mineral xenobiotics on the enzymatic activity of anthropogenically changed soils. *Polish J. Environ. Stud.*, 18(3): 421-427.

RASHEED, RO and Saleh, LIF 2016. Evaluation of some heavy metals from water and soil of Bazian Oil Refinery within Sulaimani Governorate IKR. *MARSH BUELLETIN*: 11(1) 2016.

ROSS SM. 1994. Toxic Metals in Soil Plant Systems. Chichester, Wiley, Press.

RYAN J, Estefan G and Rashid A. 2001. Soil and Plant Analysis Laboratory Manual. 2nd edition. International Center for Agricultural Research in the Dry Areas (ICARDA), Aleppo, Syria.

SETHI S and Gupta S. 2014. Heavy metal impact on soil microbial biomass, soil dehydrogenase activity and soil respiration rate. *Int. J. Adv. Res. Biol. Sci.*, 1(6): 29-34.

SHARMA RK and Agrawal M. 2005. Biological effects of heavy metals: an overview. *J. Environ. Biol.*, 26(2): 301-313.

ULMANU M, Anger I, Gamenţ E, Mihalache M, Plopeanu G and Ilie L. 2011. Rapid determination of some heavy metals in soil using an X-ray fluorescence portable instrument. *Research J. Agricultural Science*, 43(3): 235-241.

UTOBO EB and Tewari L. 2015. Soil enzymes as bioindicators of soil ecosystem status. *Applied Ecology and Environmental Research*, 13(1): 147-169.

UZUN N and Uyanoz R. 2011. Determination of urease catalase activities and CO_2 respiration in different soils obtained from in semi-arid region Konya, Turkey. *Trends Soil Sci. Plant Nutr. J.*, 2(1): 1-6.

VERCHOT LV and Borelli T. 2005. Application of para-nitrophenol (pNP) enzyme assays in degraded tropical soils. *Soil Biology & Biochemistry*, 37: 625-633.

Preparation and Characterization of Activated Carbon from Kurdistan Walnut Shell Activated by NaOH

Bakhtiar K. Hamad[1,2]

[1]Department of Environmental Engineering, College of Engineering, Knowledge University, Erbil, Kurdistan Region, Iraq.

[2]Department of General Science, College of Basic Education, Salahaddin University, Erbil, Kurdistan Region, Iraq.

A R T I C L E   I N F O

A B S T R A C T

Kurdistan walnut shell (KWS) was examined for preparation of activated carbon using sodium hydroxide as chemical agent. The characterisations of the Kurdistan walnut shell activated carbon by sodium hydroxide (WSAC-NaOH) were studied using different techniques. pH of point of zero charge (pH_{pzc}), iodine number and proximate analysis. The adsorption of methylene blue by prepared activated carbon was analyzed by the Langmuir and Freundlich adsorption isotherms. The data fitted well to the Freundlich isotherm with the maximum adsorption capacity = 344.8 mg/g for Langmuir adsorption isotherm. The analysis showed that the activated carbon derived from walnut shell activated by sodium hydroxide is more capable than commercial activated carbon (CAC) and can be used as a possible adsorbent.

1. INTRODUCTION

Activated carbon is a porous carbonaceous material, whether in a powder or granular form. It is a structure consisting of a network of interconnected micropores, mesopores and macropores that demonstrates a good ability for the adsorption of organic molecules because of its high surface area (Arvind and Hara, 2016).

However, its applications are limited due to high cost. To provide economic solution, the use of low cost of agricultural by-products has been shown to produce activated carbon. Different agricultural by-products such as bean pod (Cabal et al., 2009), almond shell (Demirbas et al., 2008), cherry stone (Jaramillo et al., 2009), rice husk (Sahu et al., 2009), date palm seed (El Nemr et al., 2008), bamboo (Hameed and El-Khaiary, 2008), sunflower seed hull (Thinakaran et al., 2008), coconut husk (Tan et al., 2008a), and waste apricot (Onal et al., 2007) have been used for preparation of activated carbons. In addition, few studies have been reported in the literature on the use of walnut shell using as agricultural waste-based activated carbon.

Walnut shell is one of the common agricultural by-products with large quantity in Kurdistan. Annually several tons of walnut shells are produced in Kurdistan. Including compounds of walnut shell are lignin, hemicellulose, and cellulose with low ash and a high carbon content which renders it a

appropriate precursor for activated carbon production. Walnut shell because of its availability as a renewable resource and high rigidity has been effectively used for activated carbon production and its use in removing pollutants by adsorption has been studied (Srinivasan and Viraraghavan, 2008; Ayrilmis et al., 2013).

In the impregnation process, the precursor is mixed with an amount of chemical agents such as KOH (Ji et al., 2007; Feng-Chin et al., 2005), NaOH (Cazetta et al., 2011), H_3PO_4 (Yorgun and Yıldız, 2015) and $ZnCl_2$ (Pezoti et al., 2014) which cause the development of porous structures in the raw material. In this study, activated carbon has been produced by using a physiochemical activation method from Kurdistan walnut shell using sodium hydroxide as chemical agent.

2. MATERIALS AND METHODS

2.1. Preparation of the Activated Carbon

The precursor for the preparation of activated carbon was walnut shells were collected from local markets in Erbil, Iraq. To remove impurities, the raw material was washed with hot distilled water and dried. The raw material was cut into small pieces and then sieved to an average particle size of 2.5 – 2.0 mm. Sixty grams of raw material was impregnated in 10 % chemical agent (NaOH) at 1: 2 ratio (w/v) and heated in a water bath at 85-90 °C for 24 h. The raw material was separated from the solution, washed with distilled water until the solution became neutral, and then dried in an oven overnight at 100 °C. The sample was then placed in a stainless steel vertical tubular reactor and put in the furnace. The process of carbonization was conducted under high purity nitrogen gas (99 %) at a flow rate of 150 cm3/ min with a

heating rate to 400 °C under the pressure of 1 atm and held for 2 h. The product was cooled to room temperature (25 °C), washed with distilled water, and then dried in an oven at 100 °C.

2.2. Characterization of Adsorbent

2.2.1. Iodine value test

The adsorption of aqueous iodine is measured a simple test for estimating the surface area of activated carbons. However, the relationship between surface area and iodine number cannot be generalized. It varies with changes in raw material of carbon and pore volume distribution. 0.1 g of dry commercial activated carbon and prepared activated carbon was separately taken in dried 100 ml conical flasks. The samples were run in duplicates and added 5 ml of 5% HCl .The flasks were shaken until the carbon was dumped.10ml of 0.1N iodine solution was added to each flask and was shaken properly for 4 minutes. 10 ml filtrate was titrated against standard (0.1N) sodium thiosulphate solution using starch as an indicator. The concentration of iodine adsorbed by activated carbon was calculated as amount of iodine adsorbed in milligrams. The used solution in this test was performed according to American Society for Testing and Materials Standard (ASTM, 2006).

2.2.2. Methylene test

Methylene blue adsorption tests were conducted by mixing 0.1 g of each, WSAC and CAC separately with 100 ml of 25, 50, 75 and 100 mg L^{-1} of methylene blue solution. After shaking for 24 hours, the solutions were filtered and methylene blue residual concentration was measured at 660 nm using UV /Vis spectrophotometer for the determination of concentration. The amount of adsorption at equilibrium, q_e (mg/g) was

calculated through the follow equation (Alam et al., 2007) :

$$q_e = \frac{(C_0 - C_e)V}{W} \tag{1}$$

where C_0 and C_e (mg/g) are the initial and equilibrium concentrations of methylene, respectively, V (L) is the volume of the solution, and W (g) is the mass of dry adsorbent used. The percentage removal of methylene was calculated using the following equation (Azam et al., 2009) :

$$\text{Removal (\%)} = \frac{(C_0 - C_e)}{C_0} \times 100 \tag{2}$$

2.2.3. Determination of moisture content

1.0 g of each of WSAC and CAC were taken in dried and weighed crucibles separately. The crucibles were kept in an oven held at a temperature of 105 ºC for 4 hours. The crucibles were put in a desiccator for 1 hour and weighed. For determination of moisture content ASTM–D1762 (1990) was used. The percentage of moisture content was measured as follows:

$$\text{Moisture (\%)} = \left[\frac{(A - B)}{A}\right] * 100 \tag{3}$$

Where A = weight of dried sample, B = weight of the sample after drying at 105 ºC

2.2.4. Determination of ash content

1.0 g of each of WSAC and CAC were taken in dried and weighed crucibles separately. The samples were run and put in a muffle furnace at 750 ºC for 6 h. The crucibles were cooled in a desiccator and weighed. The percentage of ash content was calculated as follows:

$$Ash (\%) = \frac{D}{B} * 100 \tag{4}$$

Where D = weight of residue left in gram, B = weight of dried sample in gram.

2.2.5. Determination of pH

For determine pH of WSAC and CAC, the standard test method ASTM-D3838 was utilized (ASTM, 1996). 1.0 g of WSAC and CAC were transferred into 100 ml distilled water taken in a beaker and stirred by a magnetic bar for 1 h separately. pH meter was used for measuring pH.

2.2.6. Determination of pH of point of zero charge (pH_{pzc})

pH_{pzc} of activated carbon is significant because it shows the net surface charge of the carbon in the liquid phase. The pH_{pzc} is the point where the curve of pH_{final} vs $pH_{initial}$ intersects the line $pH_{initial} = pH_{final}$. In order to determine the pH of point of zero charge 0.15 g of WSAC and CAC was taken to eleven 100 ml conical flasks containing 50 ml of 0.01M NaCl separately, whose initial pH has been measured and adjusted with NaOH or HCl for each activated carbon. The conical flasks were sealed and placed in a shaker for 24 hours after which the pH was measured.

3. RESULTS AND DISCUSSION

3.1. Investigation of sorption parameters

3.1.1 Effect of NaOH

The addition of NaOH solution to the carbon structure creates the feasibility of reactions with all four elements concerned, namely the carbon, the hydrogen, the oxygen and the sodium. The products of these reactions include sodium metal, water, carbon dioxide

and sodium carbonate. Possible general reactions, for NaOH are as follows:

$$4NaOH + C \leftrightarrow 4Na + CO_2 + 2H_2O \quad (1)$$

$$4NaOH + 2CO_2 \leftrightarrow 2Na_2CO_3 + 2H_2O \quad (2)$$
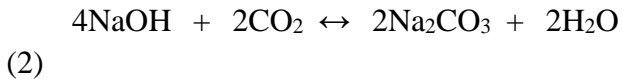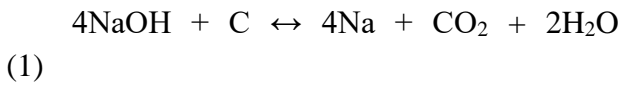
The mechanism of surface reactions will be much less complicated than indicated by these general reactions which can never take place as written. Rather, the processes will take place through a series of much simpler, simultaneous/consecutive reactions. The first state of dispersion of the NaOH is significant to maximize the contact between the carbon surface and NaOH (Marsh and Rodriguez-Reinoso, 2006).

3.1.2. Surface characterization of activated carbon

The low moisture and ash content showed in Table 1 revealed that the raw material is capable for the preparation of activated carbons. A small increase in ash content causes a reduce in adsorptive properties of adsorbent. Thus, the activated carbon content of low ash better for use in adsorption process (Quershi et al., 2007). The activated carbon prepared from the raw materials of walnut shell can be used as a good adsorbent instead of commercial activated carbon. The pH of WSAC and CAC was found to be 6.9 and 6.5 respectively. Activated carbon pH between 6 and 8 is suitable for most application (Ahmedna et al., 2000). pH is affected by the reaction of carbon dioxide and organic-inorganic solutes present in water. Any change in water pH is accomplished by the modification in other physicochemical parameters (Parihar et al., 2012). If the solution pH of activated carbon has greater than pH_{pzc}, the surface of the carbon will be negatively

charged and cations may be adsorbed on the surface. On the other hand, at solution pH less than their pH_{pzc} activated carbon surface is that it will have a positive charge and hence be a surface on which anion may be adsorbed. The pH_{pzc} of WSAC and CAC were found to be 6.5 and 6.2 respectively.

Iodine adsorption from liquid phase was assumed to gain further information of the porous structure and characterization of activated carbon. The adsorption of iodine is measured a simple test for assessing the surface area of activated carbons associated with pores larger than 1 nm (Benadjemia et al., 2011). Iodine number is a suggestion of the adsorption capacity in microspores; so it is often employed to study the adsorption capacity of the activated carbons by researchers. Table 1 shows the iodine number of WSAC (976 mg/g) and CAC (805 mg/g). A higher value of iodine number for WSAC in comparison to CAC is due to greater surface area and available pore sites for adsorption of iodine molecule on the surface. Adsorption is a natural process by which molecules of a dissolved compound collect and adsorb to the adsorbent solid surface (Bhise et al., 2012). The activated carbon prepared from walnut shell, it is cheap and available material can be used as activated carbon.

Scanning electron microscopy at Kurdistan Institution for Strategic Studies and Scientific Research (KISSR) was used to characterise the morphology of the adsorbent surface. Figs. 1(a) and 1(b) demonstrations the surfaces of the walnut raw material and walnut activated carbon, respectively, prepared by impregnation with NaOH solution for 24 h and a pyrolysis temperature of 400 °C. Many developed pores can be seen in Fig. 1(b) compared with Fig. 1(a), which shows a smooth surface and these pores are not present

in the walnut raw material. The development of pores is due to the effect of the NaOH concentration. The expansion of pore sizes during carbonization is essential for increasing the surface area of the activated carbon. (Tan et al., 2008b).
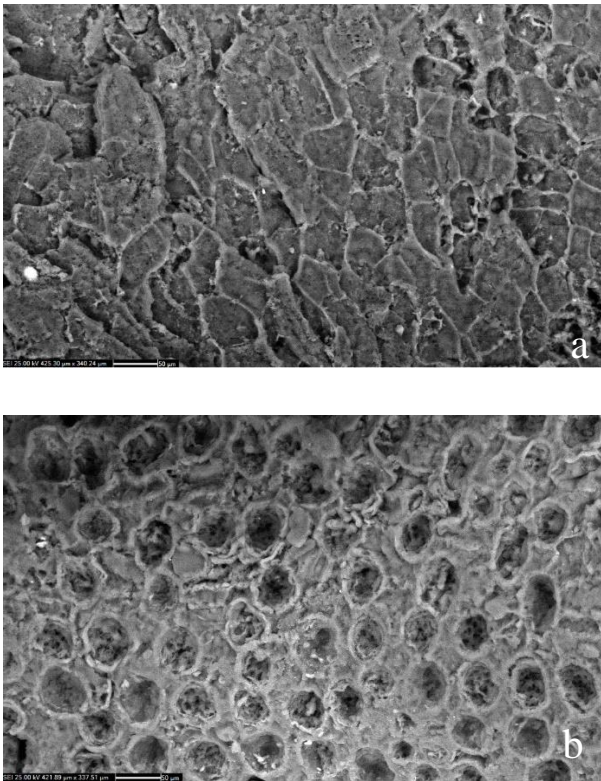
Figure1. SEM micrographs of the Kurdistan walnut shell (a) before and (b) after   carbonization at 400 ◦C

3.2. Adsorption isotherms

In order to optimize the design of an adsorption model, it is significant to set up the most appropriate correlation for the equilibrium curves. In this study, two adsorption isotherms which are the Langmuir and Freundlich isotherms were used to describe the relationship between the amount of methylene adsorbed onto WSAC and CAC and its equilibrium concentration in the solutions.

3.2.1. Langmuir isotherm model

According to Langmuir isotherm, the adsorption occurs at homogenous sites and the nature of the adsorption is monolayer and once the adsorbate is attached on the site, no further adsorption can take place on that site (Hall et al., 1996). The linear equation of Langmuir isotherm is given in Eq. 5.

$$\frac{C_e}{q_e} = \frac{1}{q_{max}b} + \frac{C_e}{q_{max}}$$

(5)

where q_e and C_e are the equilibrium concentration of methylene in the adsorbed and liquid phases in mg/g and mg/L, respectively; q_{max} (mg/g) and b (L/mg) are Langmuir constants, which are associated with the maximum adsorption capacity and energy of adsorption, respectively,   which can be calculated from the slope of the linear plot of C_e / q_e vs. C_e as shown in Figs. 2 and 3.
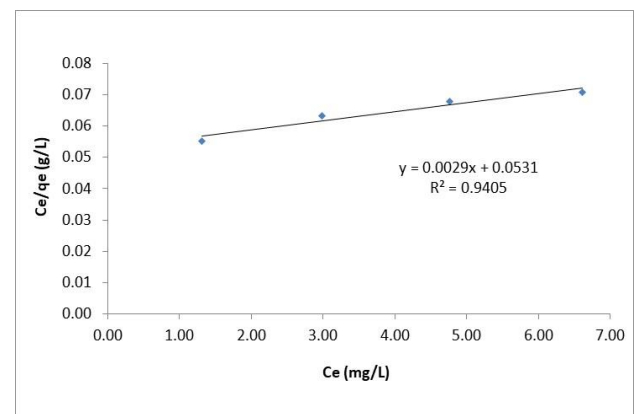
Figure 2. Langmuir isotherm for methylene adsorption onto WSAC
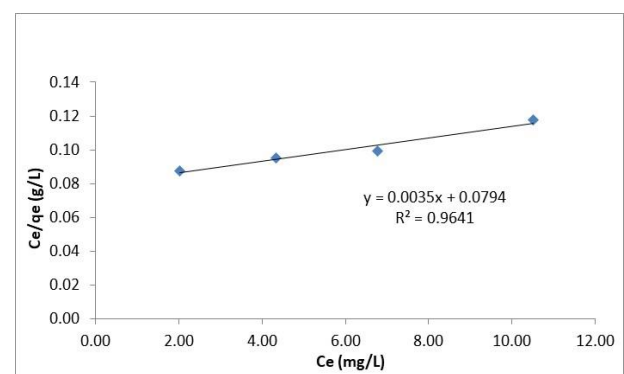
Figure 3. Langmuir isotherm for methylene adsorption onto CAC

3.2.2. Freundlich isotherm model

The Freundlich isotherm model describes the heterogeneous multilayer surfaces of adsorption due to the different trends supporting the surface sites. It supports that occupation will occur at the first stage through stronger binding, and will later decrease with the increasing degree of sites occupation (Tan et al., 2008b). The well-known logarithmic form of Freundlich isotherm is given in Eq. 6.

$$\ln q_e = \ln k_f + \frac{1}{n} \ln C_e \qquad (6)$$

where C_e and q_e are the equilibrium concentrations of methylene in the liquid and adsorbed phases, in mg/L and mg/g, respectively. The Kf (mg/g) $(L/mg)^{1/n}$ and n (L/mg) are the Freundlich constants associated with the adsorption intensity and capacity, respectively, which can be measured from the intercept and slope of the linear plot of ln qe vs. ln Ce as shown in Figs. 4 and 5.

Table 2 show Langmuir and Freundlich constants for methylene blue adsorption onto WSAC and CAC. The values of coefficient of determination (R^2) were 0.999 and 0.994 for WSAC and CAC respectively, which is indicated that the Freundlich adsorption isotherm model was representing the adsorption for removing of adsorbate. On the other hand, the maximum adsorption capacity for WSAC was calculated for Langmuir isotherm equal to (344.8 mg/g) was higher than other adsorbents as a comparison of methylene blue adsorption onto different adsorbents as shown in Table 3.
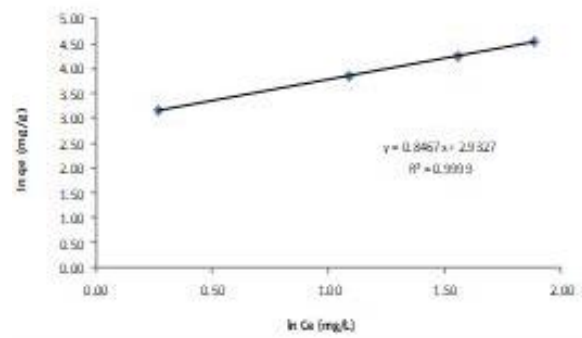
Figure 4. Freundlich isotherm for methylene adsorption onto WSAC
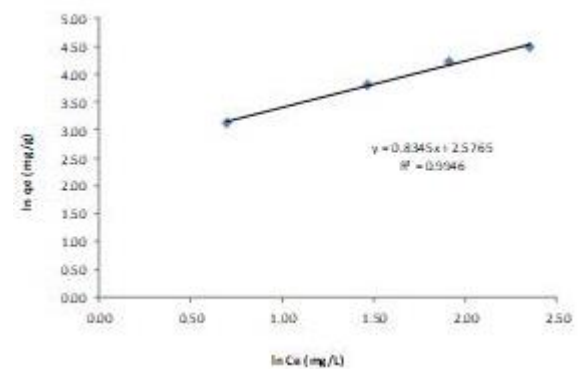
Figure 5. Freundlich isotherm for methylene adsorption onto CAC

Table 1: Physicochemical properties of WSAC and CAC

Property	WSAC	CAC
pH (mole/L)	6.9	6.5
pH$_{pzc}$ (mole/L)	6.5	6.2
Moisture (%) (g/m^3)	0.21	0.28
Ash (%) (g/m^3)	2.37	2.49
Iodine number (mg/g)	976	805
Adsorption capacity of Methylene blue (mg/g)	344.8	285.7

Table2: Langmuir and Freundlich constants for methylene blue adsorption onto WSAC and CAC

Adsorbents	Langmuir			Freundlich		
	b	q_m	R^2	Log K	1/n	R^2
CAC	0.07	285.7	0.964	2.57	0.82	0.994
WSAC	0.05	344.8	0.940	2.93	0.84	0.999

Table 3: Comparison of adsorption capacities of methylene blue on the studied adsorbent with that reported in the literature

Precursor	Adsorption capacity (mg/g)	References
Sunflower oil cake	16.43	Karagöz et al., 2008
Cashew nut shell	68.72	Kumar et al., 2011
Pine wood powder	200.00	Wang et al., 2009
Lapsi seed stone	277.00	Shrestha et al., 2012
Bamboo	286.10	Liu et al., 2010
Cotton stalk	315.45	Deng et al., 2009
Walnut shell	344.80	Present study

4. CONCLUSIONS

Depend on the experimental results and the related discussions, the walnut shell agricultural by-product was showed to be good raw material for preparation of activated carbons using physicochemical activation methods consisting of NaOH impregnation plus N2 gasification. The Freundlich adsorption isotherm was the best model for representing the adsorption for removing of adsorbate.

In conclusion, the present investigations showed that walnut shell activated carbon could be used successfully in the removal of pollutants from aqueous solutions at the adsorption equilibrium.

REFERENCES

Ahmedna M., Marshall W.E. and Rao R.M., (2000). Granular activated carbons from agricultural by-products: preparation, properties and application in sugar refining, Bulletin of Lousiana state, University Agricultural Centre, 54.

Alam, Md. Zahangir, Muyibi, Suleyman A. Mansor, Mariatul F. and Radziah, W. (2007).

Activated carbon derived from oil palm empty-fruit bunches: Application to environmental problems, J. of Environ. Sci., 19, 103-108.

American Society for Testing and Materials Annual Book of ASTM Standard, 15.01, Refractories, Carbon and Graphic Products; activated carbon, ASTM, Philadelphia PA (1996)

American Society for Testing and Materials Standard test method of determination of iodine number of activated carbon, ASTM Committee on Standards (2006)

American Society for Testing and Materials Standard test methods for moisture in activated carbon, Philadelphia, PA: ASTM Committee on Standards (1991)

Arvind, K. and Hara, M. (2016). Preparation and characterization of high surface area activated carbon from Fox nut (Euryale ferox) shell by chemical activation with H_3PO_4, Results in Physics, 6, 651–658.

Ayrilmis, N. Kaymakci, A. and Ozdemir, F. (2013). Physical, mechanical, and thermal properties of polypropylene composites filled with walnut shell flour, J. Ind. Eng. Chem., 19 (3), 908.

Azam T. Mohd Din, Hameed, B.H. and Ahmad, Abdul L. (2009). Batch adsorption of phenol onto physiochemical-activated coconut shell, J. Hazar. Mater., 161, 1522-1529.

Benadjemia M., Milliere Reinert L., Benderdouche N. and Duclaux L., (2011). Preparation, Characterization and Methylene blue adsorption of phosphoric acid activated carbons from globe artichoke leaves, Fuel Process Technol, 92, 1203-1212.

Bhise R.M., Patil A.A., Raskar A.R., Patil P.J. and Deshpande D.P, (2012). Removal of Colour of Spent Wash by Activated Charcoal Adsorption and Electrocoagulation, Res. J. Recent. Sci., 1(6), 66-69.

Cabal, B., Budinova, T., Ania, C. O., Tsyntsarski, B., Parra, J. B. and Petrova, B. (2009). Adsorption of naphthalene fromaqueous solution on activated carbons obtained from bean pods. *J. Hazard. Mater.,* 161**,** 1150-1156.

Cazetta AL, Vargas AMMM, Nogami EM, Kunita MH, Guilherme MR, Martins AC. (2011). NaOH-activated carbon of high surface area produced from coconut shell: kinetics and equilibrium studies from the methylene blue adsorption. Chem Eng J., 174, 117–25.

Demirbas, E., Kobya, M. and Konukman, A. E. S. (2008). Error analysis of equilibrium studies for the almond shell activated carbon adsorption of Cr(VI) from aqueous solutions. *J. Hazard. Mater.,* 154**,** 787-794.

Deng, H., Yang, L., Tao, G., and Dai, J. (2009). Preparation and characterization of activated carbon from cotton stalk by microwave assisted chemical activation-application in methylene blue adsorption from aqueous solution, J. Hazard. Mater. 166(2), 1514-1521.

El Nemr, A., Khaled, A., Abdelwahab, O. and El-Sikaily, A. (2008). Treatment of wastewater containing toxic chromium using new activated carbon developed from date palm seed. *J. Hazard. Mater. ,* 152**,** 263-275.

Feng-Chin W, Ru-Ling T, Ruey-Shin J. (2005). Preparation of highly microporous carbons from fir wood by KOH activation for adsorption of dyes and phenol from water. Sep Purif Technol., 47, 10–9.

Foo K.Y. and Hameed B.H., Preparation, (2012). Characterization and evaluation of adsorptive properties of orange peel based activated carbon via microwave induce K_2CO_3 activation, Bioresour Technol, 104, 679-689.

Hall, K. R., Eagleton, L. C., Acrivos, A. and Vermeulen, T. (1996). Pore-and solid-diffusion kinetics in fixed-bed adsorption under constant-pattern conditions. *Ind. Eng. Chem. Fundam.,* 5**,** 212-223.

Hameed, B. H. and El-Khaiary, M. I. (2008). Sorption kinetics and isotherm studies of a cationic dye using agricultural waste: broad bean peels. *J. Hazard. Mater. ,* 154**,** 639-648.

Jaramillo, J., Gomez-Serrano, V. and Alvarez, P. M. (2009). Enhanced adsorption of metal ions onto functionalized granular activated carbons prepared from cherry stones. *J. Hazard. Mater.,* 161**,** 670-676.

Ji Y, Li T, Zhu L, Wang W, Lin Q. (2007). Preparation of activated carbon by microwave heating KOH activation. Appl Surf Sci., 254, 506–12.

Karagöz, S., Tay, T., Ucar, S., and Erdem, M. (2008). Activated carbons from waste biomass by sulfuric acid activation and their use on methylene blue adsorption, Bioresour. Technol. 99(14), 6214.

Kumar, P. S., Ramalingam, S., and Sathishkumar, K. (2011). Removal of methylene blue dye from aqueous solution by activated carbon prepared from cashew nut shell as a new low-cost adsorbent, Korean J. Chem. Eng. 28(1), 149-155.

Liu, Q. S., Zheng, T., Wang, P., Jiang, J. P., and Li, N. (2010). Adsorption isotherm, kinetic and mechanism studies of some substituted phenols on activated carbon fibers, Chem. Eng. J. 157(2), 348-356.

Marsh, H. and Rodriguez-reinoso, F. (2006). *Activated Carbon*, Elsevier Science and Technology Books.

Onal, Y., Akmil-Basar, C. and Sarici-Ozdemir, C. (2007). Elucidation of the naproxen sodium adsorption onto activated carbon prepared from waste apricot: kinetic, equilibrium and thermodynamic characterization. *J. Hazard. Mater.,* 148**,** 727-734.

Parihar S.S. Kumar Ajit, Kumar Ajay, Gupta R.N. Pathak Manoj, Shrivastav Archana and Pandey A.C. (2012). Physico-Chemical and Microbiological Analysis of Underground Water in and Around Gwalior City ,MP , India, Res. J. Recent Sci., 1(6), 62-65.

Pezoti Jr O, Cazetta AL, Souza IPAF, Bedin KC, Martins AC, Silva TL, Almeida VC. (2014). Adsorption studies of methylene blue onto ZnCl2-activated carbon produced from buriti shells (Mauritia flexuosa L.). J Ind Eng Chem., 20, 4401–7.

Quershi K., Bhatti I., Kazi R., Ansari A.K., (2007). Physical and Chemical Analysis of Activated carbon from Sugarcane Bagasse and use for Sugar Decolorization, World Academy of Science, Engineering and Technology, 34.

Sahu, J. N., Agarwal, S., Meikap, B. C. and Biswas, M. N. (2009). Performance of a modified multi-stage bubble column reactor for lead(II) and biological oxygen demand removal fromwastewater using activated rice husk. *J. Hazard. Mater.,* 161**,** 317-324.

Shrestha, R. M., Yadav, A. P., Pokharel, B. P., and Pradhananga, R. R. (2012). Preparation and Characterization of Activated Carbon from Lapsi (Choerospondias axillaris) Seed Stone by Chemical Activation with Phosphoric acid. *Research Journal of Chemical Sciences*. 2(10), 80-86.

Srinivasan, A. and Viraraghavan, T., (2008). Removal of oil by walnut shell media, Bioresource Technol., 99 (17), 8217.

Tan, I. A. W., Ahmad, A. L. and Hameed, B. H. (2008a). Adsorption of basic dye on high-surfacearea activated carbon prepared from coconut husk: equilibrium, kinetic and thermodynamic studies. *J. Hazard. Mater. ,* 154**,** 337-346.

Tan, I. A. W., Ahmad, A. L., Hameed, B. H. (2008b). Adsorption of basic dye using activated carbon prepared from oil palm shell: batch and fixed bed studies. *Desalination*, 225, 13-28 .

Thinakaran, N., Baskaralingam, P., Pulikesi, M., Panneerselvam, P. and Sivanesan, S. (2008). Removal of acid violet 17 from aqueous solutions by adsorption onto activated carbon prepared from sunflower seed hull. *J. Hazard. Mater.,* 151**,** 316-322.

Wang, T., Tan, S., and Liang, C. (2009). Preparation and characterization of activated carbon from wood via microwave-induced $ZnCl_2$ activation, *Carbon*, 47(7), 1880-1883.

Yorgun S, and Yıldız D. (2015). Preparation and characterization of activated carbons from Paulownia wood by chemical activation with H_3PO_4. J Taiwan Inst Chem E., 53, 122–31.

Isotherm Studies of Adsorption of Cadmium (II) ion from Aqueous Solution onto Zeolite: Effects of Time, Temperature and pH

Ahmed A. Amin[1], Heman A. Smail[2], Hawraz Ibrahim M. Amin[2]

1- Department of Chemistry, College of Education, Salahaddin University, Erbil, Kurdistan Region, Iraq.

2- Department of Chemistry, College of Science, Salahaddin University, Erbil, Kurdistan Region, Iraq.

ARTICLE INFO

*Corresponding Author:

Ahmed A. Amin

Ahmed.dezaye@su.edu.krd

ABSTRACT

Today, synthetic zeolites are used commercially additional frequently than natural zeolites due to the purity of crystalline products and the regularity of particle sizes. A synthesized $Na_3K_6(H_2O)_{21}[Si_{27}Al_9O_{72}]$ (Lind type L) LTL zeolite was characterized using X-Ray diffraction (XRD), Field Emission Scanning Electron Microscopy (FE-SEM) and Transmission Electron Microscopy (TEM). The work reports the utilization of synthesized zeolite as an adsorbent for the removal of cadmium (II) ion from aqueous solution. The effects of sorption time, temperature, heavy metal concentration and pH, on the adsorption process were investigated using a batch method. Langmuir, Freundlich, and Temkin isotherms over the entire concentration range from 20-50 mg.L^{-1} were used to narrate the adsorption isotherms and their constants evaluated. The equilibrium data were found to be fitted the Langmuir and Freundlich models. Our study shows that the maximum adsorption of Cd is at pH 8.0 and 313K.

1. INTRODUCTION

Nowadays, removing the toxic heavy metal contaminants from aqueous waste streams is one of the greatest matters of interest in the literature and studies. The main concern of environmentalists about heavy metals is that these elements are highly toxic and their detrimental impact on human health and surroundings is grave (Aklil, *et al.,* 2004). Cadmium is one of the most toxic metals levels in a low concentration. It is naturally formed in the environment and is a vital polluting.

Cadmium (Cd) toxicity sources confusions like heart disease, cancer and diabetes. Cadmium poisoning may also consequence in lung cancer, anemia, skin, pulmonary edema, bone diseases, brain damage and trachea-bronchitis (Voegelin, and Kretzschmar, 2003). Cadmium gathers in bone, liver and kidney and is even more poisonous than mercury. Taking in any considerable amount of Cd leads to instantaneous intoxication and damage to the liver and the kidney (Deng and Ting, 2005). Cadmium is mainly produced when waste

streams are released from metallurgical alloying, ceramics, metal plating and sewage sludge. Conventional methods including, reverse osmosis electrodialysis (Mohammadi, *et al.,* 2005), ion-exchange, chemical precipitation, ultrafiltration (Ennigrou, *et al.,* 2009) generally, the adsorption methods are favorable methods for removing heavy metals from aqueous solutions because it is economically advantageous, highly efficient and easily applicable (Hamedreza, *et al.,* 2015). Some materials can be used as adsorbents, like activated carbon, aluminosilicate (clay materials), natural and synthetic zeolites (Dawodu, *et al.,* 2012). Zeolites are hydrated aluminosilicate produced under the hydrothermal states. It can be discovered naturally, or can be synthesized. Synthetic zeolites were first deploying commercially as molecular sieve adsorbent. They are ideally synthesized from a solution of sodium silicate and sodium aluminates. Zeolites can then be synthesized from a variety of raw materials; natural and synthetic glasses, aluminosilicate gels, and clay materials, example kaolin (Vimala and Das, 2009). It has been discovered that the starting material and shapes for the preparation have an influence on the resulting kinds and amount of zeolites to be obtained (Prasad, *et al.,* 2009). Based on an obtainable materials and publications, it could be concluded that due to their unique properties, zeolites have a considerable potentials as effective sorbent material for large number of water treatment applications like water softening ammonia removal (from municipal sewage, animal farms, fertilizer mill waste water, fish breeding pond, swimming pools), move of heavy metals (from natural water acid mines drainages, industrial wastewater), phosphates ejection of dissolved organic compounds and dyes, oil spillage surgery and many others. Ions of heavy metals such as copper, nickel, zinc, cadmium, lead, chromium

and mercury have a notable impact on the environment, since they are often detected in industrial wastewater (Ali and El-Bishtawi, 2012). Removal of ions can be an expert by a variety of techniques, in which adsorption method is currently considered very acceptable for water treatment because of its simplicity and cost success and zeolites is one of the adsorbents for the adsorption of a heavy metal. The presence of heavy metals in industrial wastewater as a result of many construct process is known to cause malignant effects on human health and environment (Selvi, *et al.,* 2011). Removing these heavy metals, demand high energy or advanced operational requirements, some conventional technologies like coagulation, precipitation, extraction, biosorption and adsorption have been considered for treatment of contaminated wastewater. Between these methods, adsorption is found to be very suitable for wastewater treatment because of its simplicity and cost effectiveness (Lei, *et al.,* 2017). Commercial activated carbon is considered as the most effective material for guide the metal ions load. Nevertheless, due to its high cost and 10%-15% lost through regeneration, unconventional adsorbents such as zeolites have attracted the attention of various investigations and adsorption characteristics have been widely investigated for the removal of metal ions (Amer, *et al.,* 2010). The aim of this study was to synthesize LTL zeolite type, which can be used as adsorbent for adsorption of Cd from aqueous solution. Additionally the effects of temperature, pH, Concentration and time were also studied to find out the maximum removal percentage, and applying isotherm models such as: Langmuir, Freundlich, and temkin isotherm models.

2. MATERIALS AND METHODS

2.1. Materials

An analytical grade of cadmium nitrate $Cd(NO_3)_2$ salt (Merck) was used to prepare the standard solution of cadmium. Aluminum foil (Aldrich), pyrogenic silica (SiO_2) (Aldrich), KOH (Merck), teflon-lined stainless steel autoclave. Zeolite LTL was used as an adsorbent. The stock solution was diluted to the needed concentration and appropriate pH with drop wise addition of 0.13M NaOH and 0.13M of HNO_3 using a pH meter. Freshly diluted stock solutions were used for each experiment. The concentration of metal ions was ponderous using atomic absorption spectrometer (GBC 932 plus) at the wavelength of 326 nm.

2.2. Zeolite LTL synthesis

In a typical experiment 0.40g of aluminum foil was dissolved in 50ml KOH and NaOH (0.3M) solution under stirring to obtain a clear solution followed by addition of 6.0g of pyrogenic silica. This particulate suspension was stirred over night at room temperature (25°C). After sealing in a teflon-lined stainless steel autoclave the mixed suspension was hydrothermally treated at 150°C for 1, 2 and 3h. The resulting solid masses were then washed with distilled water several times until the pH of washed liquid become 7.0. At the end the solid samples were dried at 60°C for 8h. (Rituparna, et al., 2014).

2.3. Characterization

Characterization of LTL zeolite formed was carried out by X-Ray Diffractometer (Siemens D5000) with radiation sources Cu Kα that has λ=0.154 nm at 40kV and current of 10mA. The diffractogram was scanned in the degree of 2θ at the range of 5-50 with the step size of 0.05. The morphology of LTL zeolite was elucidated using, FESEM and TEM (JEOL).

2.4. Adsorption procedure

The aqueous solution used, was cadmium stock prepared at different concentrations, for different runs, 0.25g of LTL zeolite was mixed with 25ml of the prepared cadmium stock solution at a particular concentration ($20mg.L^{-1}$ - $50mg.L^{-1}$), of a pH (4-10). The mixture was placed on a water bath constant temperature vibrator set at a particular temperature (303K-323K), for a particular duration/time (10min-60min). After adsorption, the solution was filtered and the filtrate's concentration was tested using Atomic Adsorption Spectrophotometer (AAS). The amount of equilibrium adsorption, Q ($mg.g^{-1}$) was calculated by

$$Q = \frac{(C_i - C_e)V}{m} \qquad (1)$$

Where C_i ($mg.L^{-1}$) is the Initial cadmium ion concentration in solution, C_e ($mg.L^{-1}$) is the equilibrium concentration of cadmium ion concentration in solution, V (liters) is volume of the solution manipulate, and m (g) is the mass of the adsorbent (Wang and Chen, 2006). The percentage adsorbed is given as;

$$Percentage\ adsorbed\ (\%) = \frac{C_i - C_e}{C_i} x\ 100$$

$$(2)$$

3. RESULTS AND DISCUSSION

Figure 1 shows the XRD of the synthesized zeolite sample LTL phase is found to match with the zeolite LTL and confirmed by contrast the diffraction peaks at 2θ degree, 5.55, 11.77, 14.71, 19.30, 20.47, 22.66, 23.35, 24.35, 26.21, 27.12, 27.97, 29.12, 29.66, 30.71, 34.21, 35.15 and 41.41. These peaks correspond to the planes [100], [001], [210], [220], [301], [221], [311] [320] [202] [321] [212] [330] [420] [222] [322] [412] and [313]. It can be seen from Figure 1 that all synthesized samples showed the formation of LTL zeolite phase (JCPDS File No. 43-560) was indicated. Figure 2 shows the FESEM image of the particles obtains hydrothermally at 150°C for 3h. It reveals the rod-shaped

morphology of zeolite LTL of the length of 5-10µm with the diameter ranging from 110-200nm. Interval Figure 3 shows TEM image also obeys the rod shaped morphology of zeolite LTL. The presence of multiple nanodomains causes a random alignment among nanocrystallites in the zeolite LTL rods (Zhang, *et al.,* 2005).
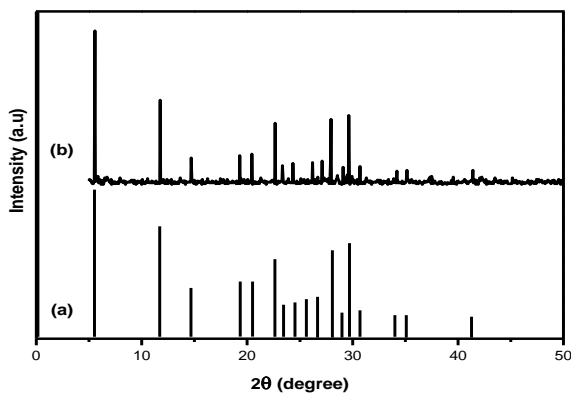
Figure (1): XRD patterns of (a) reference sample and

(b) synthesized LTL zeolite.
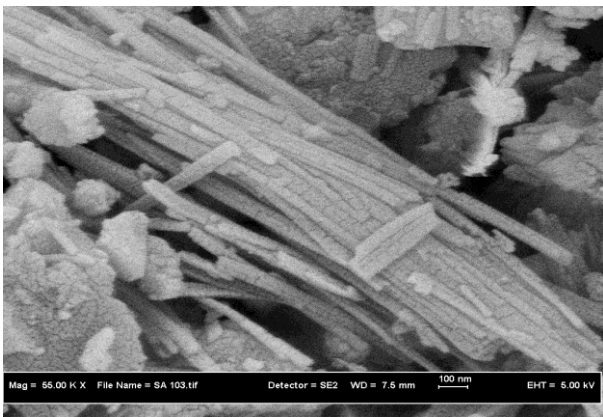
Figure (2): FESEM. Image of synthesized LTL
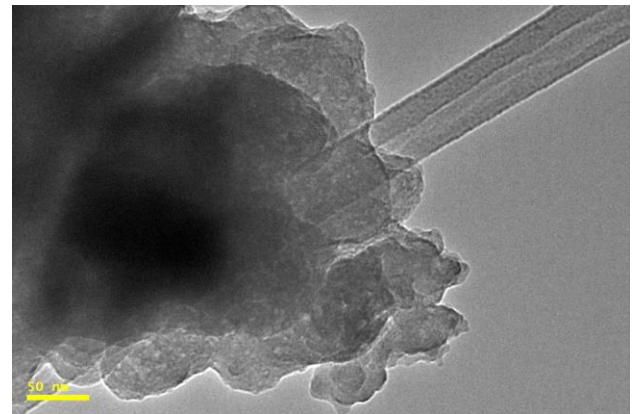
zeolite.

Figure (3): TEM. Image of synthesized LTL zeolite.

3.1. Effect of PH

The sequel of the pH of solution on adsorption was resolute because it is known to be one of the main factors affecting sorption. The result of the effect of pH on the adsorption of cadmium (II) ions is shown in Figure 4. The percentage of adsorption of cadmium was studied over a pH scope, and the result designated that maximum removal appeared at pH of 8.0. It has been reported that a relationship presence between the pH point of zero percentage removal of material, and proposed that cations adsorption on an adsorbent will be recommended at pH values above the pH point of zero, interval anions adsorption will be favored at lower pH worth. Although, metal precipitates at high pH values i.e. above pH of 8.0 impede the connect of a metal ion with the adsorbent. The decrease in sorption was noted with a further increase in pH and this may be attributed to the low solubility of cadmium at high pH. This result a good agreement with the literature reported in (Fan, et al., 2008).
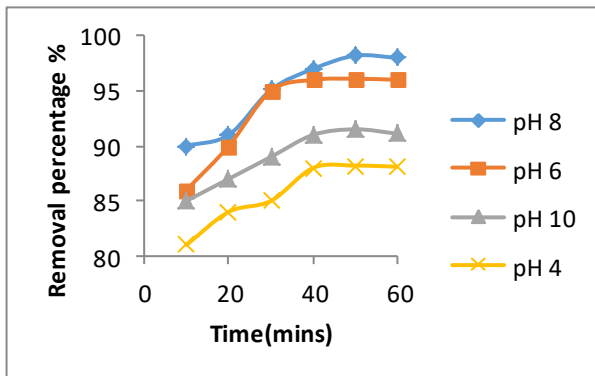
Figure (4): Effect of the pH on adsorption of cadmium on synthesized LTL zeolite.

Figure (5): Effect of concentration on adsorption of cadmium on synthesized LTL zeolite.

3.2 Effect of Concentration

The sequel of initial ion concentration was studied for the initial ion concentration between 20 to 50 mg.L^{-1} and the results were presented in Figure 5. The result showed that a decrease in the percentage removal with an increase in the concentration of cadmium was perceived. This can be reported for that all adsorbents have a fixed number of substances during a reaction and at a certain metal ion concentration the active sites suits used up and saturated (Vimala and Das, 2009). This involves that further increase in the concentration of cadmium will decrease in the percentage transfer as the active sites have been before occupied. Hence more metal ions will be surviving in solution after adsorption, the increase in the concentration of metal ions to an increase in a clash between the ions and adsorbent hence increased the power to overcome resistance to mass transfer and thus an increase in uptake capacity (Ross, 1980).

3.3. Effect of Temperature

Temperature values varying from 303K to 323K were used to study the effect of temperature on adsorption. The consequence of the effect of temperature is shown in Figure 6. It was found out that, with an increase in temperature, the time to reach the parallel percentage removal was abundant less. This is due to as the temperature increases, the rate of dispersal of adsorbate molecules across the external frontier layer and internal pores of the adsorbent particles increased. This consequence indicated that as the temperature of the solution was increased from 303K to 323K, There was also a corresponding increase in the amount of cadmium ions adsorbed by the synthesized LTL zeolite. This increase in adsorption capacity escorted by an increase in temperature designated that the adsorption process is endothermic in nature, it also recommends chemisorptions process i.e. adsorption accompanied by a chemical reaction. It is cramped to just on a layer of molecules on the surface but may be followed by a supplementary layer of physically adsorbed metal ions (Olin, *et al.,* 1998). A similar result has been reported (Amer, *et al.,* 2010; Akpomie, *et al.,* 2002). A good literature search has divulged different types of consequences on the upshot of temperature on

the adsorption of heavy metals. A decrease in adsorption potential accompanied by an increase in temperature has been perceived, the sight decrease at high temperature is probably due to the inhibiting effect of removal percentage which can be strongly adsorbed on the zeolite (Stumm, *et al.,* 1996).
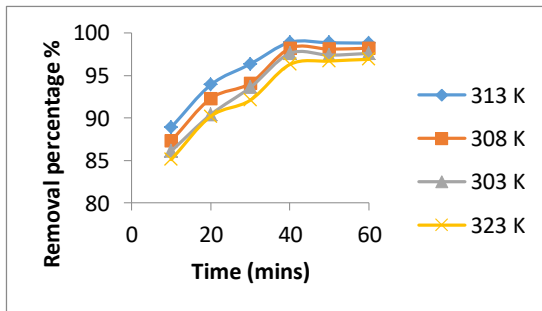
Figure (6): Effect of temperature on adsorption of

cadmium on synthesized LTL zeolite.

3.4 Effect of Time

All the batch studies were carried out on time. The study shows that as the time increases, the percentage adsorbed increases till equilibrium was reached at regarding 60mins. The initial adsorption was caused by the availability of the positively charged surface of the adsorbent. The influence of time is also the main factor to be contemplated on the adsorption of metal ions by an adsorbent. It has been described that the contact time plays a main role in the adsorption process. The fast rate of adsorption discovered at the initial stage may be explained by an availability of plentiful active sites on the adsorbent surface which gradually became occupied with time. As these sites are progressively filled the more difficult the sorption becomes as the process tends to become unfavorable (Kapica, *et al.,* 2002).

3.5 Isotherm Studies

Adsorption isotherm is usually described through isotherms, that is, the purpose which connects the amount of

adsorbate on the adsorbent. Dispersal of metal ions between the liquid phase and the solid phase can be delineated by several models of isotherm such as Langmuir, Freundlich and Temkin isotherm, etc. assumes monolayer adsorption onto a surface containing a limit number of adsorption sites of uniform schemes with no transmigration of adsorbate in the plane surface (Hameed, *et al.,* 2007). Once a site is packed, no further sorption can happen at that site. This indicates that the surface capacities a saturation point where the maximum adsorption of the surface will be achieved.

3.5.1 Langmuir isotherm model

The Langmuir isotherm is built on the theoretical principle that only a single adsorption layer exists on an adsorbent. It accepts that all active sites on the adsorbent are homogenous and there is no influence between active sites (Langmuir, 1916).

The linear shape of Langmuir equation is given as:

$$\frac{Ce}{qe} = \frac{1}{Q^\circ\,KL} + \frac{Ce}{Q^\circ} \qquad (3)$$

Hence a plot of Ce/ qe against Ce will give

$$Slope = \frac{1}{Q^\circ} \quad \text{and} \quad Intercept = \frac{1}{Q^\circ KL}$$

The Langmuir constants KL and Q° is the amount of adsorption was determined from the intercept and slope.

Langmuir model assumes that uptake of cadmium molecules occurs on a homogeneous surface by monolayer adsorption. For Langmuir isotherm, the values of specific adsorption (Ce/qe) were plotted against equilibrium concentration (Ce) and is shown figure 7 below. The Langmuir constant KL and Q° relate to the energy of adsorption and

maximum adsorption capacity was founded from the intercept and slope of the linear plot, and showed in Table 1. The crucial features of Langmuir adsorption isotherm parameter can be used to forecast the affinity between the sorbate and sorbent manipulating a dimensionless constant called separation factor (RL), which is expressed by the following relationship (Malik, et al., 2004):

$$RL = \frac{1}{(1+KL\ Ci)} \quad (4)$$

Where KL is the Langmuir constant and Ci is the initial concentration of Cd (II). The value of RL indicated the type of Langmuir isotherm to be irreversible (RL =0), linear (RL = 1), unfavorable (RL > 1), or favorable (0 < RL < 1) (McKay and Gardner, 1982). The RL values between 0 and 1 show favorable adsorption. The RL value in the present investigation was found to be 0.0983-0.1980, indicating that the adsorption of the cadmium ion onto synthesized LTL zeolite is favorable.

3.5.2 Freundlich isotherm model

The Freundlich isotherm describes the range of heterogeneity of the adsorbent surface demanding a multilayer adsorption (McKay and Gardner,1982). Freudlich equation is given as:

qe= Kf Ce 1/n   (5)

The linear form is

$$\log qe = \log Kf + \frac{1}{n}\log Ce$$

(6)

Where K*f* = Freundlich constants which correspond to adsorption capacity, n= adsorption intensity.

Freundlich isotherm involves an empirical model, where qe represents the amount adsorbed per amount of adsorbent at the equilibrium (mg.g^{-1}), Ce represents the equilibrium concentration (mg.L^{-1}), Freundlich equilibrium constants were determined from

the plot of logqe against logCe shown in figure 8. The values of the freundlich constants K*f* and n are parameters that depend on the adsorbate and adsorbent. Were indicated from the intercept and the slope individually then shown in Table 1. The constant K*f* is a measure of the adsorption capacity while constant n is a measure of the intensity or favorability of adsorption (Abdel-Fattah and Isaacs, 2003). For advantageous adsorption, the value of n will be between 1 and 10 represent good adsorption (Ozer and Pirinc¸ 2006). The n value designates the degree of nonlinearity between solution concentration and adsorption as follows: if the value of n=1, afterward adsorption is a straight line; if n<1, afterward adsorption is a chemical process; if n>1, afterward adsorption is the physical process. In this work, all the values scope from 3.5498 to 3.5549 showing beneficial adsorption of cadmium on the adsorbent. The circumstances n>1 is most habitual and may be due to a distribution of surface sites or any factor that sources a decrease in adsorbent adsorbate interaction with increasing surface density (Reed and Matsumoto, 1993). The correlation factor R^2 ranges from 0.9869 to 0.9937, indicating that the adsorption followed Freundlich isotherm model and n lies between 1 and 10 it indicates the physical adsorption of cadmium ions onto synthesized LTL zeolite so the process is favorable physical adsorption (Calace, *et al.,* 2002).

3.5.3 Temkin isotherm

The Temkin equation is given as:

$$qe = B\ln(ACe) \quad (7)$$

The linear form is

$$qe = B\ln A + B\ln Ce \quad (8)$$

qe = Amount adsorbed at the equilibrium, Ce = Equilibrium concentration.The constants A and

B were calculated; hence temkin isotherm was analyzed by plotting qe against lnCe as shown in figure 9. The values of constants A and B were calculated from intercept and slope respectively then the data was presented in Table 1. The correlation coefficient R^2 of about 0.8335 to 0.8743 indicates that cadmium

adsorption did not follow the temkin isotherm. Thus $R^2 > 0.91$ indicates adsorption follows temkin isotherm (Tempkin and Pyzhev, 1940).
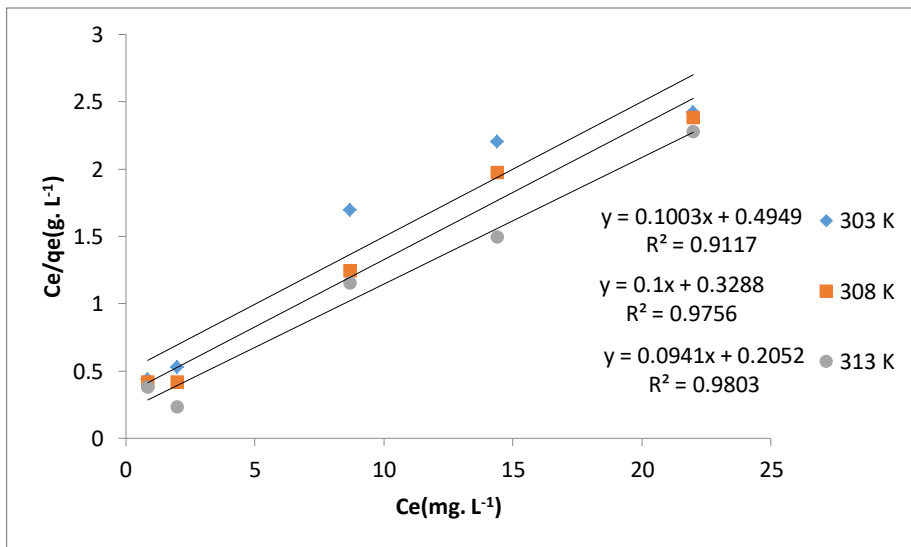
Figure (7): Langmuir isotherm for adsorption of cadmium on synthesized LTL zeolite.
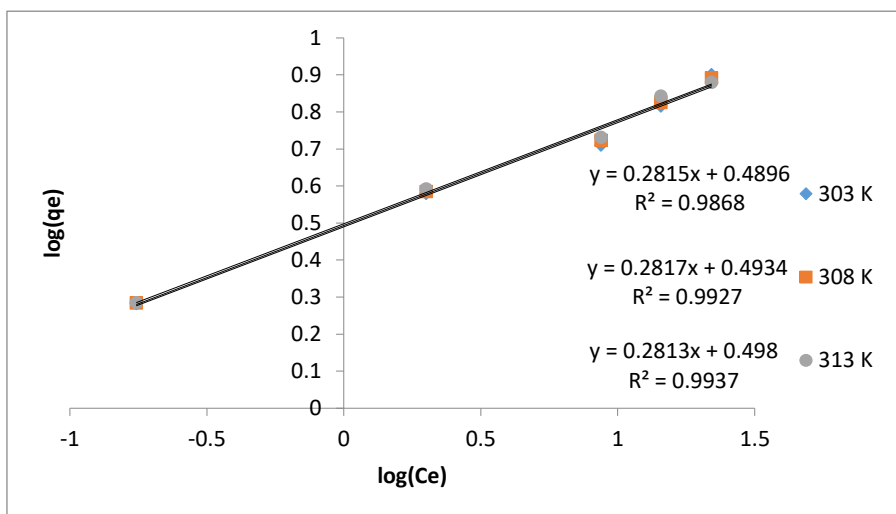
Figure (8): Freundlich isotherm for adsorption of cadmium on synthesized LTL zeolite.
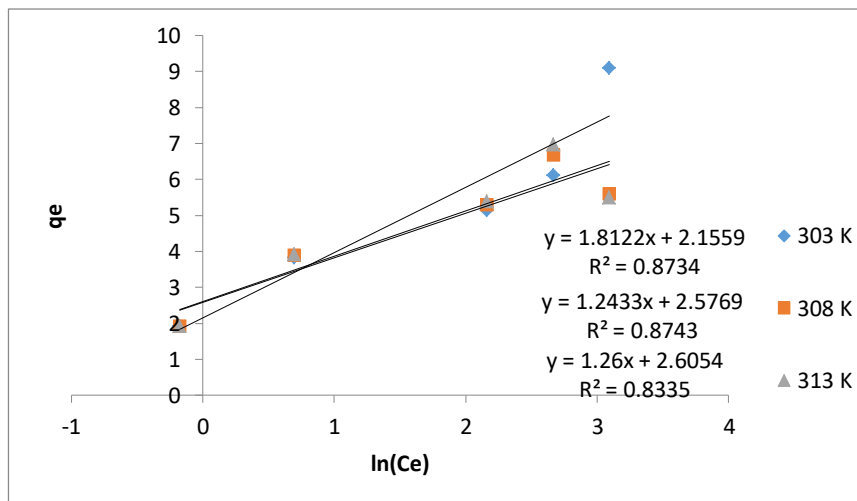
Figure (9): Temkin isotherm for adsorption of cadmium on synthesized LTL zeolite.

Table 1: Isotherm parameters for adsorption of cadmium ions onto synthesized LTL zeolite.

Isotherm models	Temperature (K)		
	303	308	313
Langmuir			
$Q°(mg.g^{-1})$	9.9700	10.0000	10.6269
$KL(L.mg^{-1})$	0.2026	0.3041	0.4585
RL	0.1980	0.1412	0.0983
R^2	0.9117	0.9756	0.9803
Freundlich			
n	3.5523	3.5498	3.5549
$Kf (L.mg^{-1})$	3.0874	3.1145	3.1477
R^2	0.9869	0.9927	0.9937
Temkin			
$A(L.g^{-1})$	3.2857	7.9454	7.9066
B	1.8122	1.2433	1.2600
R^2	0.8734	0.8743	0.8335

4. CONCLUSIONS

Our study for synthesizing zeolite LTL that can be used for removal of cadmium ion from aqueous solution showed that the best time for synthesizing LTL zeolite is 3h. Adsorption is a strong choice for removal of heavy metals from aqueous solution and the equilibrium data was found to fit the Langmuir and Freundlich models better than the Temkin model. From the Langmuir model the *RL* value in the existing investigation was less than one, indicating that the adsorption of the metal ion onto synthesized LTL zeolite is favorable, and according the obtained (n) value from Freundlich model the process is favorable physical adsorption. The maximum adsorption of cadmium occurred at a pH 8 and 313K. On the other hand increase in temperature improved adsorption performance for the zeolite; high metal uptake can be achieved with careful selection of slurry concentration to avoid masking of sorption by chemical precipitation. According to the results of our study the synthesized zeolite LTL showed promise as a highly efficient adsorbent for cadmium removal.

Conflict of Interest

REFERENCES

ABDEL-FATTAH, T. M. & ISAACS, L. K. 2003. Using organo-silicate nanocomposites for aqueous lead species removal. *American Chemical Society*, *Prepr. Ext.Abstr*, 43, 1138–42.

AKLIL, A., MOUFLIH, M. & SEBTI, S. 2004. Efficient Removal of La(III) and Nd(III) from Aqueous Solutions Using Carbon Nanoparticles. *J. Hazard. Mater.,* A112, 183.

AKPOMIE, G. K., ABUH, M. A., OGBU, C. I., AGULANNA, A. C. & EKPE, I. O. 2002. Adsorption of Cd(II) from solution by nsu clay: kinetic and thermodynamic studies. *J. Emerg. Tren. Eng. App. Sci,* 3, 254-8.

ALI, A. A. & EL-BISHTAWI, R. 2012. Removal of lead and nickel ions using zeolite tuff. *J.Chem.Technol. Biotechnol*, 69, 27–34.

AMER, M. W., KHALIL, F. I. & AWWAD, A. M. 2010. Adsorption of Lead, Zinc and Cadmium ions on polyphosphate modified Kaolinite clay. *J. Environ. Chem. Ecotox,* 2, 1-8.

CALACE, N., DIMURO, A., NARDI, E., PETRONIO, B.M. & PIETROLETTI, M. 2002. Adsorption isotherms for describing heavy-metal retention in paper mill sludgesǁ. *Ind. Eng. Chem,* 41, 5491–7.

DAWODU, F. A., AKPOMIE, G. K. & OGBU, I. C. 2012. Isotherm Modeling on the Equilibruim Sorption of Cadmuim (II) from solution by Agbani clayǁ. *Int. j. Multidisc. Sci. Eng,* 3, 9-14.

DENG, S. B. & TING, Y. P. 2005. Fungal biomass with grafted poly(acrylic acid) for enhancement of Cu(II) and Cd(II) biosorption. *Langmuir,* 21, 5940-8.

ENNIGROU, D .J., GZARA, L., BEN ROMDHANE, M. R. & DHAHBI, M. 2009. Desalination 246, 363.

FAN, T, LIU, Y. ET AL. 2008. Biosorption of cadmium (II), zinc (II) and lead (II) by Pencillium simplicissimum: Isotherms, kinetics and thermodynamics. *Journal of Hazardous Materials,* 160, 655-61.

HAMEDREZA, J., FOROUGH, G., HABIB-ALLAH, T. SEYEDMOSTAFA, H. 2015. Study of the adsorption of Cd (II) from aqueous solution using zeolite-based geopolymer, synthesized from coal fly ash; kinetic, isotherm and thermodynamic studies. *Arabian Journal of Chemistry*, 8, 837–49.

HAMEED, B., DIN, A. & AHMAD, A. 2007. Adsorption of methylene blue onto bamboo-based activated carbon: kinetics and equilibrium studies, *Journal of Hazardous Materials,* vol. 141, 819–25.

KAPICA, J., PELECH, R., PRZEPIORSKI, J. & MORAWSKI, A.W. 2002. Kinetics of the adsorption of copper and lead ions from aqueous solution on to WD-ekstra activated carbonǁ. *Adsorpt. Sci. Technol.* 20, 441–52.

LANGMUIR, I. 1916. The constitution and fundamental properties of solids and liquids. part i. solids. *J. Am. Chem. Soc.*, 38, 2221-30.

LEI, X., HONGBIAO, C., ZHENQIU, ZH., JIANI, L. & JING, Z. 2017. Equilibrium, Kinetic, and Thermodynamic Studies on the Adsorption of Cadmium from Aqueous Solution by Modified Biomass Ash. *Bioinorganic Chemistry and Applications.* 20, 1-9.

MALIK, P. 2004. Dye removal from wastewater using activated carbon developed from sawdust: adsorption equilibrium and kinetics. *Journal of Hazardous Materials,* 113, 81–8.

MCKAY, G., BLAIR, H. & GARDNER, J. 1982. Adsorption of dyes on chitin. *Journal of Applied Polymer Science*, 27, 3043–57.

MOHAMMADI, T., MOHEB, A., SADRZADEH, M. & RAZMI, A. 2005. Modeling of metal ions removal from wastewater by electrodialysis. *Sep. Purif. Technol.* 41, 73-82.

OLIN, T. J. & BRICKA, R. M. 1998. Zeolite: a single-use sorbent for the treatment of metals-contaminated water and waste streams. MIN. ENG. (LITTLETON, COLORADO), 50 , 61–6.

OZER, A. AND PIRINC, H. 2006. The adsorption of Cd(II) ions on sulphuric acid-treated

wheat bran. *Journal of Hazardous Materials,* 137, 849–55.

PRASAD, S., SAXENA, S., AMRITPHALE, S. S. & CHANDRA, N. 2000. Kinetics and isotherms for aqueous lead adsorption by natural minerals. *Ind. Eng. Chem. Res* 39, 3034–37.

REED, B. & MATSUMOTO, M. 1993. Modeling cadmium adsorption by activated carbon using the Langmuir and Freundlich isotherm expressions. *Separation Science and Technology,* 28, 2179–95.

RITUPARNA, D., SOURAV, G. & MILAN, K. 2014. Synthesis of single crystal L rods with high aspect ratio using rice husk ash. *Indian journal of chemistry.* 35A, 816-19.

ROSS, R.B. 1980. Metallic Materials Specification Handbook, 3rd Ed.; *E&NF Spon,Ltd*.: London.

SELVI, K, PATTABI, S. & KADIRAVELU, K. 2011. Removal of Cr(VI) from aqueous solution onto activated carbon‖. *Bioresource Technology,* 80, 87-9.

STUMM, W. & MORGAN, J. J. 1996. Chemical Equilibria and Rates in Natural Waters, 3rd Edi., *Aquatic Chemistry;* Wiley: New York, 260.

TEMPKIN, M. J. & PYZHEV, V. 1940. Kinetics of Ammonia Synthesis on Promoted Iron Catalysts. *Acta Physiochim,* 12, 217-22.

VIMALA, R. & DAS, N. 2009. Biosorption of Cadmuim(II) and Lead(II) from aqueous solution using mushrooms: a comparative study. *J. Hazard. Mater,* 168, 376-82.

VOEGELIN, A. & KRETZSCHMAR, R. 2003. Modelling sorption and mobility of cadmium and zinc in soils with scaled exchange coefficients. *Eur. J. Soil Sci.,* 54, 387-400.

WANG, J. AND CHEN, C. 2006. Biosorption of heavy metals by Saccharomyces cerevisiae: a review. *Biotechnol Adv.,* 24, 427-51.

ZHANG, Z., SUN, H., SHAO, X., LI, D., YU, H. & HAN, M. 2005. Three-Dimensionally Oriented Aggregation of a Few Hundred Nanoparticles into Monocrystalline Architectures. *Adv.mater.,*17, 42.
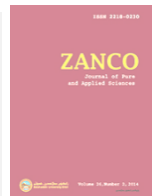
Electron Swarm Parameters in Germane – Argon Mixtures Using Boltzmann equation

Mohammad M. Othman, Sherzad A.Taha, Jwan J. Mohammad ,Ayoub S. Karem

Department of Physics, College of Education, University of Salahaddin, Erbil, Kurdistan Region, Iraq.

A R T I C L E I N F O

*Corresponding Author:
Mohammad M. Othman,
sherzad.taha@su.edu.krd

A B S T R A C T

A theoretical approach for calculating the electron swarm parameters in German – Argon (GeH_4-Ar) mixtures has been calculated by using two-term solution of the Boltzmann method in the range of E/N varying from 0.04 to 100 Td ($1Td=10^{-17}$ $V.cm^2$).These parameters namely, electron energy distribution function, characteristic energy, electron mobility. The ionization coefficients in addition to the electron drift velocity have also been calculated. The effect of the reduced electric field strength **E/N** on these parameters has been investigated, and compared with the available experimental data. Excellent agreements have been founded which suggest that the present approach is sufficient for computing the electron swarm parameters via two-term analysis.

1. INTRODUCTION

A lot of physical problems need to description the non-stationary high discharge in non-isothermal spastically homogeneous plasma. Electron kinetics simulated by using two term solution of Boltzmann equation, taking into account anisotropy of electron energy, ie. Gas laser afterglow discharge, application of RF discharges and swarm method for calculation of electron atom/molecules cross section from swarm data.

In non-isothermal, partially ionized plasma that degree of ionization is less than 1, effected by applied electric field the non-stationary electron behavior calculated by the input power and collisional power dissipation to atom/molecules in elastic and inelastic collisions undergo to different types of excited state. Because of low ionization level of under 10^{-5}, electron-electron and electron-ion are neglected. The plasma instabilities are less significance. When the plasma state reach to non-equilibrium, the transport parameters and electron collision cross section from swarm experimental swarm data calculated by using two–term solution of Boltzmann equation during the past decade (Huxley, 1974, Pichford, 1982, Rumble, 1981).

The study of the electron energy distribution function (EEDF) in ionized gases important for the quantitative understanding of gas discharges, plasma physics, laser physics. One of the most common techniques to obtain the distribution function is the solution of the Boltzmann equation using the Lorentz approximation (Zoltan and Nikolay, 2016). The role of electron swarm parameters is an important one because it provides a link

between electron gas collision cross section and gas breakdown and discharge phenomena. The swarm parameters may be directly calculated from a set of collision cross section by using either the Boltzmann equation or Monte Carlo simulation method (Yousfi and Benabdessadok, 1996).

A product of such calculations is the electron energy distributions also evaluated the percentage of energy loss by different collision processes. Once the validity of the swarm parameters are assured, they may be used to explain pre- breakdown and breakdown phenomena as well as providing sum information for understanding of discharge (Colonna and D'Angola, 1996, Bychkov *et al.*, 2014).

Germane (GeH₄) is a colorless, flammable and high toxic gas, heavier than air.Its structure analogue to silane (SiH₄) and methane (CH₄) gas. Germane molecules has been used in depositing hydrogenated amorphous silicon-germanium (a-SiGe:H) thin films by metal organic vapor phase epitaxial or chemical beam epitaxial (Venkatasubramanian *et al.*,1989). Because of complex structure of the germane molecule the basic plasma processes have not been understood. In particular for germane molecules mixed with gases are the most fundamental in understanding the physics in plasma to fabricate thin film by etching and deposition in micro electron device fabrication (Gorur *et al.*, 2012). Several industrial applications can be made using low-temperature plasmas such as the production of integrated circuits that involves deposition and etching (Mario *et al.*, 2016).

Since (GeH₄) is mixed with Ar in semiconductor fabrication plasma processes, to study the electron swarm parameters for these mixtures under effect D.C. electric field, a set of elastic and inelastic cross section required. Modeling and simulation of discharge used for this processes (Soejima and Nakamora, 1993).

The calculated values are obtained by suitably averaging over the electron energy distribution function (EEDF), which is itself obtained by using the cross sections as input to a Boltzmann solver (Morgan and Penetrante, 1990). Theoretical method was used to study the plasma discharge in Ar-Cl₂ mixtures, using Boltzmann equation (Smith and Thomson, 1978). In present work we explained that a small amount of (GeH₄) effected the electron energy distribution function in GeH₄-Ar mixtures by two term solution of Boltzmann equation using the numerical NOMAD code, D.C. discharge is applied (Rockwood and Greene, 1980).

The drift velocity and longitudinal diffusion coefficient of electrons were measured in the 0.210% and 0.980% GeH₄-Ar mixtures for the first time (Soejima and Nakamora, 1993). We have extended our study to the mixtures (0.21%, 0.98%, 2%, 5% and 10% GeH₄-Ar mixtures for the second time.

The object of this paper is to calculate the (EEDF) and the electron swarm parameters in GeH₄-Ar mixtures in the range 0.04 Td to 100 Td where (1 Td = 1 X 10^{-17} V.cm^2) and comparison with experimental results. The calculation was analyzed by using two term approximation of the Boltzmann equation.

2. Theory

The fundamental equation governing the electron distribution function is the Boltzmann equation. For spatially uniform gas in the presence of the steady electric field, the spatially homogeneous Boltzmann equation for electrons is given by (Morgan and Penetrante, 1990):

$$\frac{\partial f(v)}{\partial t} - \frac{eE}{m}\nabla_v f(v) = C \tag{1}$$

Where C is the collision integral, which, in the present study, accounts for the following processes: elastic scattering of electrons from atoms (the corresponding part of the collision integral is designated as C_m), excitation of electronic states and ionization of atoms by electron impact from the ground state (C_{in}), as well as electron-electron collisions (C_e):

$$C = C_m + C_{in} + C_e \tag{2}$$

The conventional method of solving equation (1) is based on the expansion of the distribution function *f* (**v**) in Legendre polynomials, $P_n(\cos\Theta)$. Retaining the two

irst terms only we arrive at the two-term approximation:

$$f(\mathbf{v}) = f_0(v) + f_1(v) \cos\Theta, \quad (3)$$

Where v is the magnitude of the velocity, Θ is the angle between $\mathbf{v}$ and $-\mathbf{E}$, $f_0(v)$ is the symmetrical (isotropic) part of the distribution function and $f_1(v)$ (the anisotropic part) describes the directed motion of the electrons along the electric field. In weakly ionized gases, most collisions occur between electrons and neutral atoms, the collisions between electron-electron and electron-ion are rare.

3. Transport Coefficients

The swarm parameters are defined in term of the collision cross section (Q) and the electron energy distribution f(u, E/N) as follows: The relation between drift velocity and electron energy distribution function is (Al-Amin and Lucas, 1988):

$$v_d = -\frac{1}{3}\left(\frac{2e}{m}\right)^{1/2}\frac{E}{N}\int_0^\infty u\left[\sum_s \delta_s Q_{sm}(u)\right]^{-1}\frac{df}{du}du \quad (4)$$

where , $\delta_s = \dfrac{N_s^j}{N_s}$ represents the fractional

concentration of the (s) species and N_s^j is the number of molecules of species (s)in the excited state (j). Where the energy distribution is constant in time and space and normalized by

$$\int_0^\infty u^{1/2} f_o(u)\,du = 1 \quad (5)$$

The mobility is defined as the proportionally coefficient between the drift velocity of a charged particle and electric field. The mobility of electrons is:

$$\mu_e = \frac{e}{mv_m} = \frac{v_d}{E} \quad (6)$$

v_m Represent the electron momentum transfer frequency, the electron mobility decreased with E/N increase; these occurrence energy loss results of an electron through the collisions between electrons and neutral molecules. From the computed drift velocity,

the electron mobility μ is obtained as (Ridenti et al., 2012);

$$\mu N = -\frac{1}{3}\left(\frac{2e}{m}\right)^{1/2}\int_0^\infty \frac{u}{\sum_s \delta_s Q_{sm}(u)}\frac{df}{du}du \quad (7)$$

The diffusion coefficient D is given by (Al-Amin and Lucas, 1988):

$$DN = \frac{1}{3}\left(\frac{2e}{m}\right)^{1/2}\int_0^\infty \frac{u}{\sum_s \delta_s Q_{sm}}f(u)du \quad (8)$$

If the distribution is not Maxwellian, the Einstein relationship is useful in defining a characteristic energy (Christophorou and Hunter, 1984)

$$\varepsilon_k = \frac{eD}{\mu} \quad (9)$$

Using the distribution function one can compute the electron mean energy (Morgan and Penetrante, 1990),

$$<\varepsilon> = \int_0^\infty f(u)u^{3/2}du \quad (ev) \quad (10)$$

For a Maxwellian energy distribution

$$\frac{2}{3}\langle \varepsilon \rangle = \frac{D}{\mu}$$

The primary ionization coefficient is a basic parameter in discharge physics and is defined as the number of ionizing collisions made by an electron in moving (1 cm) in the direction of the applied electric field. The coefficient is used in describing the behavior of a swarm of electrons traveling through a gas is the ionization coefficient (Frost and Phelps, 1964),

$$\frac{\alpha}{N} = \frac{1}{v_d}\left(\frac{2e}{m}\right)^{1/2}\sum_k \int_I^\infty \frac{N_k}{N}Q_i(u)f(u)u\,du \quad (cm^3/s) \quad (11)$$

where e and m are the charge and mass of the electron, N_k/N the relative concentration of the k- component, v_d is drift velocity given by equation (4), (I) is the ionization onset energy, and $Q_i(u)$ are ionization cross-section. The values of $f(u)$ are calculated from Boltzmann's equation using all the collision cross sections.

4. Cross Section

We use the argon cross sections from our calculation for electron swarm parameters. The momentum transfer cross section was

ken from Frost and Phelps (Frost and elps, 1964), and the sets of excitation cross sections were taken from Chutjion and Cartwright (1981). The ionization cross sections having onset energy 15.8eV is taken from Rapp and Englander-Golden (1965). To obtain the best agreement with experimental and theoretical swarm data, it was necessary to reduce the magnitude of some of these cross sections. For GeH4 the momentum transfer cross sections, vibrational excitation cross sections and ionization cross section having onset energy 12.3eV is taken from Soejima and Nakamora (1993).

5. Results and Discussions

Germane (GeH4) has been widely used as an amorphous thin film in plasma processing, thus we need sets of electron collision cross sections for (GeH4). Germane is an active the main attaching constituent in the mixtures, it different from argon gas that have two vibration and electronic levels in addition to the ionization with threshold energy 12.3 eV.

The electron swarm parameters as functions of **E/N** for the binary mixtures GeH4-Ar have been calculated in the E/N range 0.04 Td < **E/N** < 100 Td by a two term solution of the Boltzmann equation.

The influence of different discharge parameters on the electron distribution function is shown in figure (1). The EEDF is strongly affected by a change of the gas mixture, the figure shows the change of distribution function with the growth of the portion of Germane (GeH4) at the constant value of the electric field strength **E/N**. Therefore, for the distribution functions at **E/N**= 10 Td in two gases GeH4 and Ar quite different and the distribution function for the mixture 10% GeH4-90%Ar is different as shown in figure (1). This is because of the threshold energy at the vibration level 0.1015eV in the case of GeH4 gas. For this reason, the inelastic collision of an electron with GeH4 molecules occurs at low value of **E/N**. Therefore, the number of electrons at low energy increases at specified **E/N** value and they will also increase as a result of increase of GeH4 gas concentration in the mixture.

The electron at high energy suffers inelastic collisions with Argon atoms, the Germane gas molecules causing these atoms and molecules to be excited to higher different electronic levels. However, electron kinetic is strongly affected by the electric field and also by inelastic collisions due to the inefficiency of elastic collision in the energy transfer. It is seen from the shift of the curve that the 10% GeH4-90%Ar mixture reduce the mean energy of electrons. A significant shift of tails of EEDF on pure Argon towards higher energies results from different mechanisms of electron energy dissipation through the inelastic collision in this gas.

The best set of cross - sections for germane molecules used to calculate swarm parameters (drift velocity and diffusion coefficient) are shown by dashed lines in figures (2 and 3). This cross - sections are shown to give very good agreement between present calculation and measured drift velocity and diffusion (Soejima and Nakamora, 1993) in mixtures 0.21% and 098% GeH4 in Argon. The calculated values in pure Germane and Argon are also shown in the same figure. Drastic changes in drift velocity were observed by adding small amounts of GeH4 into Ar, because of momentum transfer and vibrational excitation sections of GeH4 at low energy. As shown in figure (2), drift velocities showed negative differential conductivity over the **E/N** range 0.1 to 0.4 Td in the 0.21% mixture and over range 2.5 to 6 Td in the 0.29% mixture, the decrease was not smooth but contained a small hump when the concentration of GeH4 in mixtures is small.

The calculated electron drift velocities in GeH4-Ar mixture gases are shown in figure(4), the drift velocity values in GeH4-Ar mixture gases are suggested to be between those of the pure gases over the range of **E/N** > 6 Td. In the range of **E/N** > 6 Td, the drift velocity values in these binary mixtures are higher than those of GeH4, especially on E/N = 2 Td corresponding to electron energy of about 0.1015 eV. To the best of our knowledge, the electron drift velocity strongly depends on momentum transfer cross sections and vibrational excitation cross sections. In these cases, the reasons could be suggested

t at this energy the vibrational excitations GeH$_4$ gas occurred, the momentum transfer cross section of GeH$_4$ gas is higher than that of Ar gas and the momentum transfer cross sections of GeH$_4$ and Ar gases are deeply decreasing to the minimum points (Soejima and Nakamora, 1993).

The electron drift velocities in the GeH$_4$–Ar mixtures are very sensitive to the mixture ratio of the GeH$_4$ molecule, especially in the low E=N range. Small regions of the NDC in these binary mixtures are observed in the **E/N** ranges of 0.3-4Td for 0.21%GeH$_4$–Ar, 0.6–6Td for 0.5%GeH$_4$-Ar, 1-10Td for 2%GeH$_4$-Ar, 2-20Td for 5%GeH$_4$-Ar and 4-20Td for the 10%GeH$_4$-Ar mixtures. The occurrences of these phenomena are due to the Ramsauer–Townsend minimum (RTM) of the elastic momentum transfer cross sections of the GeH$_4$ molecules, and the Ar atom. At a higher **E/N**, the electron drift velocities in 2, 5, and 10% GeH$_4$–Ar mixtures are close to that in pure GeH$_4$. This is due to dominant inelastic collision processes in the swarm shifting from those proceed by the vibrational excitation of the GeH$_4$ molecule to those caused by electronic excitations of the majority Ar atom because the mean energy of the electrons is enhanced at a higher **E/N**.

The characteristic energy as a function of **E/N** is shown in figure (5), the calculated values of characteristic energy for pure Germane are also shown in the same figure for comparison. The characteristic energy increases as a function of **E/N**, but at a specified value of E/N the characteristic energy decrease by increasing GeH4 in mixtures.

The electron mobility is also one of the important parameters of electron swarm behavior, like the drift velocity. The dependence of electron mobility on E/N for different GeH$_4$ content in the mixture is shown in figure (6). The behavior of the electron mobility decreases with increasing GeH4 concentration in the mixture at fixed E/N (0.01 to 1 Td), while the dependence of electron mobility on the partial concentration of GeH4 is reversed in the range 1 to 100 Td. For comparison, the calculated values for pure Germane are also shown in the same figure. Although electron mobility strongly depends on the amount of Germane in Argon and the parameter approximated to that in pure Germane at higher **E/N**, it depends on **E/N**. It should be noted that the hump in electron mobility occurred at roughly the same **E/N**.

The calculated ionization coefficients in GeH$_4$-Ar mixture gases are shown in figure (7). The variation of ionization coefficient α/N, with **E/N** for pure GeH$_4$ and Ar are also shown in the same figure, the α/N values in GeH$_4$-Ar mixture gases are suggested to be between those of the pure gases over the ranges of **E/N** > 4 Td. For pure Argon, the ionization coefficient is higher than the value of ionization coefficient in pure Germane over the same range of **E/N**. There are five further curves between the ranges mentioned later, with different mixtures of GeH$_4$ and Ar, i.e 0.21%, 0.98%, 2%, 5% and 10% GeH$_4$ in Argon, respectively. As shown in figure (7), the increase of GeH$_4$ content in mixture decreases the ionization coefficient. However, the growth of the inelastic collisions of electrons with germane molecules which are proportional to their concentration, reduce the number of fast electrons and causes lowering of ionization coefficient at higher concentration of the GeH$_4$ in the mixture.

6. Conclusion

The electron EEDF and transport coefficients (electron drift velocity, longitudinal diffusion coefficient, electron mobility, ionization coefficient) in binary mixtures of GeH$_4$-Ar was calculated by a two-term solution of the Boltzmann equation for the range (0.04 $\leq$**E/N**$\leq$ 100 Td) in the 0.21%, 0.98%, 2%, 5%, and 10% GeH$_4$-Ar mixture. Drastic changes in swarm parameters were detected by adding Germane into Argon. The drift velocity of electrons showed an unusual negative differential conductivity, with the decrease in the drift velocity not being smooth but having a small hump in both mixtures. These observed feature in the electron swarm parameters are due to the inelastic processes of germane molecules, possibly vibrational and electronic excitation. Models of gas discharge plasmas could be constructed using the binary mixture gases of GeH$_4$ gas with a high concentration of Argon.

References

A. Chutjian,, D. C. Cartwright, "Electron-impact excitation of electronic states in argon at incident energies between 16 and 100 eV", Phys. Rev.A, Vol.23, No. 5, pp. 2178-2193, 1981.

Bychkov, V.L., Golubkov, G.V. and Nikitin, A.I., The Atmosphere and Ionosphere, Springer, 2014, chpt.2, pp. 69-111.

Christophorou, L.G., Hunter, S.R, Electron-Molecule Interactions and Their Applications, vol. 2, pp. 318–412. Academic Press, Florida (1984)

D. Rapp, P. Englander-Golden, "Total Cross Sections for Ionization and Attachment in Gases by Electron Impact. I. Positive Ionization" , J. Chm. Phys., Vol.43, No.5, pp.1464-1479, 1965.

G. Colonna and A. D'Angola, Plasma Modeling Methods and Applications, pp. 2-23, IOP Publishing Ltd , 2016 .

Gorur Govinda Raju,, Gaseous Electronics, Tables, Atoms, and Molecules, CRC Press, 2012.

H. Soejima and Y. Nakamora, Measurement of electron swarm parameters in GeH4-Ar mixtures, J. of Vacuum Science, A. 11, 1161-1164, 1993.

K. Smith and R. M. Thomson," Computer Modeling of Gas Lasers", Plenum Press, 1978.

L. S. Frost and A. V. Phelps, "Momentum transfer cross section for slow electrons in He, Ar, Kr and Xe from transport coefficient", Phys. Rev. , Vol.136, pp. A1538-A1545, 1964.

L.C. Pichford and A.V. Comparative calculations of electron-swarm properties in N_2 at moderate E/N values, Phelps, Phys. Rev., A25, pp. 540-554, 1982.

L.C. Pitchford, S.V. ONeil, and J.R. Rumble, Extended Boltzmann analysis of electron swarm experiments, Phelps, Phys. Rev., A23, pp. 294-304, 1981.

L.G.H. Huxley and R.W. Crompton, The diffusion and drift of electrons in gases, New York, whily, 1974.

M. A. Ridenti, J. Amorim and V. Guerra, " A numerical solver for the homogeneous Boltzmann Equation" Physics Proceeding, XI Young Researchers Meeting, pp.6-5, March, 2012.

M. Yousfi and M.D. Benabdessadok, Boltzmann equation analysis of electron molecule collision crosses sections in water vapor and ammonia, J. Appl. Phys. Vol. 80, pp. 6619-6629, 1996.

Mario Capitelli, Roberto Celiberto, Gianpiero Colonna, Fabrizio Esposito, Claudine Gorse, Khaled Hassouni, Annarita Laricchiuta and Savino Longo. Fundamental Aspects of Plasma Chemical Physics: Kinetics, Springer, New York 2016.

S. A. J Al-Amin and J. Lucas, "Electron swarm in mixtures of metal vapour and argon gas", J. Phys. D: Apli. Phys., Vol.21, No.8, pp.1261-1270.1988.

S.D. Rockwood and A.E. Greene, "Numerical solutions of the Boltzmann transport equation", Computer Physics Communications, Vol.19, No. 3, pp. 377-393,1980.

Venkatasubramanian, R., Pickett, R. T.and Timmons, M. L. , "Epitaxy of germanium using germane in the presence of tetramethylgermanium". Journal of Applied Physics. Vol.66, No. 11, pp. 5662–5664, 1989.

W.L. Morgan, and B.M. Penetrante," ELENDIF: A time-dependent Boltzmann solver for partially ionized plasmas", Computer Physics Communications, Vol.58, No. 1-2, pp. 127-152,1990.

Zoltan ,Donko1, and Nikolay Dyatko, First-principles particle simulation and

oltzmann equation analysis of negative differential conductivity and transient negative mobility effects in xenon, Eur. Phys. J. D, Vol. 70, pp. 135-146, 2016,.
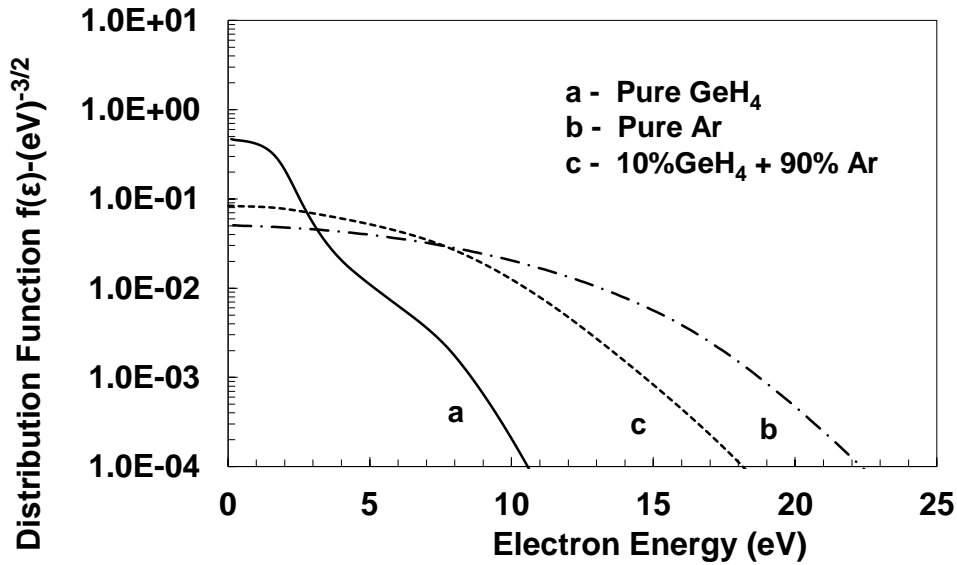
Figure (1): Comparison of calculated electron energy distribution function (EEDF) at E/N=10Td. Solid line GeH$_4$, dashed line 10%GeH4+90%Ar, dotted line pure Ar.
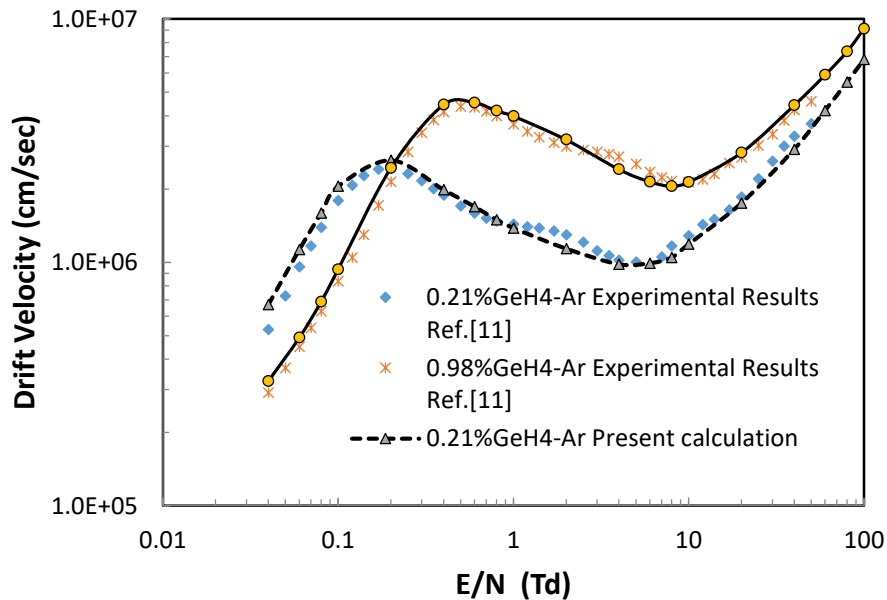
Figure (2): Electron drift velocity as a function of E/N in GeH$_4$-Ar mixtures with comparison with experimental results.
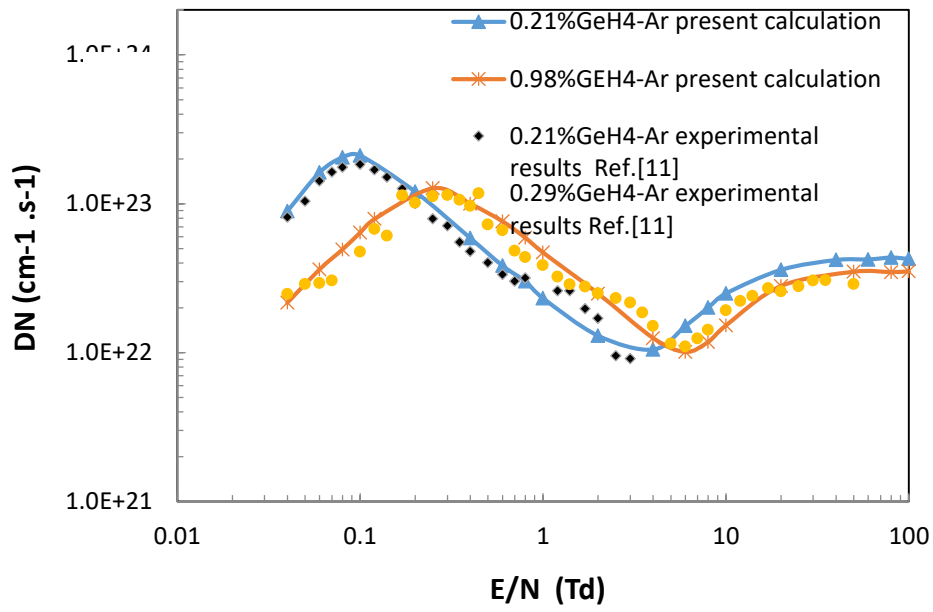
Figure (3): Density-diffusion coefficient as a function of E/N in GeH$_4$-Ar mixtures with comparison with experimental results.
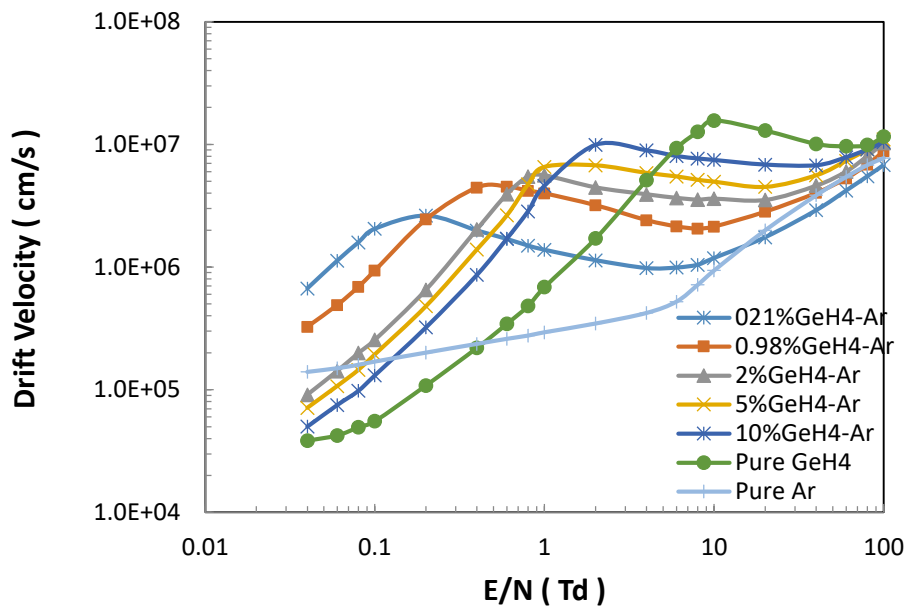
Figure (4): Electron drift velocity as a function of E/N for various GeH$_4$-Ar gas mixtures.
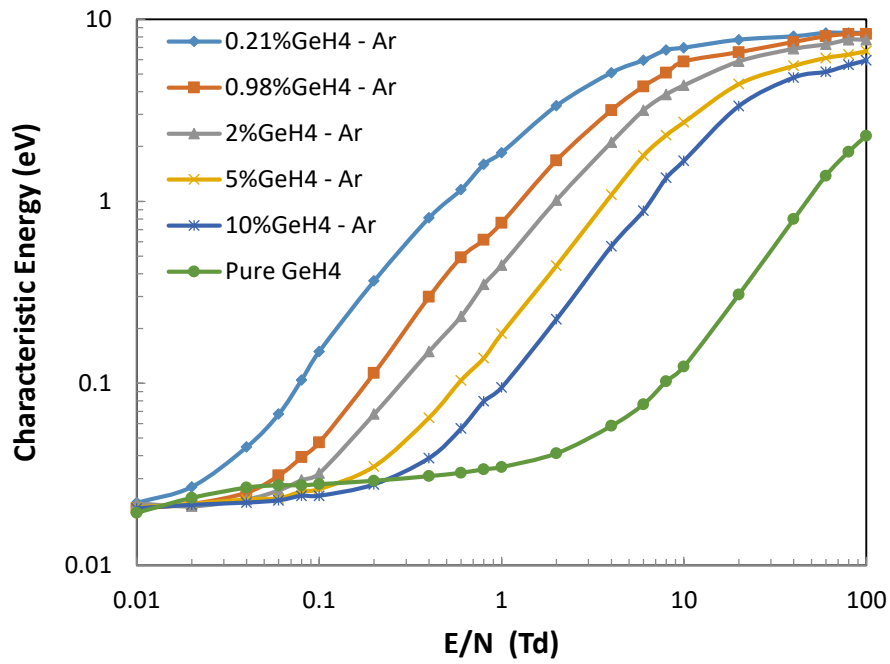
Figure (5): The characteristic energy as a function of E/N for various GeH$_4$-Ar gas mixtures
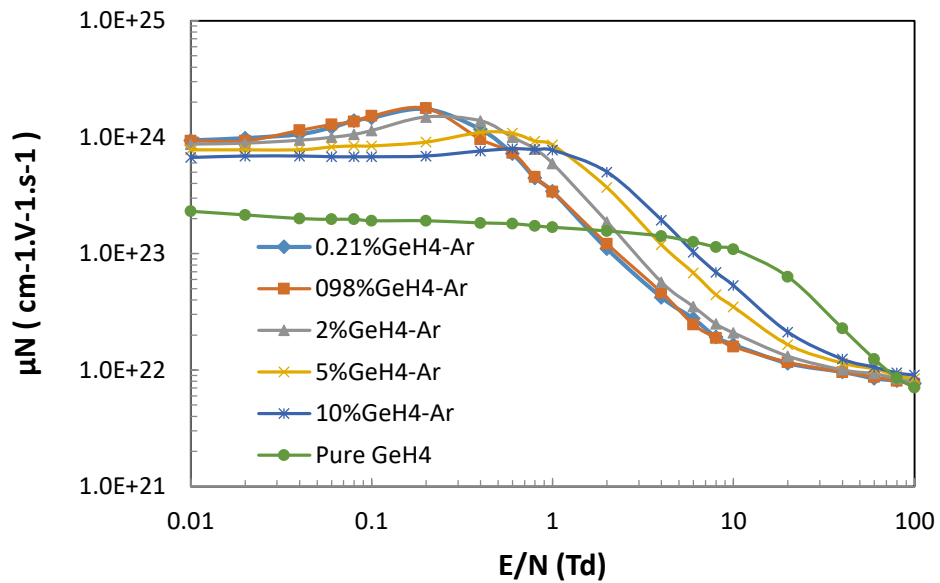
Figure (6): The electron mobility as a function of E/N for various GeH$_4$-Ar gas mixtures.
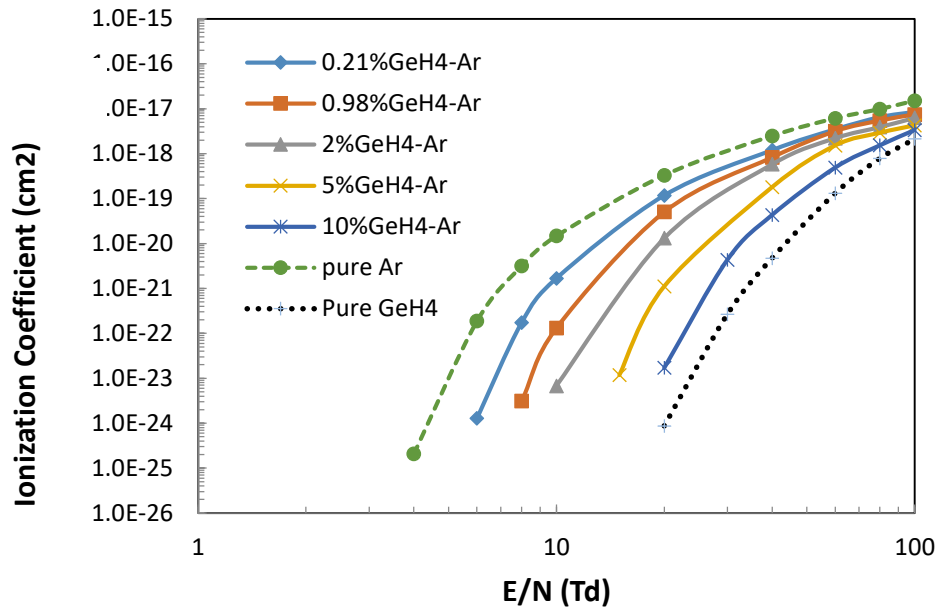
Figure (7): The ionization coefficient as a function of E/N for various GeH4-Ar gas mixtures.

Synthesis and spectroscopic study of 1,2-thiazine system incorporating various ester groups

Aras Najmaddin Hamad[1,2], Hassan Ahmed Mohammed[3]

[1]Pharmaceutical Chemistry Department, College of Pharmacy, Hawler Medical University, Erbil-Kurdistan Region, Iraq

[2] Pharmacy Department, Aynda Private Technical Institute, Erbil-Kurdistan Region, Iraq

[3] Chemistry Department, College of Science, Salahaddin University, Erbil-Kurdistan Region, Iraq

A R T I C L E   I N F O

*Corresponding Author:
Aras NAjmadin Hamad
dr.aras_naj@pha.hmu.edu.iq

A B S T R A C T

A series of 3-substituted-methyl-1,2-thiazines (4 a-g) was exclusively obtained in high yields for the first time through nucleophilic substitution reaction of 4,6-dibromo-2- phenyl-5-methyl-3-bromomethyl-1,1-dioxo-1,2-thiazines (3) with each of sodium Formate, acetate, propanoate, glycinate, benzoate, glycolate and salicylate as nucleophilic reagents in a highly polar aprotic solvent at room temperature. The IR, ^{1}H- and ^{13}C-NMR and MS spectra of the prepared compounds were conformed to their proposed structures

1. INTRODUCTION

The treatment of infectious diseases still remains an important and challenging problem because of a combination of factors including emerging infectious diseases and the increasing number of multi-drug resistant microbial pathogens. In spite of a large number of antibiotics and chemotherapeutics available for medical use, at the same time the emergence of old and new antibiotic resistance created in the last decades revealed a substantial medical need for new classes of antimicrobial agents

and is very important to explore additional sources for substances with potential antimicrobial activity, which could possibly have different modes of activity or affect different sites in the bacterial and fungal cells [*aras 2016*]. Compounds incorporating ester moiety play an important role in modern drug discovery and medicinal chemistry, and have long been used as anti-cancer [*Claudriana et al 2013, Azmat et al 2013 and Shima et al 2013*], anti-bacterial [*Bartzatt et al 2004 and Bartzatt et al 2003*], anti-fungal [*Boussalah et al 2013, Martin et al 2012 and HUHTANEN and GUY*], anti-viral [*Nothias et al 2015 and Hisashi et al 2011*] , anti-inflammatory [Bassem et la 2013 and Mounir et al 1985], anti-convulsant [Mariia et al 2016 and Waters et al 1986], anti-diabetic [Vaiyapuri and Shruthi 2014]   And also as stimulate hair growth agents [*Joseph and Gregory 2001*]. Looking to the diversified biological activities an attempt was made on the way to synthesis a series of new 1,2-thiazine system   incorporating various ester moieties as outlined in Scheme 1.

2. MATERIALS AND METHODS

Uncorrected melting points were determined in open capillaries on a Gallen Kamp electrothermal apparatus. IR spectra were recorded on a Thermo-Mattson-300 Spectrophotometer, as KBr disc (Chemistry Department, College of Science, Salahadden University/Erbil), 1H and 13C-NMR spectra were measured using a Bruker ultra shield 300 MHz with internal TMS (Central Lab., Al-al-Bayt University/ Jordan), chemical shifts are given in ppm. MS were recorded on a GCMS, shimadzu, QP505 and Lc/MS/API5000 (Pharmaceutical research Unit, Amman-Jordan).

2.1. Synthesis of 3,5-dimethyl-2-phenyl-1,1-dioxo- 1,2-thiazine (2) :-

A mixture of (200 mmol) of 3,5-dimethyl 1,1-dioxo-1,2-oxathine (1) (which prepared by [Fanghanel et al 1982] from the reaction of mesityl oxide, acetic anhydride and sulfuric acid at 0 ^{0}C for 48h) and (210 mmol) of aniline was heated at 130-135 ^{0}C for about 1-1.5 h. Then the reaction mixture was cooled to room temperature and 100 mL of 10% cold HCl solution was added, the obtained product was collected by filtration, washed several times with cold water then air-dried and recrystallized from methanol. Pale yellow; yield 47%; m.p.: 112-114; FT-IR (KBr) cm^{-1}:1152.2s, 1384.0s (SO$_2$); ^{1}H-NMR (CDCl$_3$, 300 MHz): 1.894 (s, 3H, 5-CH$_3$); 2.115(s, 3H, 3-CH$_3$);5.654 (s, 1H, 4-CH); 6.210 (s, 1H, 6-CH); 7.363-7.4 (m, 2H, **HBz**); 7.445-7.478(m , 3H, **HBz**); ^{13}C- NMR (CDCl$_3$, 300 MHz): 144.002 (C3), 106.874 (C4), 145.196 (C5), 111.936 (C6), 21.452 (C3-CH$_3$), 21.888 (C5-CH$_3$), 134.120 (C7), 129.464 (C8,8-), 129.928 (C9,9-),   129.516 (C10). MS (m/z, (relative abundance, %): 235.3(81.5),   236.3(24.1), 237.3(8.1),   170.2(100),   171.2(82.8), 156.2(48.2),   129.1(52.9),   115.1(37.9), 77.2(97.1), 67.1(), 51.1(79.5).

2.2. Synthesis of 4,6-dibromo-2-phenyl-5-methyl-3-bromomethyl-1,1-dioxo-1,2-thiazine (3):-

4,6-dibromo-2-phenyl-5-methyl-3-bromom-eth-yl-1,1-dioxo-1,2-thiazine (3) was prepared according to the method of [Fanghanel et al 1983]. Pale yellow; yield 55.3%; m.p.:160-162 ^{o}C; ^{1}H-NMR (CDCl$_3$, 300 MHz): 2.487(s, 3H, 5-CH$_3$); 4.174(s, 2H, 3-CH$_2$Br); 7.282-7.322 (m, 2H, HBz); 7.473-7.494 (m, 3H, HBz); ^{13}C-NMR (CDCl$_3$, 300 MHz): 137.469 (C3), 109.887 (C4), 141.603 (C5), 113.198 (C6), 29.026 (C3-CH2Br), 24.08 (C5-CH3), 134.431(C7), 128.592(C8,8-), 130.037 (C9,9-

), 129.77(C10). MS (m/z, (relative abundance, %): 471.1(15.1), 473.1(40.2), 475.1(40.5), 477.1(15.7), 326.2(66.6), 328.2(100), 330.2(683), 246.2(17.1), 248.2(18.2), 168.2(82.4), 167.2(34), 117.1(18.5), 83.7(87.7), 63(30), 51.1(74).

2.3. General procedure for the synthesis of esters (4a-g):-

To a stirred solution of (1.5 mmol) of tribromo-1,2-thiazine (3) in 25mL of dimethyl sulfoxide was added (2 mmol) of dry sodium carboxylate (Formate, acetate, propanoate, N-acetyl glycinate,benzoate,glycolate and salicylate) in one portion, and then the resulting pale-yellow mixture was further magnetically stirred at room temperature. The progress of the reaction was monitored by thin layer chromatography using dichloromethane until the disappearance of starting material. After completion of the reaction, the mixture was poured into 60 mL of ice-cold water, stirred for 20 minutes and the corresponding 1,2-thiazinyl carboxylate (4a-g) was extracted from the obtained milky solution using 30 mL of diethyl ether (twice). The ethereal solution was washed with water, dried over anhydrous sodium sulphate, then the diethyl ether was evaporated under rotary evaporator, and the residue was purified by recrystallization from 95% ethanol to yield

2.3.1 (4,6-dibromo-5-methyl-2-phenyl-1,1-dioxo-1,2-thiazine-3-yl meth)yl formate (4 a):

Pale yellow crystal with yield 85.7%; m.p.: 138-140 °C; FT-IR (KBr): 1176.4s & 1360.7 (SO$_2$), 1719.1s (CO); ^{1}H NMR (CDCl$_3$, 300 MHz): 2.502 (s, 3H, 5-CH$_3$); 4.940 (s, 2H, 3-CH$_2$-O); 7.977 (s, 1H, -CHO); 7.216-7.248 (m, 2H, HBz); 7.437-.458 (m, 3H, HBz); ^{13}C-NMR (CDCl$_3$, 300 MHz): 135.772 (C3), 111.730 (C4), 141.512 (C5), 113.462 (C6), 61.879 (C3-CH$_2$O), 24.18 (C5-CH$_3$), 134.532 (C7), 128.146 (C8,8-), 129.821(C9,9-), 129.602 (C10), 159.419 (C11). MS (m/z, (relative abundance, %): 473.1(14.3),

475.3(30.3), 441.1(16.4), 326.2(76.6), 328.2(100), 330.2(72.3), 264.1(10.6), 266.1(8.9), 246.2(17.1), 248.2(21.2), 168.2(73.4), 167.2(34), 100(86.1), 77.1(96.8), 51.1(86.1).

2.3.2. (4,6-dibromo-5-methyl-2-phenyl-1,1-dioxo-1,2-thiazine-3-yl meth)yl acetate (4 b):

Pale yellow crystal with yield 88.3%, m.p.: 129-131ºC; FT-IR (KBr): 1176.2s & 1363.7 (SO$_2$), 1733.5s (CO); ^{1}H-NMR (CDCl$_3$, 300 MHz): 2.001(s,3H,CO-CH$_3$); 2.486(s, 3H, 5-CH$_3$); 4.852 (s, 2H, 3-CH$_2$-O); 7.207-7.226 (m, 2H, HBz); 7.419-7.439 (m,3H , HBz); ^{13}C-NMR (CDCl$_3$, 300 MHz): 136.542 (C3), 111.069 (C4), 141.607(C5), 112.950 (C6), 62.586 (C3-CH$_2$O), 24.233 (C5-CH$_3$), 134.714 (C7), 128.133 (C8,8-), 129.693 (C9,9-), 129.469 (C10), 169.706 (C11), 20.34 (C12). MS (m/z, (relative abundance, %): 449.2(22.3), 451.2(44.9), 453.2(16.4), 326.2(63.6), 328.2(100), 330.2(61.3), 264.1(50.1), 266.1(46.5), 246.2(25.1), 248.2(26.7),

168.2(50.6), 167.2(24), 104.1(33.8), 77.1(54.2), 51.1(37.2), 43.1(73.1).

2.3.3. (4,6-dibromo-5-methyl-2- phenyl-1,1-dioxo-1,2-thiazine-3-yl meth)yl propanoate (4 c):

Pale yellow crystal with yield 88.6; m.p.: 87-88 ºC; FT-IR (KBr): 1180.0s & 1365.2 (SO$_2$), 1743.9s(CO); ^{1}H- NMR (CDCl$_3$, 300 MHz): 1.108 (t, 3H, OCH$_2$CH$_3$); 2.299(q, 2H, OCH$_2$CH$_3$) ; 2.5 (s, 2H, 3-CH$_2$) ; 7.197-7.259 (m, 2H, HBz); 7.415-.449 (m, 3h , HBz); ^{13}C-NMR (CDCl$_3$, 300 MHz): 136.622(C3), 111.095 (C4), 141.589 (C5) ,112.910 (C6), 62.528 (C3-CH$_2$O), 24.264 (C5-CH$_3$), 134.699 (C7),128.127 (C8,8-), 129.659 (C9,9-),

129.447 (C10), 173.239 (C11), 27.114 (C12) , 9.002 (C13). MS (m/z, (relative abundance, %): 463(18.2), 456(39.5), 467(19.9), 326.2(73.5), 328.2(100), 330.2(72.1), 264.1(60.1), 266.1(58.5), 246(30.3), 248(29.8), 168.2(69.1), 167.2(35.6), 104(29.6), 77.1(76.2), 51.1(85.1).

2.3.4. (4,6-dibromo-5-methyl-2-phenyl-1,1-dioxo-1,2-thiazine-3-yl meth)yl N-acetyl glycinate(4 d):

Pale yellow crystal with yield 80.%, m.p.: 105-106 $^{\circ}$C; FT-IR (KBr): 1182.9s & 1363.9s (SO$_2$), 1760.5s & 1640.5s(CO), 3290.6s (NH); ^{1}H-NMR (CDCl$_3$, 300 MHz): 2.046 (s, 3H, CO-CH$_3$); 2.497 (s, 3H, 5-CH$_3$) ; 4.015 (d, 2H, OCO-CH$_2$-NH); 4.943 (s ,2H, 3-CH$_2$-O); 5.955(s, 1H, NH); 7.195-7.214 (m, 2H, HBz) ; 7.439-7.459 (m, 3H, HBz); ^{13}C-NMR (CDCl$_3$, 300 MHz): 135.732 (C3), 111.936 (C4), 141.434 (C5), 113.711(C6), 63.228 (C3-CH$_2$O), 24.160 (C5-CH$_3$), 134.569 (C7), 127.992 (C8, 8-), 129.783 (C9, 9-), 129.609 (C10), 170.175 (C11), 41.047 (C12), 168.926 (C14), 22.868 (C15). MS (m/z, (relative abundance, %): 506.1(18.5), 508.1(38.3), 510.1(19.1), 326.2(56.6), 328.2(100), 330.2(54.3), 264.1(40.6), 266.1(38.9), 246.2(22.1), 248.2(24.2), 168.2(65.2), 167.2(33.2), 100(86.1), 77.1(66.8),65(18.1) 51.1(86.1), 41(85).

2.3.5. (4,6-dibromo-5-methyl-2-phenyl-1,1-dioxo-1,2-thiazine-3-yl meth)yl benzoate (4 e):

Pale yellow crystal with yield 89.3%; m.p.: 120-121 $^{\circ}$C; FT-IR (KBr): 1181.6s & 1368.4s (SO$_2$), 1728.0s (CO); ^{1}H NMR (CDCl$_3$, 300 MHz): 2.52(s, 3H, 5-CH$_3$); 5.118(s, 2H, 3-CH$_2$O); 7.24-7.271(m, 2H, HBz); 7.383-7.490(m, 3H, HBz); 7.464(t, 2H, H-benzoate); 7.604 (t, 1H, Hbenzoate); 7.991(d, 2H,

Hbenzoate); ^{13}C NMR (CDCl$_3$, 300 MHz): 136.634(C3), 111.349 (C4), 141.608 (C5), 113.238 (C6), 63.081 (C3-CH$_2$O), 24.269 (C5-CH$_3$), 134.70 (C7),128.130 (C8,8-), 129.70 (C9,9-), 129.541(C10),165.369 (C11), 129.793 (C12), 129.077 (C13,13-), 128.512 (C14,14-), 133.435 (C15). MS (m/z, (relative abundance, %): 511(7.1), 513(14.1), 515(8.1), 326.1(16.1), 328.1(32), 330.1(15.6), 246(8.2), 248(9.1), 168.2(18.2), 167.2(8.1), 105(100), 77.1(57.2), 51.1(21).

2.3.6. (4,6-dibromo-5-methyl-2-phenyl-1,1-dioxo-1,2-thiazine-3-yl meth)yl glycolate (4 f):

Pale yellow crystal with yield 77.1%; m.p.: 144-145 $^{\circ}$C; FT-IR (KBr): 1168.9s &, 1346.2s (SO$_2$) 1740.16s (CO) 3514.0s (OH); ^{1}H-NMR (CDCl$_3$, 300 MHz): 2.256(s, 1H, OH); 2.495(s, 3H, 5-CH$_3$); 4.126(s, 2H, CO-CH$_2$-OH); 4.979(s, 2H, 3-CH$_2$-O); 7.196-7.227(m,2H, HBz); 7.435-7.456(m, 3H, HBz); ^{13}C-NMR (CDCl$_3$, 300 MHz): 135.699 (C3), 111.803 (C4), 141.485(C5) ,113.563 (C6), 63.246 (CH$_2$O), 24.173 (C5-CH$_3$), 134.594 (C7), 128.020 (C8,8-), 129.815 (C9,9-), 129.588 (C10), 172.130 (C11), 60.281(C12). MS (m/z, (relative abundance, %): 465.1(13.3), 467.1(27.9), 469.1(14.4), 407.1(8.3), 409(16.1), 411.1(8.2), 326.2(77.6), 328.2(100), 330.2(76.1), 264.1(22.1), 266.1(20.5), 246.2(13.1), 248.2(15.2), 168.2(66.6), 167.2(27.1),104.1(42.7), 86(22), 85(47.2), 77.1(93.2), 65(13.5), 51.1(58.2).

2.3.7. (4,6-dibromo-5-methyl-2-phenyl-1,1-dioxo-1,2-thiazine-3-yl meth)yl salicylate (4 g) :

Pale yellow crystal with yield 73.9%; m.p.: 116-117 $^{\circ}$C; FT-IR (KBr): 1158.3s & 1362.1s

(SO$_2$), 1680.1s (CO), 3126.3w (OH); ^{1}H-NMR (CDCl$_3$, 300 MHz): 2.527 (s, 3H, 3-CH$_3$); 5.144 (s, 2H, 3-CH$_2$O); 6.952 (m, 2H, H salicylate); 7.502 (m, 1H, H-salicylate); 7.769,7.8 (dd,1H, H-salicylate); 7.227-7.284 (m, 2H-, HBz); 7.384-7.434 (m, 3H, HBz); 10.305 (s, 1H, OH); ^{13}C- NMR (CDCl$_3$, 300 MHz): 136.271(C3), 111.732 (C4), 141.540 (C5), 113.587 (C6), 63.148 (C3-CH$_2$O), 24.283 (C5-CH$_3$,134.565 (C7), 128.054(C8,8-), 129.811(C9,9-), 129.625 (C10), 168.795 (C11), 130.037 (C12), 161.684 (C13), 117.674(C14), 135.931(C15), 119.464(C16) ,141.540 (C17). MS (m/z, (relative abundance, %): 527(19.2), 529(38.1), 531(20.3), 326.2(73.5), 328.2(100), 330.2(72.1), 264.1(12.3), 266.1(11.5), 246(24.5), 248(25.1), 168.2(81.1), 167.2(37.6), 121(97.2), 77.1(59.6), 51.1(37.1).

3. RESULTS AND DISCUSSION

The first impartial of this study was to synthesize and spectroscopic study of some new 1,2 thiazine system incorporating various esters groups. The required 3, 5-dimethyl-2-phenyl-1,1-dioxo-1,2-thiazine (2) for this study was readily prepared through a single-step reaction as outlined in Scheme 1. From the reaction of 3,5-dimethyl-2-phenyl-1,1-dioxo-1,2-oxathine (1) and aniline [Tawada et al 1990]. The formed 3,5-dimethyl-2-phenyl-1,1-dioxo- 1,2-thiazine (2) in the presence of potassium carbonate in chloroform at room temperature reacts with bromine to afford 4,6-dibromo-2-phenyl-5-methyl-3-bromomethyl-1,1-dioxo-1,2-thiazine (3) [*Shen and Dryhurst 2001*]. In the present study, 3-bromomethyl 1,2-thiazine (3) easily undergoes nucleophilic substitution reaction in dimethyl sulfoxide at room temperature for giving (4,6-dibromo-5-methyl-2-phenyl-1,1-dioxo-1,2-thiazine-3-yl meth)yl formate (4a) in high yield. Since at room temperature-condition, the reaction was progressed smoothly and products were obtained in very good yields and in high purity, the esterification process of 3-bromomethyl groups of compound (3) was extended for the preparation of (4,6-dibromo-5-methyl-2-phenyl-1,1-dioxo-1,2-thiazine-3-yl meth)yl acetate (4b) propanoate (4c), N-acetyl glycinate (4d) and benzoate (4e) using sodium acetate, propanoate, N-acetyl glycinate and benzoate. To further expand our understanding of esterification-reactions of 1,2-thiazine system, reaction of 4,6-dibromo-2-(substituted phenyl)-5-methyl-3-bromomethyl-1,1-dioxo-1,2-thiazine (3) with sodium glycolate and salicylate in dimethyl sulfoxide at room temperature was carried out to the corresponding (4,6-dibromo-5-methyl-2-phenyl-1,1-dioxo-1,2-thiazine -3-yl meth)yl glycolate (4f)

Scheme (1): preparation of compounds (4a-g)
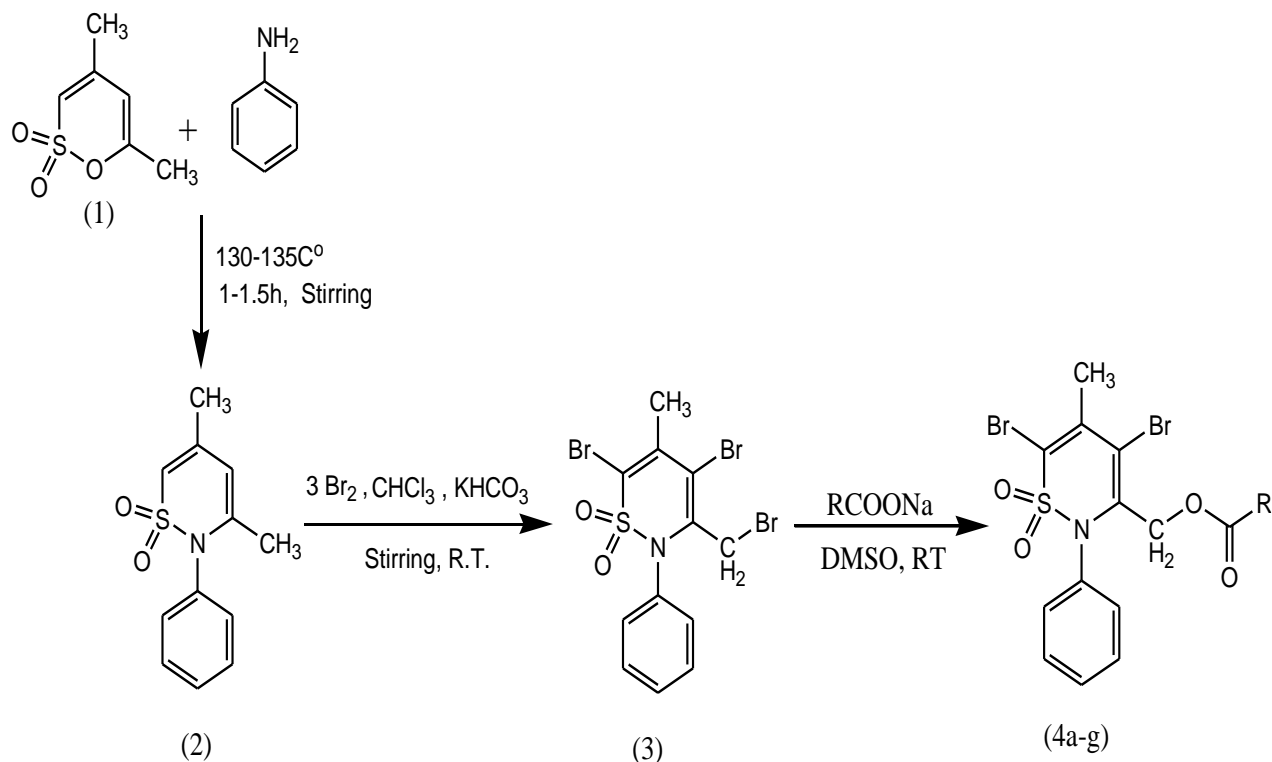
4a R=H,   4b R=CH3,   4c R=CH3CH2,   4d R=CH2NHCOCH3,   4e R=C6H5,   4f R =CH2OH,   4g R= C6H5(2-OH)

salicylate and (4g) in yields lower than those of (4 a-e). Herein, steric effects come into play; the hydroxyl groups of the glycolate and salicylate anions in two modes lowering the product-yield. In the former, the hydroxyl group through its negative inductive effect decreases the nucleophilicity of the glycolate anion, while in the latter; the formed intramolecular hydrogen bond between carbonyl oxygen atom and the hydroxyl group at ortho position decreases the nucleophilic power of the salicylate anion toward the bromo group of the 3-bromomethyl moiety of (3), and this interpretation was in agreement with their infrared and proton NMR data of the hydroxyl groups and also with the reported data [*Hosangadi and Dave 1996*].

M=437.1 (14.3%)

M+2=439.1 (30.3%)

M+4=441.1 (16.4%)

M=77.1 (96.8%)

$\overset{+}{C}_4H_3$

M=51.1 (86.1%)

M=326.2 (76.6%)

M+2=328.2 (100%)

M+4=330.2 (72.3%)

M=264.1 (10.6%)

M+2=266.1 (6.38%)

M=168.2 (73.4%)

M=104 (42.5%)

M=246.2 (17%)

M+2=248.2 (21.2%)

M=167.2 (34%)
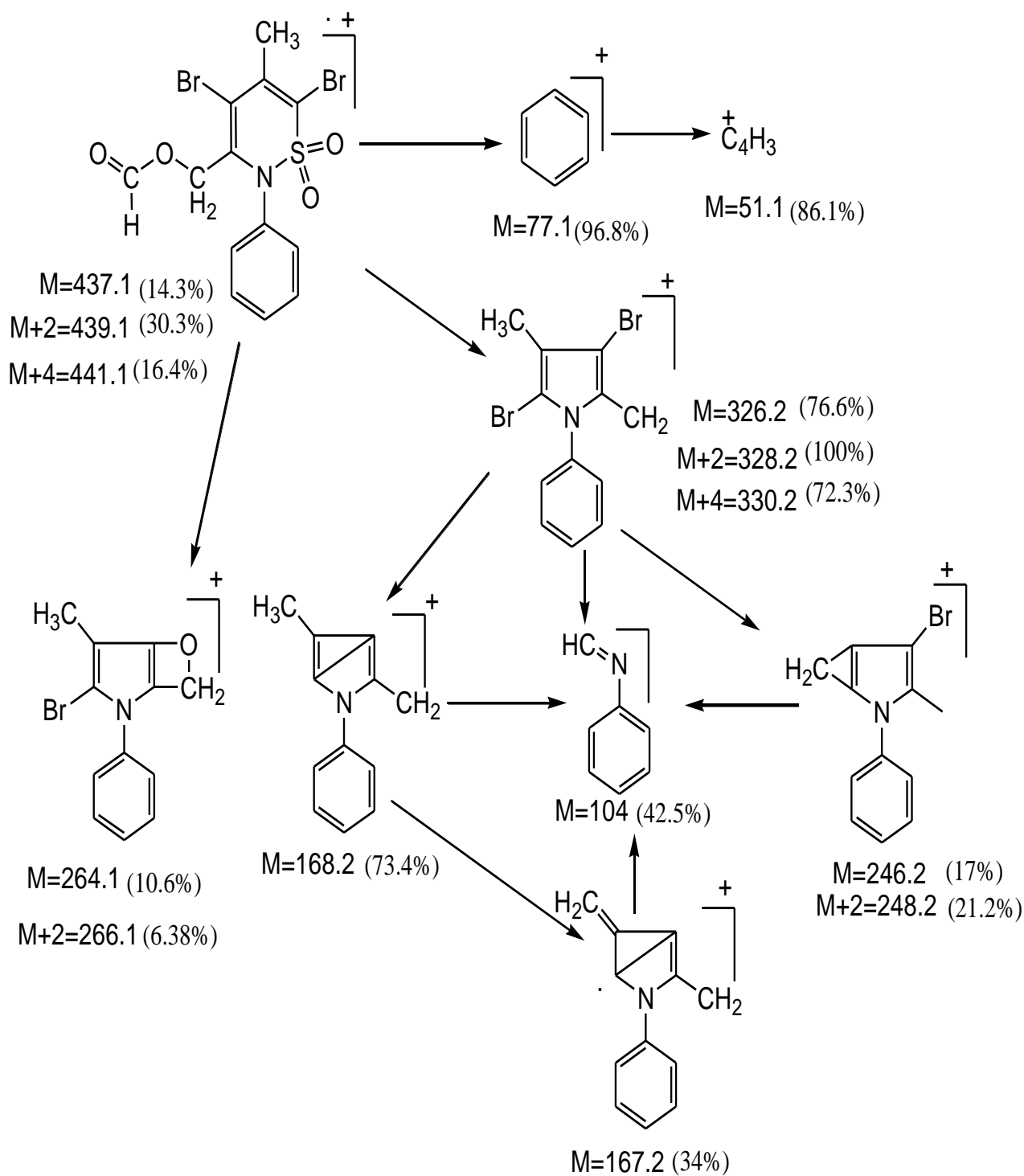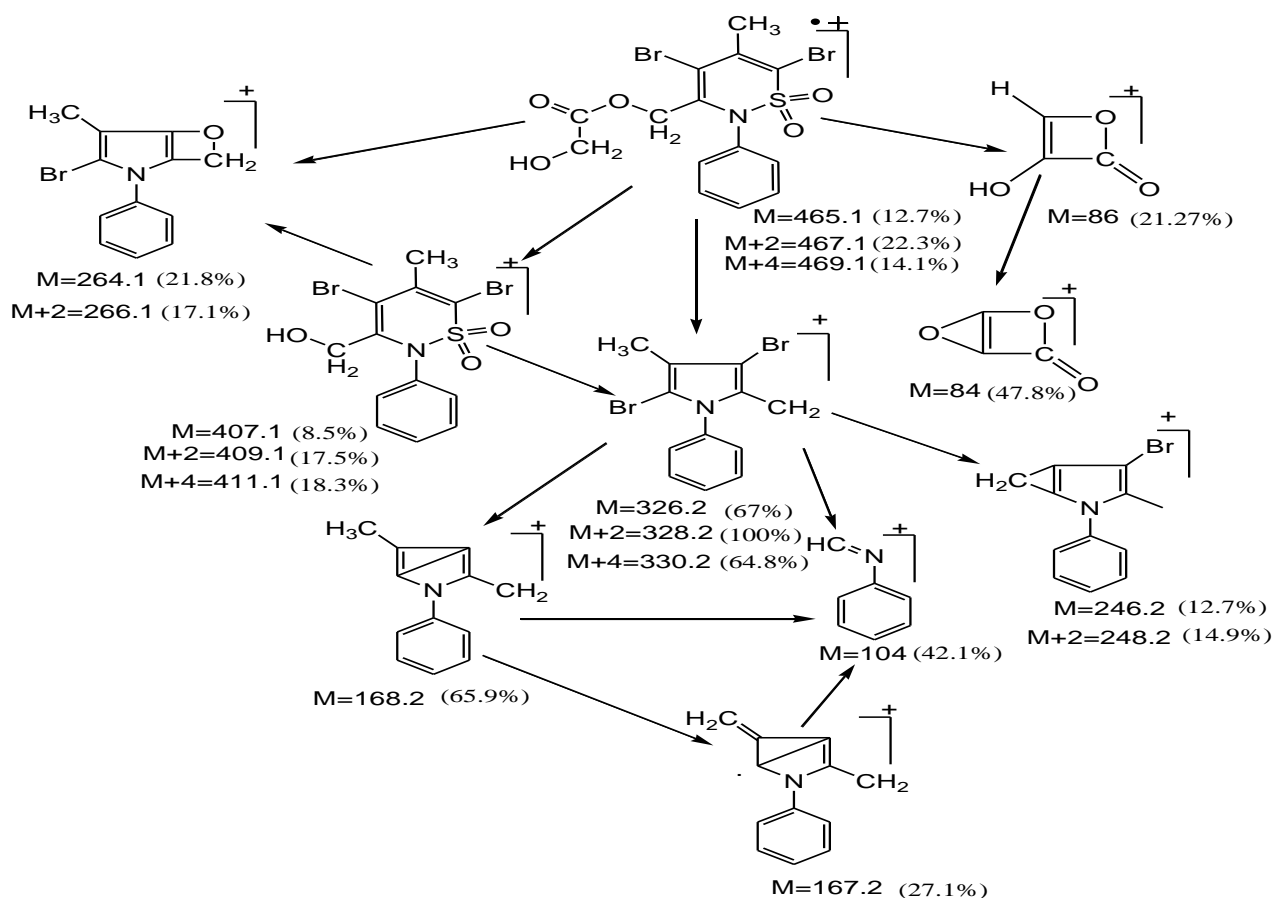
Scheme (2): Mass fragmentation of N-(4,6-dibromo-5-methyl-2-phenyl-1,1-dioxo-1,2-thiazine-3-yl meth) yl formate (4a) and glycolate(4f).

signal at 4.174 ppm due to the protons of the 3-methylene group in (3), on esterification process was shifted to around 5 ppm. For our knowledge the depicted molecular ion peak in the mass spectrum of each ester is in covenant with the molecular weight of the obtained esters (4a-g). In addition to that in the mass spectra of ester 4a the base ion peak, which results from the loss of   sulfur dioxide molecule and carboxylate radical from its molecular ion appears at M/Z = 326.2, and the isotope patterns at 328.2 and 330.2 revealed the presence of the two bromo groups in it. Another two prominent peaks at 246.2 with its M+2 at 248.2 were due to 4-bromo-2-phenyl-

2-azabicyclo   [3.1.0]   hexa-1(5)-3-diene-2-methylene cation and it could be seen in the mass spectra of all ester compounds. The ions at M/Z at = 264.2 and its M+2 at 266.2 due to formation   of   3-bromo-4-methyl-2-phenyl-6-oxa-2-azabicyclo[3.2.0]hepta-1-,3-diene cation and at   168 due to 4-methyl-2-methylene-1-phenyl-2H-pyrrolium cation were shown in the mass spectra of all ester compounds. Herein, we can say that the mass fragmentation of the ester compounds were similar to each other except for showing some different ions which were references to the carboxylate moiety.

4. CONCLUSIONS

In this work a series of new 1,2-thiazine system incorporating various ester groups was prepared through a classical, convenient and practical method. In this method, the products can be separated conveniently from the reaction mixture in high purity and no chromatographic method needed for their isolation. Another notable advantage of this method is that the reaction condition was mild and the products were obtained in very good yields in suitable time. The present approach has the ability to synthesize a variety of 1,2-thiazines bearing various group.
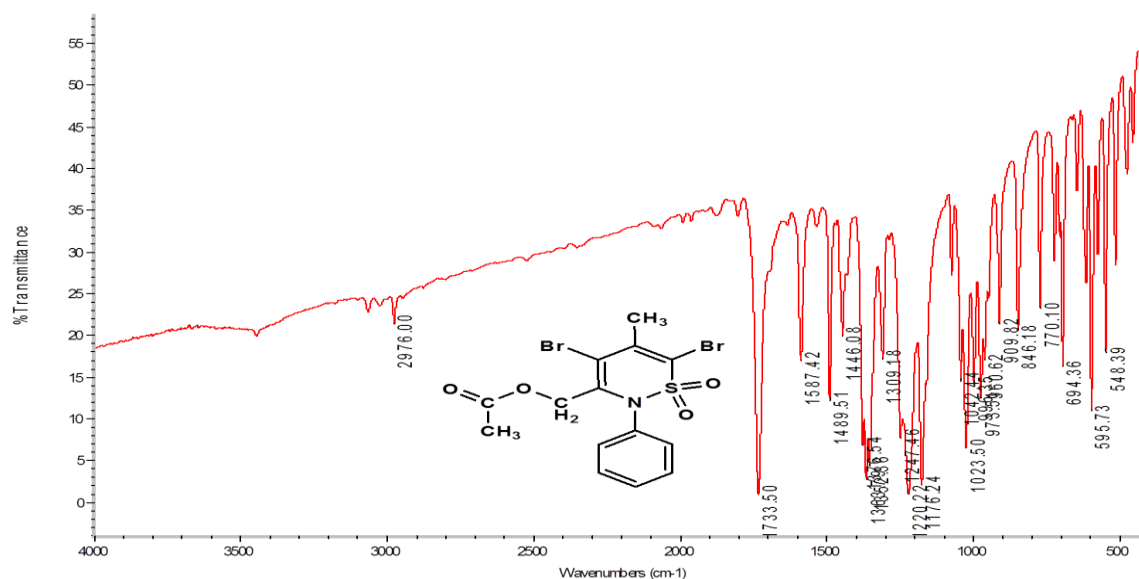
Figure (1): Infrared spectrum of compound (4b)
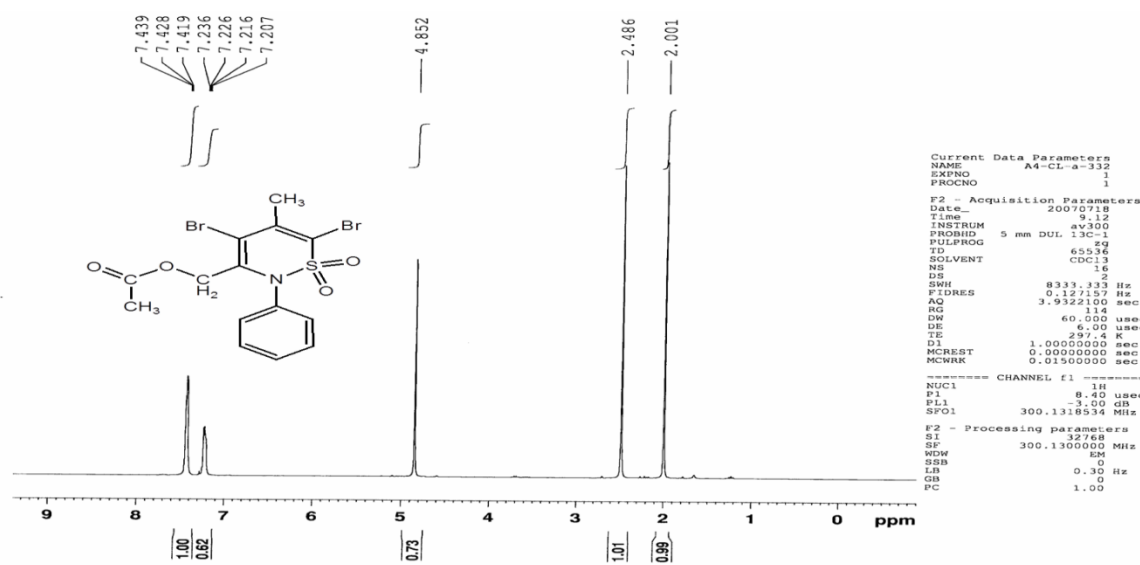
Figur (2): ^{1}H - NMR spectrum of compound (4b)
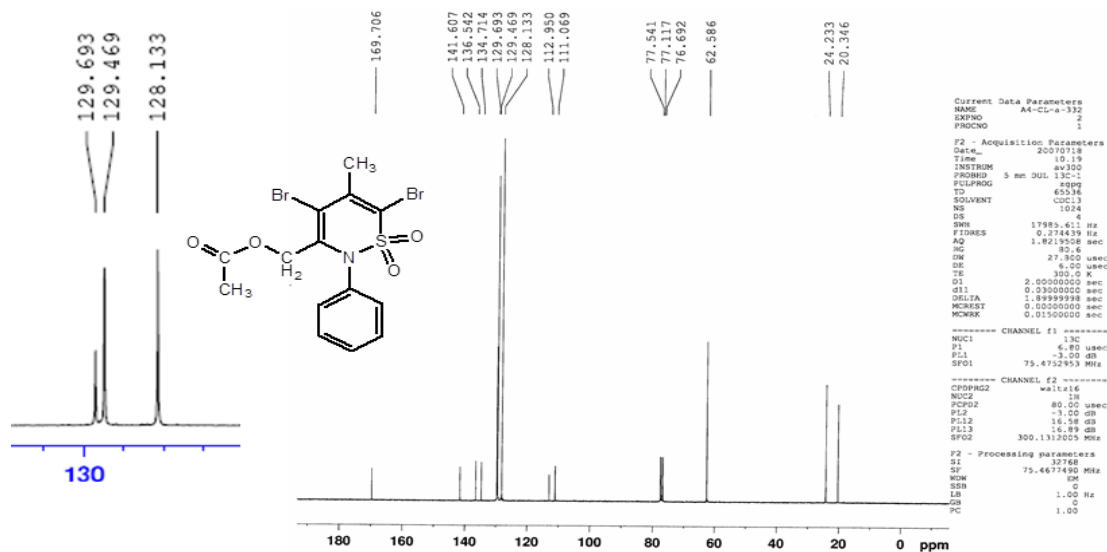
Figur (3): ^{13}C - NMR spectrum of compound (4b)
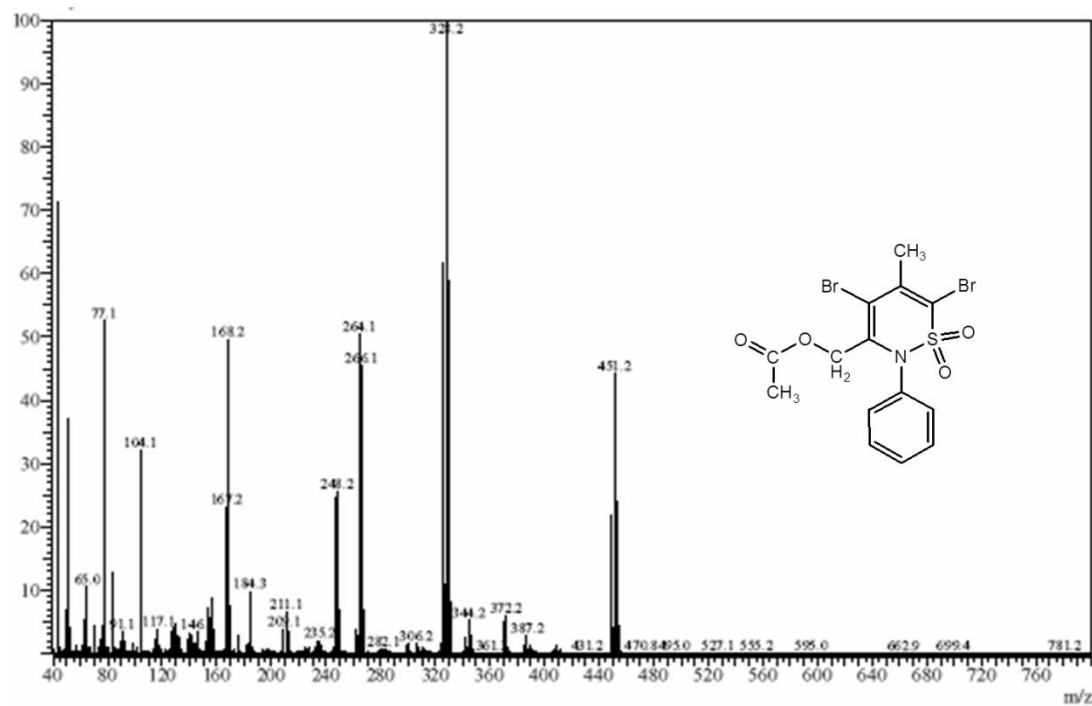
Figure (4) : Mass spectrum of compound (4b)

REFERENCES

Aras, N., H.; Synthesis and preliminary evaluation of the antibacterial activity of some new compounds from nucleophilic acyl substitution and ring opening reactions

of 5(4H)-oxazolones , ZANCO Journal of Pure and Applied Sciences, **2016**; 28 (3), 175-185.

Bartzatt, R.; Malesa, C.; Synthesis, structural analysis and antibacterial activity of a butyl ester derivative of ampicillin, Chemotherapy, **2003**; 49(5), 213-21.

Bartzatt, R.; Cirillo, S. L.; Cirillo, J. D.; Molecular properties and antibacterial activity of the methyl and ethyl ester derivatives of ampicillin, Physiological Chemistry and Physics and Medical NMR, **2004**; 36, 2, 85-94.

Bassem, S.; Amar, M. H.; and Abdu, A.; Anti-inflammatory agents of the carbamoylmethyl ester class: synthesis, characterization, and pharmacological evaluation, Journal of Inflammation Research., **2013**; 6: 35–43.

Boussalah, N., Touzani, R., Souna, F., Himri, I., Bouakka, M., Hakkou, A., Ghalem, S., El Kadiri, S. Hide details, Antifungal activities of amino acid ester functional pyrazolyl compounds against Fusarium oxysporum f.sp. albedinis and Saccharomyces cerevisiae yeast, Journal of Saudi Chemical Society, **2013**, 17, 1, 17-21.

Claudriana, L.; Fabíola, B. F.; Tânia, B. C.; Alkyl esters of gallic acid as anticancer agents: A review, European Journal of Medicinal Chemistry, **2013**; 60, 233-239.

Fanghanel, E.; Radeglia, R.; and Mohammed, H.; Substituent Effects and 13C-NMR Chemical Shifts of para Substituted N-Phenyl-2,4-Dimethyl-buta-1,3-diene-Sultames-1,4; Journal für praktische Chemie, **1983**, 325, 1030.

Fanghanel, E.; Mohammed, H.; Radeglia, R.; and Keita, Y.; Structure Elucidation of Bromination Products of N-Aryl-2, 4-dimethyl-buta-1,3-diene-sultames-1, 4; Journal für praktische Chemie, **1982**, 324, 353.

Hisashi Y.; Kazuko T.; Keiko I.; Yukiko S.; Tsutomu A.; Hajime, K.; Antiviral and Virucidal

Activities of N-Cocoyl-L-Arginine Ethyl Ester, Advances in Virology, **2011**, 6 -12.

Hosangadi, B. D.; and Dave, R. H.; An efficient general method for esterification of aromatic carboxylic acids ; Tetrahedron Lett. **1996**, 37(35), 6375.

Huhtanen, C, N.; Guy, E. J.; Antifungal Properties of Esters of Alkenoic and Alkynoic Acids, journal of food science, **1984**, 49, 1, 281- 285.

Joseph, P. S.; Gregory, S. H., , heterocyclic ester and amide hair growth compositions and uses,2001, US 6,274,617 B1.

Khan, A. A.; Alanazi, A. M.; Jabeen, M.; Chauhan, A.; Abdelhameed, A. S.; Design, Synthesis and In Vitro Anticancer Evaluation of a Stearic Acid-based Ester Conjugate, Anticancer Research, **2013**; 33, 6, 2517-2524.

Mariia. N.; and Iryna, K.; Synthesis and Pharmacological Properties of Novel Esters Based on Monocyclic Terpenes and GABA, Pharmaceuticals (Basel). **2016**; 9(2): 32.

Martin, K.; Jarmila, V.; Antifungal Activity of Salicylanilides and Their Esters with 4-(Trifluoromethyl)benzoic Acid, Molecules, **2012**, 17(8), 9426-9442.

Mounir, A. K.; John, C. L.; Henry J. L.; Synthesis of a new anti-inflammatory steroidal acid ester: Methyl 11β-hydroxy-3,20-dioxo-1,4-pregnadien-21-oate,
Journal of Pharmaceutical Sciences, **1985**, 74, 2, 180–183.

Nothias-Scaglia, L. F.; Pannecouque, C.; Renucci, F.; Delang, L.; Neyts, J.; Roussi; F.; Costa, J.; Leyssen, P; Litaudon, M.; Paolini. J.; Antiviral Activity of Diterpene Esters on Chikungunya Virus and HIV Replication., Journal of Natural Products, **2015, 78 (6), 1277–1283**.

Shen, X. M.; Dryhurst, G.; Influence of glutathione on the oxidationchemistry of 5-S - cysteinyldopamine: potentially neuroprotective reactions of relevance to arkinson's disease. Tetrahedron, **2001**, 57, 2, 393–405.

Shima, H. E. K.; Mohsen, A.; Mohsen, V., Abbas, S.; Ebrahim, A.; and Farzad, K.; Synthesis, Evaluation of Anticancer Activity and QSAR Study of

Heterocyclic Esters of Caffeic Acid, Iranian Journal of Pharmaceutical Research, **2013**; 12, 4, 705–719.

Tawada, H.; Sugiyama, Y.; Ikeda, H.; Yamamoto, Y.; Meguro, K.; Studies on antidiabetic agents. IX. A new aldose reductaseinhibitor, AD-5467, and related 1,4-benzoxazine and 1,4-benzo-thiazine derivatives: synthesis and biological activity, Chemical and Pharmaceutical Bulletin, **1990**; 38, 1238–45.

Vaiyapuri, S.; Shruthi S. D.; In vitro and in silico antidiabetic activity of pyran ester derivative isolated from Tragia cannabina, Asian Pacific Journal of Tropical Biomedicine, **2014**, 4, 1, S455-S459.

Waters, J. A.; Hollingsworth, E. B.; Daly, J. W.; Lewandowski, G.; Creveling C. R.; Anticonvulsant activity of piperidinol and (dialkylamino) alkanol esters., J Medical Chemistry, **1986** ;29(8):1512-6.

Synthesis of some new Betti bases via one-pot three-component reaction of β-naphthol, primary diamine and substituted aromatic aldehydes

Dalia A. Abdul[1], Faiq H.S. Hussain[2]

1-Department of Chemistry, College of Science, University of Sulaimani, Sulaimani-Kurdistan Region, Iraq

2-Ishik Research center, University of Ishik, Erbil-Kurdistan Region, Iraq

A R T I C L E   I N F O

*Corresponding Author:
Dalia A.Abdul
dalia.abdul@univsul.edu.iq

A B S T R A C T

An efficient method is described for the synthesis of   N,N`-bis-[(2-hydroxy-napthalene-1-yl) (substituted phenyl)methyl]2,6-diamino pyridine derivatives by one pot three components reaction of β-naphthol, 2,6-diaminopyridine and substituted aromatic aldehydes in ethanol without any catalyst .Many of the synthesized products have been characterized by melting point ,FTIR,1HNMR,13C NMR and mass spectral data

1. INTRODUCTION

Survey of chemistry of the Betti's bases started at the beginning of the 20th century, when Betti (Betti,1901),informed that condensation of 2-naphthol, benzaldehyde and ammonia provided a good product. Preparation of the substituted Betti's base derivatives via the modified Mannich reaction had subsequently become an important area in synthetic chemistry because of C–C bond formation under mild experimental conditions. In last years   a similar reaction were achieved can by either

using other naphthols (Pirrone,1940) or quinolinols (Phillips,1956) or by replacing ammonia with alkyl amines (Brode & Littman, 1930), (Wang & Ding, 2002), (Cardellicchio *et al*., 1999) and (Szatmari, 2003). In addition, a variety of racemic structures related to the Betti's bases have been synthesized recently by addition of naphthols to the preformed imminium salts(Grumbach *et al*.,1996). In recent years, the effort were done to synthesized the Betti's base derivatives in organic solvents such as EtOH, MeOH, and Et$_2$O at room temperature or thermally under solvent less condition .The literature also reveals that such compounds are gaining interest of chemists who are working in the field of asymmetric synthesis because of utility in preparation of chiral inductors or chiral precursor. Betti's base derivatives have also

2. MATERIAL AND METHODS

2.1 Experimental Notes

Thin Layer Chromatography (TLC) was carried out by using pre coated plate with slic agel plate. IR-Spectra were recorded on FT-IR spectrophotometer, 1000 (USA) Perkin Elmer (USA) as KBr disc. Nuclear Magnetic Resonance (NMR) spectrophotometry ^{1}H-NMR,^{13}C-NMR spectra was recorded on Ultrashield-500 plus instrument(BRUKER, Germany – 600MHz) spectrometers using DMSO &CDCl$_3$ as a solvent. Mass Spectra (MS) instrument used in this work is ISQ Single Quadrupole MS, Germany. Gas chromatography – mass spectroscopy (GC-MS) was recorded on QP 2010 GC instrument (Shimadzu, Japan).Elemental analysis used Euro EA Elemental Analyzer

provided convenient access to many useful synthetic building blocks via the amino and phenolic hydroxy functional groups (Szatmari *et al*., 2004) and (Heydenreich *et al*.,2006). Several more and green procedures for Betti reactions have also been successfully developed (Csutortoki, 2013) and (Kidwai, 2013). A new environmentally benign multicomponent reactions were synthesis (Sun et al, 2012) (Gong,2014).Synthesis of new type of Betti bases via three-component reaction of beta-naphthol, cyclic amines and isatins was reported (Gao & Sun, 2015). The Betti bases afforded a number of chiral bis phosphorylated thioure reported by (Metlushka *et al*, 2017). In the present work we have synthesized bis Betti Bases via traditional and microwave methods.

type Euro EA 3000/Italy. Melting Point were determined using Automate Melting point System Digital Image Processing Technology Stanford Research Systems.7-The Sonication was performed by Elmasonic type E 30H.The Microwave Irradiation was carried out by domestic microwave oven 900 w,2500MHZ.

2.2. Synthesis of N,N`-bis-[(2-hydroxy-napthalene-1-yl) (substituted phenyl) methyl]2,6-diamino pyridine (1a-1k):

Method[A] Traditional method:

A mixture of 2,6-diaminopyridine (0.136g, 1.25mmol) and substituted aromatic aldehydes (2.5mmol) was dissolve

in (5mL) of ethanol after appropriate time (2-30min) the precipitate formed then dissolve it(in 15mL) THF and 2-naphthol (0.2g, 2.5mmol) was added. The mixture was heated under reflux with stirring for an appropriate time(24-120 hrs.), then the solvent was removed at reduced pressure by rotatory evaporator. Completion of reaction was indicated by TLC monitoring using (n-hexane: ethyl acetate) (4:1). The reaction mixture was cooled to ambient temperature and the crude solid residue was recrystallized in ethanol to afford pure crystals.

Method[B] Microwave assisted :

A mixture of 2,6-diaminopyridine (0.136g, 1.25mmol) ,substituted aromatic aldehydes (2.5mmol) and 2-naphthol (0.2g, 2.5mmol) triturated using mortar and pestle .The mixture was transferred to a (50mL) beaker, then placed vertically in the center of domestic microwave oven ,and irradiated between (2-6 min) table (1) at high Power (400-900 W) the products were sonicated in cold ethanol filtered and dried in vacuum desiccator

2.2.1 N,N`-bis-[(2-hydroxy-napthalene-1-yl) (phenyl) methyl]2,6-diamino pyridine(1a):

deep Yellow solid; IR (cm^{-1}) :3392 (-OH), 3200 (-NH), 3058 (Ar-H), 2850 (-CH), 1600 (C=C), 1225 (C-N).^{1}HNMR (600MHz, CDCl$_3$) :δ =5.19 (s, 2H, CHAr), 6.0-7.60 (m, 25H, ArH), 5.0 (s, 2H, ArOH), 4.0 (brs, 2H, NH) ppm. .^{13}CNMR (100MHz, DMSO.d$_6$): δ = (51, 98.3, 115, 118, 122, 125, 126, 128, 128.4, 128.7, 129, 133, 140, 153.7, 160.2) :Anal.calc.for C$_{39}$H$_{31}$O$_2$N$_3$:C,81.67; H, 5.41;

N, 7.32%, found : C, 81.25; H, 5.0; N, 7.10. MS :m /z =573 (M$^+$).

2.2.2 N,N`-bis-[(2-hydroxy-napthalene-1-yl)4-fluoro(phenyl) methyl]2,6-diamino pyridine(1b):

light yellow solid ;IR (cm^{-1}) :3400 (-OH), 3290 (-NH), 3058 (Ar-H), 2912(-CH), 1601 (C=C), 1227 (C-N ^{1}HNMR (600MHz, CDCl3) :δ =5.19 (s, 2H, CHAr), 5.9-7.60 (m, 23H, ArH), 5.0 (s, 2H, ArOH), 4.0 (brs, 2H, NH) ppm. .^{13}CNMR (100MHZ, DMSO.d6) :δ =(40.5, 98.0, 115, 116, 118, 122, 124.6, 125, 127.6, 128, 128.7, 130, 133, 140.3, 153.7, 160.0, 162.0) :Anal.calc.for C$_{39}$H$_{29}$O$_2$N$_3$F$_2$: C, 76.86; H, 4.76; N, 6.89%, found :C, 76.44; H, 4.50; N, 6.45. MS :m/z =609 (M$^+$)

2.2.3 N,N`-bis-[(2-hydroxy-napthalene-1-yl)2-fluoro(phenyl) methyl]2,6-diamino pyridine(1c):

deep Brown solid; IR (cm^{-1}):3421 (-OH), 3200 (-NH), 3070 (Ar-H), 2974(-CH), 1613(C=C), 1227 (C-N).^{1}HNMR (600MHz, CDCl$_3$) :δ =5.19 (s, 2H, CHAr), 5.9-7.60 (m, 23H, ArH), 5.0(s, 2H, ArOH), 4.0 (brs, 2H, NH) ppm. .^{13}CNMR (100MHz, DMSO.d6) :δ=(40.5, 98.0, 115, 116, 118, 122, 124.6, 125, 127.6, 128, 128.7, 130, 133, 140.3, 153.7, 160.0, 162.0): Anal. calc. for C$_{39}$H$_{29}$O$_2$N$_3$F$_2$:C, 76.86; H, 4.76; N, 6.89%, found : C, 76.40; H, 4.23; N, 6.45. MS :m/z =609 (M$^+$)

2.2.4 N,N`-bis-[(2-hydroxy-napthalene-1-yl)2-chloro(phenyl)methyl]2,6-diamino pyridine(1d):

light orange solid ;IR (cm^{-1}):3500 (-OH), 3200 (-NH), 3061 (Ar-H), 2850 (-CH),

1607 (C=C) ,1234 (C-N). ^{1}HNMR (600MHz,CDCl3) :δ =5.19 (s, 2H, CHAr), 5.92-7.60 (m, 23H, ArH), 5.0 (s, 2H, ArOH), 4.0 (brs, 2H, NH) ppm. .^{13}CNMR (100MHZ, DMSO.d6) :δ=(42.0, 98.0, 115, 118, 122, 122.8, 125.9, 125, 127.4, 127.1, 128, 128.7, 129.4, 129.8, 130, 133, 133.5, 140.0, 143 ,153.7, 160.0) :Anal. calc. for $C_{39}H_{29}O_2N_3Cl_2$: C, 72.90; H, 4.55; N, 6.54 %, found :C, 71.72 ;H, 5.92 ;N, 6.43 MS :m/z =652 (M^+).

2.2.5 N,Nˋ-bis-[(2-hydroxy-napthalene-1-yl) 2-hydroxyl (phenyl) methyl] 2,6-diamino pyridine (1e):

light Yellow solid; IR (cm^{-1}) :3500 (-OH), 3200 (-NH), 3042 (Ar-H), 2900(-CH), 1604 (C=C), 1245 (C-N).^{1}HNMR (600MHZ, CDCl3) :δ =5.19 (s, 2H, CHAr), 5.92-7.63 (m, 23H, ArH), 5.0 (s, 2H, ArOH), 4.0 (brs, 2H, NH) ppm.^{13}CNMR (100MHZ, DMSO.d6) :δ=(41.1, 98.3, 115.4, 116.2, 118, 121.6, 122.2, 122.8, 125.9, 127.4, 128.0, 128.7, 129.8, 130.2, 133.5, 140.3, 153.7, 157.2, 160.2) :Anal. calc. for $C_{39}H_{31}O_4N_3$:C, 77.3; H, 5.1; N, 6.9%, found: C, 77.7; H, 4.5; N, 6.389 MS :m/z =605 (M^+).

2.2.6 N,Nˋ-bis-[(2-hydroxy-napthalene-1-yl) 4-hydroxyl (phenyl)methyl] 2,6-diamino pyridine (1f):

Light Brown solid; IR (cm^{-1}) :3500 (-OH), 3200 (-NH), 3019 (Ar-H), 2910 (-CH), 1611 (C=C), 1236(C-N). ^{1}HNMR (600MHz, CDCl3) :δ =5.19 (s, 2H, CHAr), 5.92-7.63 (m, 23H, ArH), 5.0 (s, 2H, ArOH), 4.0 (brs, 2H, NH) ppm.   .^{13}CNMR (100MHz, DMSO.d6) :δ=(51.0, 98.2, 115, 116, 118, 122.2, 122.8, 125.9, 128.0, 128.7, 129.8, 133, 135.5, 140.3, 154.8, 153.7, 160.2)

:Anal.calc. for $C_{39}H_{31}O_4N_3$:C, 77.3 ;H, 5.1;N, 6.9%, found: C, 77.2 ;H, 5.0; N, 6.7 . MS :m/z=605 (M^+).

2.2.7.N,Nˋ-bis-[(2-hydroxy-napthalene-1-yl)4-methoxy(phenyl)methyl]2,6-diaminopyridine (1g):

Light brown solid; IR (cm^{-1}): 3450 (-OH), 3200 (-NH), 3021Ar-H), 2920(-CH), 1602(C=C), 1224(C-N). ^{1}HNMR (600MHz, CDCl3): δ=3.73 (s, 6H, -OCH3), 5.19 (s,2H, CHAr), 5.927.63(m, 23H, ArH), 5.0(s.2H, ArOH), 4.0(brs, 2H, NH)ppm. ^{13}CNMR (100MHz, DMSO. d6) :δ=(51.3, 56.0, 98.2, 115, 116, 118, 122.2, 122.8, 125.9, 128.0, 128.7, 129.4, 133, 135.5, 140.3, 153.7, 159.5, 160.2) : Anal. calc. for $C_{41}H_{35}O_4N_3$: C, 77.72; H, 5.529; N, 6.63%, found: C, 77.52; H, 5.5; N, 6.62. MS: m/z =633 (M^+).

2.1.8.N,Nˋ-bis-[(2-hydroxy-napthalene-1-yl)4-methyl(phenyl)methyl]2,6-diaminopyridine (1h):

Yellow solid ; IR(cm[-1]): 3445 (-OH) ,3200 (-NH), 3064 (Ar-H), 2838 (-CH),   1602 (C=C) ,1240 (C-N). ^{1}HNMR (600MHz ,CDCl3) :δ=2.35 (s ,6H ,-CH3), 5.19(s, 2H, CHAr), 5.92-7.60(m, 23H, ArH), 5.0(s, 2H, ArOH), 4.0(brs, 2H, NH)ppm. ^{13}CNMR (100MHz, DMSO d6): δ= (20.9, 51.3, 98.2, 115.4, 118.2, 122.2, 122.8, 125.9, 128.0, 128.3, 128.7, 129.7, 133, 135, 140.0, 140.3, 154.8, 153.7, 160.2): Anal. calc. for $C_{41}H_{35}O_2N_3$: C, 81.86; H, 5.82; N.6.98% , found: C, 81.80; H, 5.81; N, 6.96. MS: m/z =601 (M^+).

2.2.9.N,Nˋ-bis-[(2-hydroxy-napthalene-1-yl)2,4-hydroxy(phenyl)methyl]2,6-diaminopyridine (1i) :

Brown solid; IR (cm^{-1}): 3500 (-OH), 3200 (-NH), 3010 (Ar-H), 2912 (-CH), 1610 (C=C) , 120 (C-N). ^{1}HNMR (600MHz, CDCl$_3$) :δ =5.19 (s, 2H, CHAr), 5.92-7.60 (m, 21H, ArH), 5.0 (s, 6H, ArOH), 4.0 (brs, 2H, NH) ppm.^{13}CNMR (100MHz, DMSO.d6) :δ =(41.0, 98.3, 103.4108.8, 115, 116, 118, 122.2, 122.8, 125.9, 128.0, 128.7, 129.8, 131.2, 133.4, 140.3, 156.2, 158.6, 153.7, 160.2) :Anal.calc. for C$_{39}$H$_{31}$N$_3$O$_6$:C, 73.46; H, 4.86; N, 6.59 % found :C, 73.44; H, 4.85; N, 6.58. MS :m/z =637 (M$^+$).

2.2.10 N,N`-bis-[(2-hydroxy-napthalene-1-yl)4-nitro(phenyl) methyl]2,6-diamino pyridine(1j):

Orange solid ;IR (cm^{-1}) :3445 (-OH), 3200 (-NH), 3086 (Ar-H), 2912 (-CH), 1595 (C=C), 1229 (C-N). ^{1}HNMR (600MHz, CDCl3) :δ=5.19 (s, 2H, CHAr), 5.92-8.7 (m, 23H, ArH), 5.0 (s, 2H, ArOH), 4.0 (brs, 2H, NH)ppm. ^{13}CNMR (100MHz, DMSO.d6) :δ =(51.0, 98.3, 115, 118, 122.2, 122.8, 124,

125.9, 128.0, 128.7, 129.3, 133.4, 140.3, 145.9, 149.1, 153.7, 160.2) :Anal. calc. for C$_{39}$H$_{29}$O$_6$N$_5$:C, 70.58; H, 4.37; N, 10.55 %, found :C, 70.57; H, 4.35; N, 10.55 .MS: m/z =663 (M$^+$).

2.2.11 N,N`-bis-[(2-hydroxy-napthalene-1-yl)4-dimethylamino(phenyl)methyl]2,6-diaminopyridine(1k):

Orange solid ;IR (cm^{-1}) :3445 (-OH), 3200 (-NH), 3042 (Ar-H), 29881 (-CH), 1604 (C=C) ,1245 (C-N). ^{1}HNMR (600MHz, CDCl$_3$) :δ =(2.89S, 12H, -CH3), 5.19 (s, 2H, CHAr), 5.92-7.63 (m, 23H, ArH), (5.0 (s, 2H, ArOH), 4.0 (brs, 2H, NH) ppm. ^{13}CNMR (100MHz, DMSO.d6) :δ =(43.6, 51.3, 98.2, 113.6, 115.4, 118.2, 122.2, 122.8, 125.9, 128.0, 128.7, 129.3, 132, 133.5, 140.3, 142.0, 153.7, 160.2) :Anal.calc.for C$_{43}$H$_{41}$N$_5$O$_2$:C, 78.27; H, 6.26; N, 10, 61%, found :C, 78.51; H, 5.92 ;N, 10.55 .MS :m/z =657(M$^+$).

Scheme.1 Synthesis of Bis Betti bases (1a-1k)
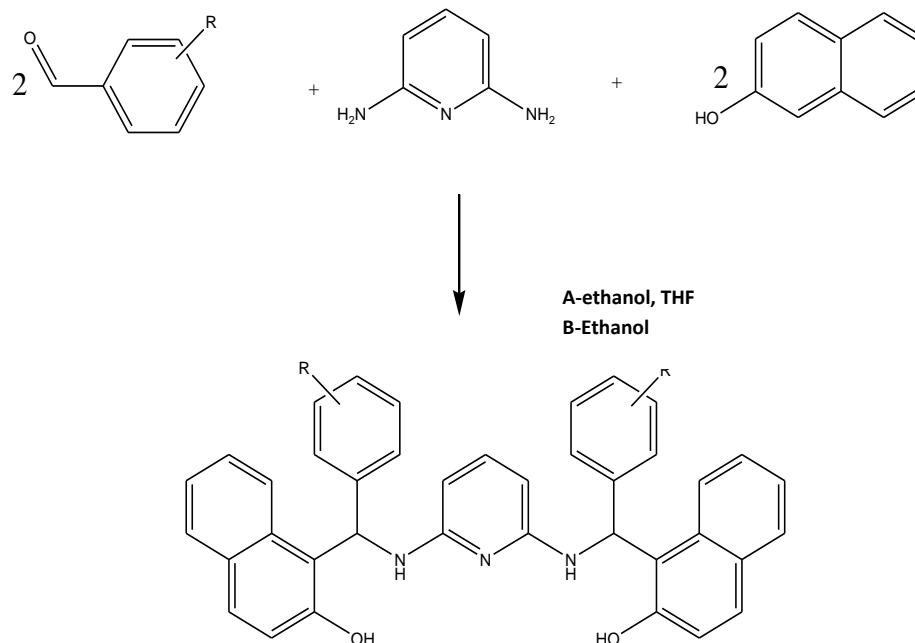
Compd.	R	Molecular formula	Rf	M.P.	Method[A]		Method[B]	
					Time/hr.	%yield	Time/min	%yield
1a	H	$C_{39}H_{31}O_2N_3$	0.5	277-276	24	71	4	42
1b	4-F	$C_{39}H_{29}O_2N_3F_2$	0.2	178-180	96	28	-----------	----------
1c	2-F	$C_{39}H_{29}O_2N_3F_2$	0.4	229-231	44	42	2	28.5
1d	2-Cl	$C_{39}H_{39}O_2N_3Cl_2$	0.87	215-217	44	87	2	25
1e	2-OH	$C_{39}H_{31}O_4N_3$	0.6	223-225	44	98	4	28

Table.1 some physical property of Synthesized Bis Betti bases (1a-1k)

1f	4-OH	$C_{39}H_{31}O_4N_3$	0.44	180-182	120	1.42	6	1.4
1g	4-OCH$_3$	$C_{41}H_{35}O_4N_3$	0.93	198-200	72	63.29	2	28.5
1h	4-CH$_3$	$C_{41}H_{35}O_2N_3$	0.5	184-186	72	71	2	71
1i	2,4-OH	$C_{39}H_{31}N_3O_6$	0.8	180-182	72	63	2	1.2
1j	4-NO$_2$	$C_{39}H_{29}O_6N_5$	0.55	256-258	48	36	2	12
1k	4-N(CH$_3$)$_2$	$C_{43}H_{39}N_5O_2$	0.33	231-233	72	25	----------	----------

3. RESULTS DISCCUSION

Reactions between 2-naphthol, aromatic aldehydes and 2,6-diaminopyridine were resulted in the synthesis of N,N`-bis-[(2-hydroxy-napthalene-1-yl)(substituted phenyl) methyl]2,6-diamino pyridine(1a-1k): (Scheme 1). These reactions were studied under two conditions, as follows: A) Reflux in ethanol for(24- 120)hr.at(80)^{0}C: B)Solvent-free microwave at 400- 900 W for 2-6 minutes in absence of any catalyst; All final compounds reported in this paper are new and not found in the chemical literature and were completely characterized by spectroscopic means. The popularity of employing microwave energy in organic synthesis has tremendously increased in past decade owing to the simplicity, rapidity, high turnover and green nature of the reactions. As evident from data presented in Table 1, we were able to obtain Bis Betti bases 1a-1k in absence of any catalyst using neat conditions under reflux reactions in ethanol benefitted. The comparison of isolated yields, reaction time and material requirements of the two conditions employed showed microwave-assisted solvent-free reactions as the most efficient synthetic method in terms of energy and time consumption but low amount of product compared with other method. The products obtained through the reflux reaction protocol had the inherent advantage of digestion of insoluble product precipitates and therefore the purity of the obtained product were consistently better as evidenced by the sharper and higher melting point as compared to same products obtained by employing other conditions. The structures of all the synthesized compounds were confirmed by elemental analysis and from spectral data (MASS,^{1}HNMR,^{13}CNMR spectra).

4. CONCLUSION

Eleven Bis Betti bases of 2-naphthol were successfully synthesized and purified. Although reflux conditions provided products with higher purity, the use of microwave-assisted conditions was shown to be the most efficient method of synthesizing compounds of this type in terms of atom economy, energy consumption and time required.

Acknowledgement

REFERENCES

BETTI M.(1901), Condensation between 2-naphthol, aldehydes and amines, *J. Chem. Soc*., 80 (1), 81–82.

BRODE W. R. & LITTMAN J. B. (1930), Condensations of secondary amines with aldehydes and naphthols, *J.Amer. Chem. Soc.,* 52,1655–1659.

CARDELLICCHIO C.& CICCARELLA G. (1999),   Naso F., Perna F.and Tortorella P., Use of readily available   chiral compounds related to the Betti base in the enantio selective addition of diethylzinc to aryl aldehydes, *Tetrahedron*, 55, 14685–14692.

CSUTORTOKI R., I. SZATMA´ ri, & F. Fu¨ lo¨ p, (2013), Syntheses of amidocarbamido and carbamato alkylnaphthols, *Curr. Org. Synth.* 10 , 564 –583.

DINDULKAR S.D., V.G. PURANIK & JEONG Y.T., (2012), supported copper triflate as an efficient catalytic system for the synthesis of highly functionalized 2-naphthol Mannich bases under solvent free condition, *Tetrahedron Lett.* 53, 4376–4380.

GRUMBACH H. J., AREND M. & RISCH N. (1996), Aminoalkylation of electron-rich aromatic compounds using preformed iminium salts   derived   from   aldehydes   other   than formaldehyde, *Synth*.,883–887.

GONG H., SUN J. & YAN C.G. (2014), Synthesis of triphenyl phosphanylidene Spiro [cyclopent [2]ene-1,30-indolines] with three-component reaction of triphenyl phosphine, dialkyl acetylene di carboxylates and 3-phenacylideneoxindoles, *Synthesis,* 489–492

GAO H., SUN J. & Yan C.G. (2015), Synthesis of new type of Betti bases via three-component   reaction of beta-naphthol, cyclic amines and isatins, *Chinese Chemical Letters* 26,353–356

HEYDENREICH M., KOCH A., KLOD S., SZATMARI I.,FULOP F.& KLEINPETER. E. (2006) , Synthesis and conformational analysis of napht[10,20:5,6][1,3]oxazino[3,2-c][1,3]benzoxazine   and   napht [10,20:5,6] [1,3]oxazino [3,4-c][1,3] benzoxazine derivatives, *Tetrahedron*, 62, 11081–11089.

KUMAR A., A. SAXENA, M. DEWAN A. & MOZUMDAR S. (2011), Recyclable nano particulate   copper   mediated   synthesis   of naphthoxazinones in PEG-400: a green approach, *Tetrahedron Lett*. 52, 4835–4839.

KARMAKAR B. & BANERJI J. 2011, A competent pot and atom-efficient synthesis of Betti bases over nano crystalline MgO involving a modified Mannich type reaction, *Tetrahedron Lett.* 52, 4957–4960.

KUMAR A., GUPTA M.K. & KUMAR M.(2010), Non-ionic surfactant catalyzed synthesis of Betti base in water, *Tetrahedron Lett*. 51,1582–1584.

KIDWAI M. & CHAUHAN R. (2013), Catalyst-free Synthesis of Betti bases in a Mannich-type reaction, *Asian J. Org. Chem*. 2, 395–398.

Metlushka K., Sadkova D., Nikitina K., Lodochnikova O. & Kataeva O. (2017) Betti base in the synthesis of chiral bisphosphorylated thioureas, Ruusian journal of chemistry 87, Issue 9, PP. 1893–1902

PIRRONE F. (1940), Hydroxyquinolines Amino derivatives of 7-benzyl-8-hydroxyquinoline.7-[a-(pnitroanilino) benzyl]-8-hydroxyquinoline, Gazzetta *Chimica Italiana,* 70, 520–527.

PHILLIPS J. P. & BARRALL E. M. (1956), Betti reactions of some phenols, *J. Org. Chem.,* 21, 692–694.

PHILLIPS J. P. (1956), The reactions of 8-quinolinol, *Chem. Rev*., 56, 271–297.

SZATMARI I., TAMAS A., MARTINEK L. & FULOP F. (2003), Substituent effects in the ring-chain tautomerism of 1,3-diaryl-2,3-dihydro-1H-naphth[1,2-e] [1,3]oxazines, *Tetrahedron,* 259, 2877–2884.

SZATMARI I., HETENY A. & LAZAR L. and FULOP F. (2004), Transformation reactions of the Betti base analog aminonaphthols, *J. Heterocycl. Chem*., 41, 367–373.

SZATMA I.´ ri, F. & Fu¨ lo¨ p, 2013, Syntheses, transformations and applications of aminonaphthol derivatives prepared via modified Mannich reactions, *Tetrahedron* 69 ,1255-1278

SHAFIEE M., Khosropour A.R., Mohammadpoor-Baltork I. & et al. (2012), An efficient, expeditious, and diastereo selective one-pot pseudo-five-component reaction for the synthesis of new bis-Betti bases under catalyst-free conditions, *Tetrahedron Lett*. 53,. 3086–3090.

SUN J., SUN Y.,GONG H., XIE Y.J, &Yan C.G. (2012), Facile synthesis of dis pirooxindole-fused heterocycles via domino 1,4-dipolar addition and Diels–Alder reaction of in situ generated Huisgen 1,4-dipoles, *Org. Lett.* 14 , 5172–5175.

SUN J., SUN Y., GAO H. & YAN C.G. (2012), Synthesis of Spiro [indoline-3, 20-quinoline] derivatives through a four-component reaction, *Eur. J. Org. Chem.,* 1976–1983.

WANG Y., Li X. & DING K. (2002), Synthesis of a new type of chiral amino phosphine ligands for asymmetric catalysis, *Tetrahedron Asymm*., 13, 1291–1297.
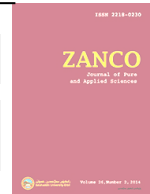
Size and Shape effects of testing specimens on the compressive Strength of SCC

Dillshad K. H. Amen[1], Mohammad A. Ihsan [1], Sinan A. yaseen [1],

1- Civil Department , College of Engineering, Salahaddin University, Erbil, Kurdistan Region, Iraq.

ARTICLE INFO

ABSTRACT

To control the quality of concrete during concreting works, there are various moulds that are used for casting concrete samples according to different standards at different countries. And these differences in the shapes and sizes of concrete samples can cause variations in the results of measured compressive strength. Self-compacting concrete (SCC) have a structural strength and high flowability. This material used in modern concrete technology and extensively in the construction applications of high-rise buildings and long-span concrete structures.This research concentrated on the effect of specimen sizes and shapes on compressive strength of High strength SCC, Specimens were normally cured in the Lab. and tested at age of 28 days. Results were plotted, and indicated that for all testing specimens, there was a significant Influence of size and shape of the specimens on the measured compressive strength. Common sizes that have used for testing compressive strength of concrete were investigated; (100 X100 X100), (150X150X150) mm for cubes and (100 X 200), (150 X300) for cylinders. To determine the best conversion factors, linear relationship added as a trend line between compressive strength measured based on testing cylinders to that measured based on testing cubes, on the other hand relationships was conducted to relate compressive strength tested on cubes and cylinders of different sizes.

1. INTRODUCTION

To control the quality of concrete, there are lots of experiments, each one designated to specify different properties of concrete. Among these experiments, compressive strength is the most important and useful property of concrete. There are many factors that effect on the compressive strength test results, such as environmental condition, loading rate and size and shape of the testing specimens.

The cylinder specimen of concrete (150 diameters and 300 heights) is a standard specimen to test the compressive strength in United States (ASTM C39-2003). While in Britain and Europe, the standard specimen for testing the compressive strength is a cube specimen of concrete by size 150 X 150 X150 mm (BS EN 12390-3,2009, A.M. Neville, J.J. Brooks,2010) The cubes are smaller compared with the cylinder specimen of concrete, and the advantages of cylinders do not depend on the quality and condition of the moulds and that their density can be more readily and accurately established by weighing and measuring(Day, K.W, 2006). The main difference between cylinder and cube specimens is that the cylinder specimens need capping before loading because the top surface of the cylinder finished by the trowel causes no

plane for testing. Two methods are used to obtain the plane surface of the cylinder. (i) Capping method: using sulphur mortar, high strength gypsum plaster and cement paste in order to have plain loading surfaces, the thickness of the capping should be 1.5–3 mm and have the same strength of the concrete. (ii) Grinding method: is satisfactory but expensive

Cubes do not require capping as they are turned over on their sides, when being loaded. The height / diameter ratio equal to 2, the compressive strength of cylinder specimens with varying diameter, the larger the diameter, the lower will be the strength (Day, K.W, 2013, A.M. Neville, J.J. Brooks, 2010, Jin.-keum. Kim, Y. Seong-Tae,2002). The cylinders are cast and tested in the same position, but the cubes are cast in one direction and tested at right angles to the position cast and thus no need of capping or grinding. In actual structures in the field, the casting and loading are similar to those of the cylinder and not like the cube (Neville A.M, 2012). The comparison between the compressive strength of cube and compressive strength of cylinder, a factor of 0.8 to the cube strength is often applied for normal strength concrete (E.I. Al-Sahawneh 2013). Fig. 1 shows the influence of the height to diameter ratio on the compressive strength of concrete. If a cylinder with an aspect ratio h/d = 1, then it will be able to resist higher loads than a cylinder with an aspect ratio of 2 (E.I. Al-Sahawneh, 2013, A.M. Neville, J.J. Brooks, 2010, Jin.-keum. Kim, Y. Seong-Tae,2002). The usual fracture of cylinder specimens is columnar and there are other types such as cone, cone and split, cone and shear and shear (ASTM C39-2003). And typical failure modes of cubes are non-explosive, semi-explosive and explosive (BS EN 12390-3,2009). It's found that the restraining effect of the platens of the testing machine extends over the entire height of a cube but leaves unaffected a part of a test cylinder. It is, therefore, to be expected that the strengths of cubes and cylinders made from the same concrete differ from one another (Neville A.M, 2000).

Because European Standard (ENV 206:1990) recognizes the use of both cylinders and cubes it includes a table of equivalence of strengths of the two types of compression specimens up to 50Mpa (measured on cylinders). The values of the cylinder/cube strength ratio are all around (0.8). These tables should be used for purposes of conversion of a measured strength of one type of specimen to the strength of the type. For any one construction project, a single type of compressive strength test specimen should be used.

It is difficult to say which type of specimen, cylinder or cube, is better but even in countries where cubes are the standard specimen, there seems to be a tendency, at least for research purposes, to use cylinders rather than cubes, and this has been recommended by RILEM -an international organization of testing laboratories. Cylinders are believed to give a greater uniformity of results for nominally similar specimens because their failure is less affected by the end restraint of the specimen, their strength is less influenced by the properties of the coarse aggregate used in the mix, and the stress distribution on horizontal planes in a cylinder is more uniform than on a specimen of square cross section (Neville A.M, 2000, Al-Hayderi H.S, 2003, Carino N.J., Guthrie W.F. and Lagergren E.S, 1994).

It may be recalled that cylinders are cast and tested in the same position, whereas in a cube the line of action of the loads at right angles to the axis of the cube as-cast. In a structural compression members, the situation is similar to that existing in a test cylinder, and

it has been suggested that, for this reason, tests on cylinders are more realistic, the relation between the directions as-cast and as-tested has, however, been shown not to affect appreciably the strength of cubes made with unsegregated and homogenous concrete (Aitcin P.C. 1998). The size of test specimens for strength testing is prescribed in the relevant standards, but occasionally more than one size is permitted. Moreover, from time to time arguments in favor of use smaller specimens are advanced. These point out their advantages, smaller specimens are easier to handle and are less likely to be accidentally damaged, the moulds are cheaper, a lower capacity testing machine is needed, and less concrete is used, which in the laboratory means less storage and curing space, and also smaller quantity of aggregate to be processed(Aitcin P.C, 1994).

This paper was conducted to study the size and shape effect on the high strength SCC. The shapes used were the cubes and cylinders. The size of cubes were 150 X150 X150 mm and 100 X100X100m against the size of cylinders which were 150 X 300 mm and 100 X 200 mm. These sizes were chosen because it represented the sizes that are most commonly used locally and universally in concrete construction.
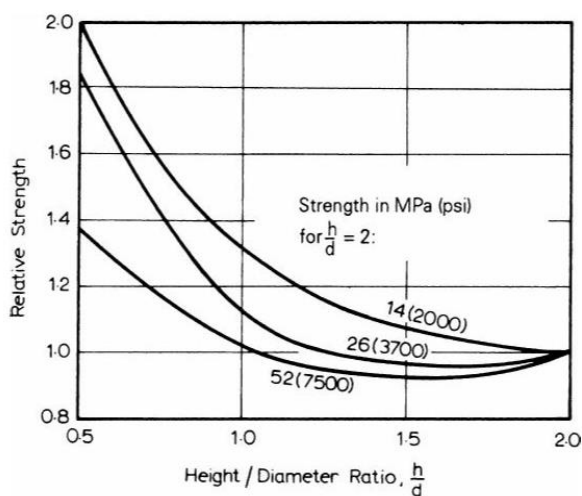
Figure 1. Influence of the height/diameter ratio on the apparent strength of a cylinder for
Different strength level [5].

1.1 Research significance

The use of SCC is spreading worldwide because of its very attractive properties in the fresh state as well as after hardening. Three mixes of high strength SCC were considered starting approximately from 60 to greater than 100 MPa . It must be remembered that the same concrete will not give the same compressive strength when tested as cubes and cylinders. The compressive strength measured on cubes is always higher than that obtained on cylinders. The importance of this investigation is to determine the conversion factors for compressive strength tested by specimens having different shapes and size. Specifically in Kurdistan region, different design methods have been followed for the design of concrete structures. This consequently needs more accurate conversion factors among cubes and cylinders to satisfy strength of concrete for the quality control. From the literature it is shown that there are several previous works and standards on this topic. No standard or research works have been done to determine these conversion factors in specific for self-compacting concrete.

2. MATERIALS AND METHODS

2.1. Materials

The following Materials are used for the preparation of self-compacting concrete specimens

Cement: - Ordinary Portland cement of 42.5 grade , manufactured by Mass cement factory-Iraq, and its chemical composition confirmed the requirements of ASTM type I grade having a specific gravity of 3.15.

Silica Fume: Type SikaFume-HR was used to increase the stability and flowability of SCC mixtures with replacement rate approximately 9% by weight of total cementitious material. Size of particles extremely was 0.1 μ and specific gravity of 2.24.

Fine Aggregate: Natural river sand from Erbil city quarries, with 95 % passing sieve of 5 mm was used. Percentage passing conformed the requirements of ASTM C-33 ,with the apparent specific gravity 2.67 and fineness modulus of 2.85.

Coarse Aggregate: Natural river gravel, un-crashed type, with a maximum size of 12.5 mm was used and their gradation in accordance to ASTM C-33. Specific of gravity was (2.71).

Filler: - Limestone Powder obtained by grinding limestone rocks , particles passing sieve 150 μ were used as inert filler to enhance the particle size distribution of Portland cement.

Admixture: A polycarboxylates based polymer superplasticizer type Sika Visco Crete-PC 15 having a specific gravity of 1.09 used in all the mixtures to obtain the required flowability.

Water: - Tap water was used for mixing and curing.

Table-1 Quantities of materials selected for 1 m³ of SCC mixtures.

Mix. No.	C	A_c	A_f	SF	P	SP %	W_f
SCC-1	384	859	910	3	5	1.33	**157**
SCC-2	437	794	893	4	6	2.13	**164**
SCC-3	494	926	741	4	7	2.13	**143**

2.2. Mix design

The procedure adopted by (ACI committee 237-2007) was followed to select three mixtures of SCC with different powder contents; SCC-I, SCC-2- and SCC-3. Their w/cm ratios were 0.265, 0.345, and 0.375, respectively. Cementitious material contents ranged from 422 kg/m3to 543 kg/m3. Several trial mixes were conducted to obtain the proper mixture proportions. The quantities of

materials selected for 1 cubic meter are shown in Table-1.

2.3. Laboratory Tests

The following tests were conducted on fresh SCC mixtures: the slump flow and T50, according to ASTM C 1611, V funnel test, and L-Box test according to BS EN 12350- 2010. Test results indicated that the selected mixtures of SCC had a good filling and passing abilities. Rheological properties of fresh SCC are shown in table-2. SCC specimens were cast without any compaction. Fresh concrete samples moulded into cubes and cylinders with two different sizes which are most commonly used in concrete works. Cubes of size 150 mm and 100 mm and cylinders of size (150 X 300) and (100 X 200) mm were produced. The specimens were de-moulded after one day of casting and immersed in water until testing age was 28 days.

In this research, as concrete specimens were chosen from different sizes and shapes, for executing compressive strength test, different standards were followed. For measurement of

compressive strength of cubes, BS EN 12390-3:2009 was followed. Compressive strength test of cylindrical specimens were carried out according to ASTM C39/C39M-2011. Testing cylinders in compressive strength has an additional stage of capping.

Table-2 rheological properties of SCC mixtures.

Mix No.	Slump Flow (mm)	T_{500} (Sec)	V-Funnel time (Sec)	L-Box ratio H2/H1
SCC-1	645	4.45	9.65	0.88
SCC-2	675	3.12	8.4	0.91
SCC-3	565	5.85	12.32	0.8

3. RESULTS AND DISCUSSION

Totally three different factors were investigated to find out their influence on concrete compressive strength test results. The factors are two different shapes of moulds, two different size of moulds and three different concrete mix proportions. The employed moulds were 2 different cubes (100 and 150 mm) and two different cylinders (100×200 mm and150×300 mm). Twelve specimens of concrete were cast for each case of testing and analyses. Totally 144 concrete specimens with different sizes and shapes were prepared and tested

3.1. Effect of Size

The compressive strength test results for different size cubes and different size cylinders are plotted as shown in figure-3. The best fit linear equations without intercept (started from zero) are added as a trend lines for the current results. Equations that relate compressive strength of concrete cubes of size 150 mm to cubes of size 100 mm are presented in figure 3-a. and equations that relate compressive strength of cylinders of size (150 X 300) mm to cylinders of size (100 X 200) mm are presented in figure 3-b, for three mixture proportions. It can be seen that strength of cubes or cylinders of smaller sizes were higher than compressive strength of bigger sizes of the corresponding shape and for the same mixture proportion. Moreover the conversion factor depended upon the strength grade of concrete, which is represented by type of the mix. The slope of the trended lines represents the average value of the ratio of compressive strength measured on big specimens to that strength measured on small specimens. Therefore the slope is always less than 1. The value of slopes determined from the plots are listed in Table-3

Table-3 correction factors taking the effect of size of specimens

Mixes	for cubes $\dfrac{f_{cub(150)}}{f_{cub(100)}}$	for cylinders $\dfrac{f_{c(150X300)}}{f_{c(100X200)}}$
SCC-1	0.88	0.86
SCC-2	0.91	0.89
SCC-3	0.92	0.91

3.2 Effect of shapes

The compressive strength test results for different shape of moulds cubes and cylinders are plotted as shown in figure-4. The best fit linear equations without intercept (started from zero) are added as a trend lines for the current results. Equations relate compressive strength of concrete measured on cubes to that measured on cylinders for three mixture proportions. It can be seen that strength of cylinders were lower than strength of cubes of the same corresponding size and for the same mixture proportion. Moreover the conversion factor also depended upon the strength grade of concrete, which is represented by type of the mix. The slope of the trended lines represents the average value of the ratio of compressive strength measured on cylindrical specimens to that strength measured on cubes. Therefore the slope is always less than 1 and called as conversion factors, thus to convert from cubes to cylinders , the following values as listed in table-4 were determined to be multiplied by strength on cubes.

Table-4 correction factors taking the effect of shape of specimens

Mixes	for small specimens $\dfrac{f_{cyl(100 \times 200)}}{f_{cub(100)}}$	for big specimens $\dfrac{f_{cyl(150 \times 300)mm}}{f_{cub(150)mm}}$
SCC-1	0.83	0.81
SCC-2	0.89	0.87
SCC-3	0.91	0.90

3.3. Discussion

It has been reported [5] that within the range of sizes of specimens normally used, the effect of size on strength is not large, but it is significant and should not be ignored in work of high accuracy or in research. Analysis of numerous test data applied for normal type concrete has suggested a general relation to determine conversion factor as a function to the shape and size of the specimen in terms of ($\frac{V}{hd} + hd$), where V = volume of specimen, h = its height, and d = its least lateral dimension. Conversion factor is defined as the ratio of strength of concrete cylinder f_c of any size to the strength of cubes f_{cub} of 150 mm size. The relation has been confirmed also for high strength concrete.

$$\varphi = \frac{f_c}{f_{cub(152)}} = 0.56 * \frac{0.697}{\left(\frac{V}{152\,hd} + \frac{h}{d}\right)}$$

To make the comparison between the equation suggested and the analysis of current results, it can be obtained that conversion factor suggested by the equation equal to 0.84 to convert from cylinders of size (100 X 200) mm to cube of size 150 mm, and equal to 0.81 to convert from cylinder of size (150X300) mm to cube of size 150 mm.

Analysis of current results proposes the following conversion factors:

1. From cylinder (150X300) to cube of size 150 mm, for SCC and high strength SCC.

when the cylinder strength was 80MPa. It has been reported that there is no simple relation between the strength of the specimens of the two shapes. The ratio of the strength of the cylinder to the cube increase strongly with an increase in strength (4) and is approximately equal to (1) at strengths of more than (100MPa.).

In the current results the average ratio of the compressive strength of the cubes (f_{cube}) in size $150 \times 150 \times 150$ mm to the cubes of size $100 \times 100 \times 100$ mm was 0.90 and the average ratio of the compressive strength of the cylinders (f_{cyl}) in size of 100×200 mm to the cylinder of size 150×300 mm determined was 0.88. These results very close to the results obtained by Hamad , who studied the effects of size and shape of specimens on the compressive strength of high performance lightweight foamed concrete ,their ratios determined and averaged were 0.909 for cubes and 0.87 for cylindrical specimens.

50 Mpa. The cylinder/cube strength ratio rises progressively, and was reaching (0.89).

$\varphi3 = 0.90$ for strength grade-3 or SCC-3

From cylinder (100X200) to cube of size 150 mm, for SCC and high strength SCC. $\varphi1=$ 0.95 for strength grade-1 or SCC-1

$\varphi2 = 0.98$ for strength grade-2 or SCC-2

$\varphi1= 0.81$ for strength of grade-1 or SCC-1

$\varphi2 = 0.87$ for strength grade-2 or SCC-2

$\varphi2 = 0.99$ for strength grade-2 or SCC-2

The (CEB-FIP Design Code)[15] gives a similar table of equivalence strength, but above
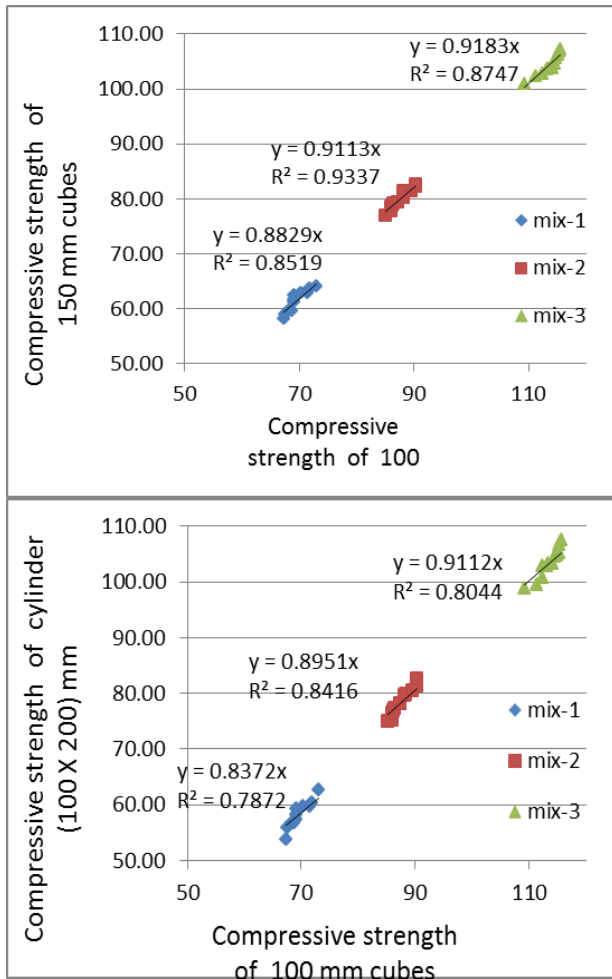
Figure-2 Relation between the compressive strength of SCC for different shapes and sizes of testing specimens; (A) tested by 150 mm cubes versus by 100 mm cubes; (B) tested by cylinders (100 X 200) mm versus to that tested by 100 mm cubes.
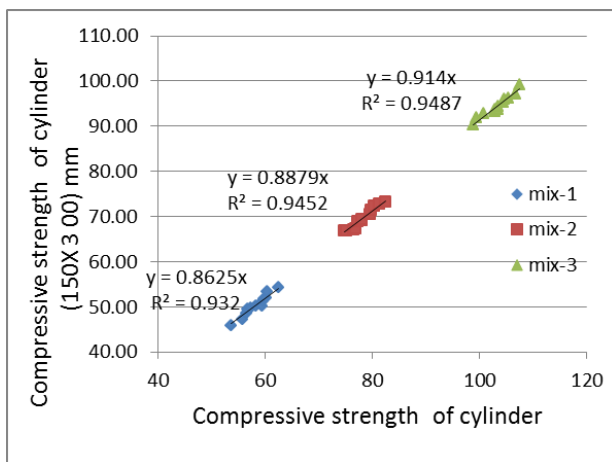
Figure-3 Relation between the compressive strength of SCC for different shapes and sizes of testing specimens; (A) tested by 150 X 300 mm cylinders versus to the
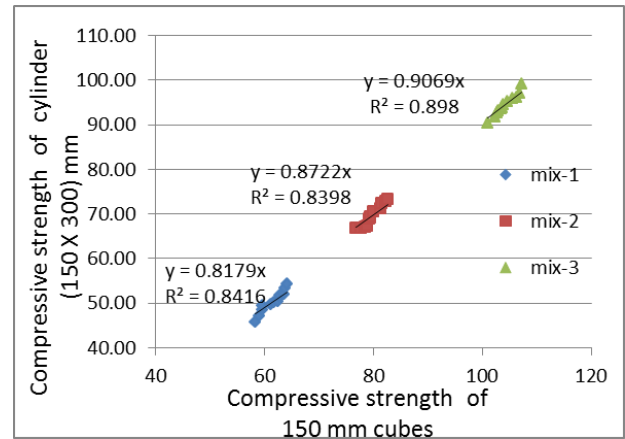
strength tested by 100X 200 mm cylinders; (B) tested by cylinders (150 X 300) mm versus to that tested by 150 mm cube.

4. CONCLUSIONS

Based on the results of this study the following conclusions can be drawn.

1. On average the ratio of compressive strength of Self compacted concrete of 150 X 300 mm cylinders to 150 mm cubes was 0.86

2. On average the ratio of compressive strength of self-compacted concrete of 100 X 200 mm cylinders to 150 mm cubes was 0.97

3. On average the ratio of compressive strength of self-compacted concrete of 100 mm to 150 mm cubes was 1.10

4. On average the ratio of compressive strength of self-compacted concrete of 100 X 200 mm to 150 X300 mm cylinders was 1.13

5. The obtained results indicated that increasing strength of concret

6. increased strength ratios of cylinders to cubes regardless of size and increased strength ratios of big specimens to that of small specimens regardless of shape of specimens.

REFERENCES

ASTM C 39, 2003. Standard Test Method for Compressive Strength of Cylindrical Concrete Specimens. Annual Book of ASTM Standards, vol. 04.02.

BS EN 12390-3, "Testing hardened concrete. Compressive strength of test specimens", BSI, 31 May-2009.

Day, K.W. "Concrete Mix Design, Quality Control and Specification" (third ed.)Taylor & Francis e-Library (2006).

E.I. Al-Sahawneh, "Size effect and strength correction factors for normal weight concrete specimens under uniaxial compression stress", Contemp. Eng. Sci., 6 (2) (2013), pp.57–68.

A.M. Neville, J.J. Brooks, Concrete Technology, (second ed.)Prentice Hall, Pearson Education (2010)

Jin.-keum. Kim, Y. Seong-Tae, "Application of size effect to compressive strength of concrete members India, 27 (4) ,2002, pp. 467–484

Shetty, M.S. "Concrete Technology, Theory and Practice, S. Chand & Company Ltd, India ,2005

Neville A.M., "Properties of Concrete", Pitman, Wiley, New York and Longman, London, 5th and final edition, 2000

ENV 206, 1990, "Concrete: Performance, Production, Placing, and Compliance Criteria", European Standard.

Al-Hayderi H.S, "Correlation Between Strength of Different Sizes,Shapes and Curing Conditions for High Strength Concrete", M.Sc. Thesis, Al-Mustansiriya University, Baghdad, Iraq, 2003.

Carino N.J., Guthrie W.F. and Lagergren E.S., "Effects of Testing Variables on the Measured Compressive Strength of High-Strength (90Mpa.) Concrete", NISTIR 5405, National Institute of Standards and Technology, Gaithersburg, MD, Oct., 1994, pp. 141.

Aitcin P.C., Uncvcrste, Desher, Borooke, Quebec, "High Performance Concrete", London and New York, 1998.

Aitcin P.C., Miao B., Cook W.D. and Mitchell D., " Effect of Size and Curing on cylinder Compressive Strength of Normal and High-Strength Concrete", ACI Materials Journal, Jul.-Aug, Vol.91, No.4, 1994, pp. 349-354.

ACI Committee 237, " Self consolidating Concrete", ACI manual of Concrete practice , 2007

CEB-FIP, "Model Code 1990", Thomas Telford, London, pp: 437, 1993.

BS EN-12350-10, " Testing fresh concrete. Self-compacting concrete. L Box test", BSI , BS EN 12350-10, 31 August 2010.

Hamad, A.J., " Size and shape effect of specimen on the compressive strength of HPLWFC reinforced with glass fibers", Journal of King Saud University, Engineering Sciences, 2015.
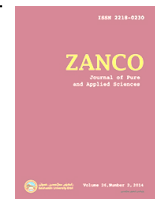
Shear Strength Comparison of High Performance Reinforced Concrete Deep Beams without Stirrups Between ANSYS vs Experimental Work

Omar Q. Aziz[1], Mohammad A. Ihsan[2], Sinan A. Yaseen[3]

1,2,3-Civil Engineering Dept., University of Salahaddin, Erbil, Iraq

ARTICLE INFO

*Corresponding Author:
Sinan A. Yaseen

Sinan.yaseen@su.edu.krd

ABSTRACT

This study presents a theoretical analysis of high performance reinforced concrete deep beams without stirrups based on three-dimensional finite element (FE) models to predict the shear stress, shear strain, load deflection, and crack propagation of 16specimens via ANSYS (v14).The variables considered in the experimental program were compressive strength (normal strength concrete, 40 MPa; high strength concrete, 60 MPa; and high performance concrete, more than 100MPa), shear span-to-depth ratio (1, 1.5, 2, 2.5, and 3), and the ratio of the amount of flexural steel bars (1.35%, 2.40%, 3.76%, and 6.108%). Results obtained with ANSYS were compared with the experimental results to verify the accuracy of the FE models. The general behaviors based on the linear and nonlinear ranges up to failure of the FE models show good agreement with the experimental data. The effect of each parameter was discussed and compared with those in experimental works.

1. INTRODUCTION

Reinforced concrete deep beams are used as load-distributing structural elements, such as transfer girders pile caps, foundation walls, and offshore structures. The shear strength evaluation of reinforced concrete beams has been the subject of several studies that aimed to determine the influences of major parameters. The combination of stresses (bending and shear) in the shear span results in inclined cracks, which transform the beam into a tied arch. In general, reinforced concrete deep beams should have adequate shear reinforcement to prevent sudden and brittle failure after the formation of diagonal cracks, as well as to keep crack width at an

acceptable level. Shear force presents in beams at sections at which bending moment changes along the span; it is equal to the rate of change of the bending moment.

Using of deep beam in construction sector has increased due to its improved properties compared to ordinary beams. Shear resistance is one of most intensive area of research in deep beams. To Estimate the shear resistance of beams, researchers and standard codes have specified different formula considering different parameters into consideration. Choosing an appropriate model for predicting shear resistance of reinforced concrete deep beams was difficult

because of disagreement between researchers and different codes that considered too many parameters. Therefore, an extensive research work on shear behavior of deep beams casting with different strength: normal strength concrete (NSC), high performance concrete (HPC), and high strength concrete (HSC), which is a concrete with a specified compressive strength of 55MPa or greater (ACI, 2013a). HPC is a concrete that meets special combinations of performance and uniformity requirements that cannot always be achieved routinely using conventional constituent materials and normal mixing, placing, and curing practices(ACI, 2013b).

The major researchers in this field include (Bazant Z.P. , 1986), (Zsutty T.C., 1971), (Aziz O.Q., 2014), (Yaseen S.A., 2016), and many more. Estimation of shear resistance of different strength deep beams is still controversial therefore it's a thrust area for research.

The shear failure of reinforced concrete beams without web reinforcement is a distinctive case of failure which depends on various parameters such as shear span to effective depth ratio, longitudinal tension steel ratio, aggregate type, strength of concrete, type of loading, and support conditions, *etc*. Most of the researchers concluded that failure mode is strongly dependent on the shear span to depth ratios (*a/d*). Given the small span–depth ratio of a deep beam, its strength is typically controlled by shear strength rather than by flexural strength if the normal amount of longitudinal reinforcement is applied (Gaetano Russo, 2005, Shyh-Jiann H., 2000). Several experimental studies have been conducted to understand the various modes of failure that could occur because of the possible combination of shear and bending moments acting at a given section. The main obstacle to the shear problem is the large number of parameters involved (Boris B., 1963, Dileep K.).

(Berg F. j., 1962), (Taylor R., 1960) study a shear capacity of varied shear span to effective depth ratio in Reinforced concrete beams.

(Sudheer Reddy L., 2011) studies evaluation of shear resistance of high strength concrete beams without web reinforcement using ANSYS. (Fanning P., 2001) evaluated reinforced and post tensioned concrete beams using the ANSYS.

The present study analysis twelve different strength deep beam ANSYS model using finite element analysis. One of the main advantages of ANSYS is the integration of the three phases of finite element analysis: preprocessing, solution, and post-processing. Pre-processing routines in ANSYS involve defining the model, boundary conditions, and loadings. Displays may be created interactively on a graphics terminal as the data are entered to assist model verification. Post-processing routines may be used to retrieve analysis results in a variety of ways. Plots of the deformed shape of a structure and stress or strain contours can be obtained in the post-processing stage. The analysis of the tested beams is carried out in 'ANSYS' package considering perfect bond between the tension reinforcement and the surrounding concrete. The predicted results using 'ANSYS' model, have been compared with the corresponding test data in (Yaseen S.A., 2016).

2. OBJECTIVES

i.   Study the shear response of concrete beams without shear reinforcement by taking the variables, compressive strength (normal strength concrete, 40 MPa; high strength concrete, 60 MPa; and high performance concrete, more than 100MPa), shear span-to-depth ratio (1, 1.5, 2, 2.5, and 3), and the ratio of the amount of flexural steel bars (1.35%, 2.40%, 3.76%, and 6.108%) into consideration.

ii. Develop and analyze different strength concrete deep beam models in ANSYS and compare the results with the experimental data; and

3.FINITE ELEMENT MODEL

REPRESENTATION

As mentioned previously, the ANSYS computer program was used to analyze all the tested beams. The finite element modeling and analysis techniques used to simulate the behavior of high performance reinforced concrete deep beams are described following the element definition in the aforementioned program. The element types utilized to construct the FEM are discussed below.

3.1. Finite element model of fiber reinforced concrete

Concrete members consist of concrete and steel fibers. The finite element idealization should be able to represent concrete cracking, crushing, and the interaction between concrete and reinforcement. The interaction between the two materials is needed to reduce crack growth and the capability of concrete to transfer shear stress after cracking via an aggregate interlock. Three-dimensional elements are used to investigate failures in which shear stress plays a major role. A 3D solid element with eight nodes was used to model the concrete (SOLID-65). The element comprised eight corner nodes (Fig. (1)), and each node had three degrees of freedom (u, v, and win the x, y, and z directions, respectively). The element is capable of plastic deformation, cracking in three orthogonal directions, and crushing. The steel fibers used in this study were straight steel wire fibers (undeformed). The fibers showed an aspect ratio (l/d) of 80, a nominal diameter of 0.2 mm, a nominal length of 40 mm and the volume fracture is $V_f = 1\%$. Internal reinforcement (flexural and shear stirrups) was modeled using 3-D spar elements (Link180), which allow the elastic–plastic response of reinforcing bars (ANSYS, 2011).
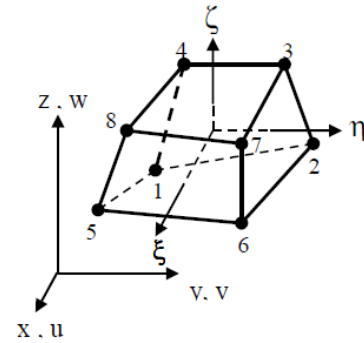
Figure (1): Three-dimensional eight-node solid element

3.2. Finite element model of reinforcement bars

The finite element modeling of steel reinforcement can be realized with three techniques (ANSYS, 2011), namely, discrete, embedded, and smeared (distributed) representations (Fig. (2)). The steel reinforcements (tensile, compressive, stirrups, and dowel bars) were represented by using a two-node discrete representation (LINK-8) and were included within the properties of eight-node solid elements. In general, reinforcement bars are assumed capable of transmitting axial forces only, and a perfect bond is assumed to exist between the concrete and the reinforcing bars.

To provide the perfect bond, this study connected the link element for the steel reinforcement bar between the nodes of each adjacent concrete solid element such that the two materials shared the same nodes. The stress–strain curve of steel reinforcement for the FEM was based on the actual stress–strain curve obtained from the tensile tests.
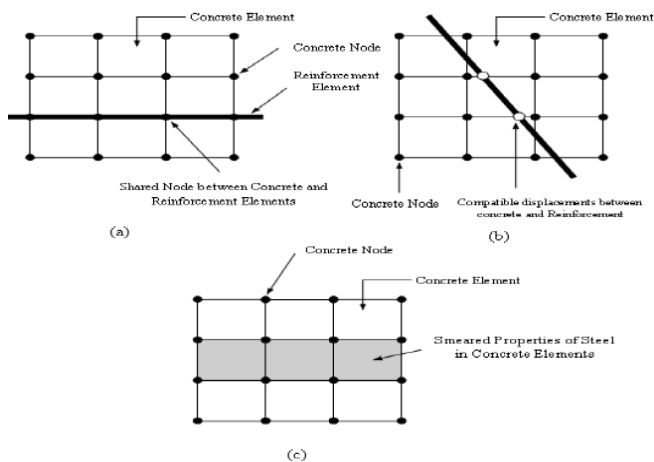
Figure (2): Reinforced concrete model representations (a) Discrete; (b) Embedded; and (c) Smeared

3.3. Steel plates

A 12.5mm-thick steel plate was added at the support locations to avoid stress concentration problems and to prevent the localized crushing of concrete elements near the supporting points and load application locations. These plates were modeled by using Solid185 elements to ensure an even stress distribution over the support area. The element was defined with eight nodes, each of which had three degrees of freedom and translations in the nodal x, y, and z directions (ANSYS, 2011).

4. MODELING OF MATERIAL PROPERTIES

4.1. Stress–strain relationship model for concrete

Concrete is a quasi-brittle material with different compression and tension behaviors. It is assumed to be homogeneous and initially isotropic. Figure (3) shows a typical stress–strain curve for NWC (Desayi P., 1964). However, this ideal stress–strain curve was not used in the finite element material model because the negative slope portion leads to convergence problems. The compressive uniaxial stress–strain relationship for the concrete model was obtained by using the following equations to compute the multilinear isotropic stress–strain curve of concrete (Bangash, 1989).

$$f = \frac{E_c \varepsilon}{1 + \left(\frac{\varepsilon}{\varepsilon_o}\right)^2} \qquad (1)$$

$$\varepsilon_o = \frac{2f'_c}{E_c} \qquad (2)$$

$$E_c = \frac{f}{\varepsilon} \qquad (3)$$

$f = Stress\ at\ any\ strain\ \varepsilon$

$\varepsilon = Strain\ at\ stress\ f$

$\varepsilon_o = Strain\ at\ the\ ultimate\ compressive\ strength\ f'_c$

Figure (4) shows the simplified compressive uniaxial stress–strain relationship that was used in this study. The simplified stress–strain curve for each beam model comprises six points connected by straight lines. The curve starts at zero stress and strain. Point No.1 at $0.40f'_c$ is calculated from the stress–strain relationship of the concrete in the linear range (Equation (3)). Points No. 2, 3, and 4 are obtained from Equation (1), in which ε_0 is calculated from Equation (2). Point No. 5 is at ε_0 and f'_c. In this study, perfectly plastic behavior was assumed after Point No. 5.

The behavior of normal concrete under compression is illustrated in a typical uniaxial stress-strain curve, as shown in Fig. 4, and consists of two parts, linear and nonlinear. The limit of the linear portion is defined as 30% of the maximum compressive strength , the modulus of elasticity (Ec) and Poisson's ratio (calculated from the linear portion). The nonlinear elastic behaviors of concrete can be defined by the multi-linear stress-strain relationships, as illustrated in Fig. 3-4.

For concrete, ANSYS requires input data for material properties as follows: Elastic modulus (Ec), Ultimate uniaxial compressive strength (f'c), Ultimate uniaxial tensile strength (modulus of rupture, fr), Poisson's ratio (ν), Shear transfer coefficient (β), and the Compressive uniaxial stress-strain relationship for concrete.

The elastic modulus (Ec), compressive strength (f'c) and modulus of rupture (fr) were obtained experimentally. Poisson's ratio for the

concrete was assumed to be 0.2 (67) for all four beams. The default values used by the ANSYS which was 0.001 (for values and type of conversion criteria). The shear transfer coefficient represents conditions of the crack face. The value of β ranges from 0 to 1, with 0 representing a smooth crack (complete loss of shear transfer) and 1 representing a rough crack (no loss of shear transfer).
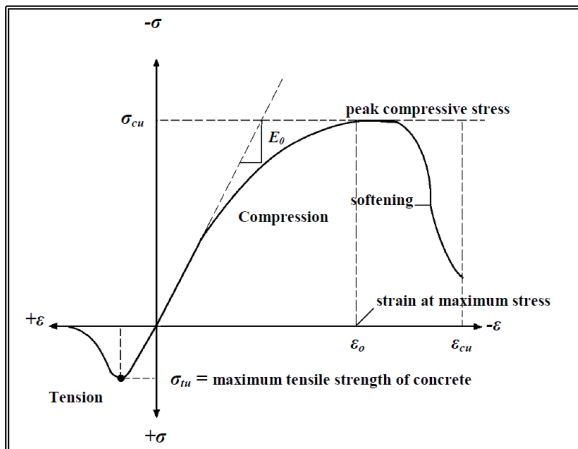
Figure (3): Typical uniaxial compressive and tensile stress – strain curve of concrete[(ACI, 2013a)]
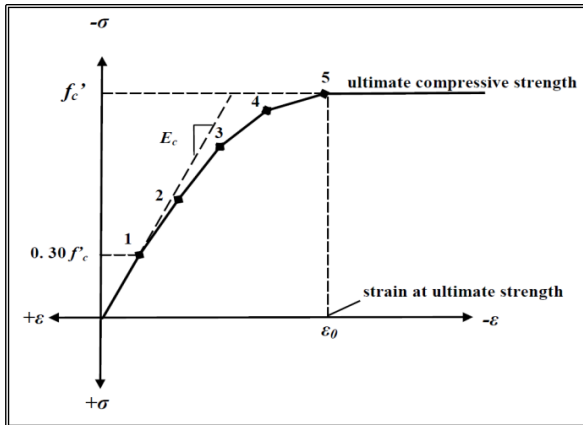
Figure (4): Simplified compressive uniaxial stress – stain curve of concrete[(ACI, 2013b)]

4.2. Geometry and FE modeling of HPC and steel Reinforcement

All the tested beamsmeasured1,250 mm long and had an overall cross section of 100 mm × 200 mm (effective depth d=167mm). All the tested specimens were simply supported over a clear span of 1,000mm. The tested beams were divided into four groups. Figure (5) and Table (1) present the properties and details of the tested specimens [12]. Half of the full beam was used for modeling by taking advantage of the symmetry of the beams. This approach reduced computational time and computer disk space requirements significantly.

5. MESHING

After the creation of volumes, a finite element analysis requires meshing of the model. In other words, the model is divided into a number of small elements, and after loading, stresses and strains are calculated at the integration points of these small elements. In this study, good results were obtained by setting up the mesh such that square or rectangular elements were created (Fig. (6)).

6. TEST MODEL AND EXPERIMENTAL DATA
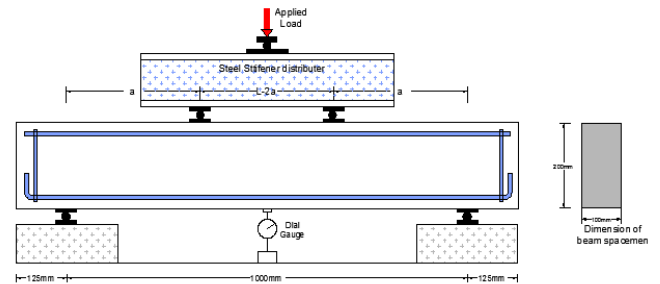
Figure (5): Detail of the tested specimens

Table 1- Detail of the Tested Specimens [(Yaseen S.A., 2016)]

Beam designation		l(mm)	a(mm)	d	a/d	ρ_w%	Concrete type
Series1	G11	1,000	334	167	2.00	6.108	NSC
	G12	1,000	334	167	2.00	6.108	HSC
	G13	1,000	334	167	2.00	6.108	HSC
	G14	1,000	334	167	2.00	6.108	HPC
	G15	1,000	334	167	2.00	6.108	HPC
Series2	G21	1,000	167	167	1.00	6.108	HPC
	G22	1,000	250	167	1.50	6.108	HPC
	G23	1,000	418	167	2.50	6.108	HPC
	G24	1,000	500	167	3.00	6.108	HPC
Series3	G31	668	334	167	2.00	6.108	HPC
	G32	835	334	167	2.00	6.108	HPC
	G33	1,169	334	167	2.00	6.108	HPC
	G34	1,326	334	167	2.00	6.108	HPC
Series4	G41	1,000	334	167	2.00	1.35	HPC
	G42	1,000	334	167	2.00	2.4	HPC
	G43	1,000	334	167	2.00	3.76	HPC

Use 2–25mm as main reinforcement. b= 100mm, d= 167mm for series 1,2, and 3.
Use 2–12, 2–16, and 2–20 mm as main reinforcement. b= 100mm, d= 167mm for series 4.

7. SETTING OF BOUNDARY CONDITIONS AND LOADING POINTS

The best simulation model can be created when the actual boundary conditions used in the modeling act in the same way as the experimental tested beam. Displacement boundary conditions are needed to constrain the model and obtain a unique solution. The model being used is symmetrical about one plane. The boundary conditions for both the support and planes of symmetry are shown in Figure (6). The boundary conditions need to be applied at points of symmetry and at points where support and loading exist.

A vertical plane through the beam center at the mid-span defines the section of the plane of symmetry. To model the symmetry, nodes in this plane must be constrained in the longitudinal direction. Therefore, in this study, the displacements were set as zero in the plane along the Xdirection, (UX = 0). The support was modeled such that that a roller was created. A single line of nodes on the plate was given a constraint in the Y and Z directions, a displacement value of zero (UY=0, UZ=0) was applied. Thus, the beam was allowed to rotate at the support. Force P was applied across the entire nodes of the steel plate.
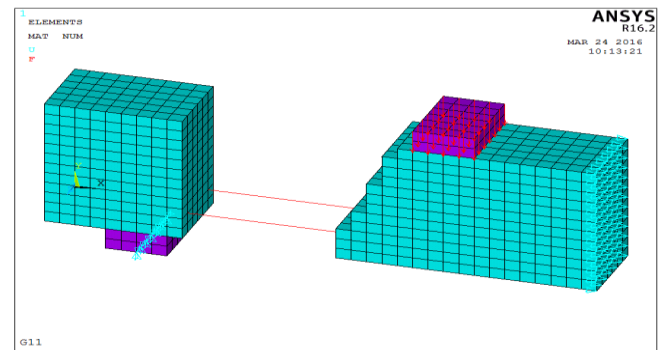
Figure (6): Typical steel reinforcement locations for the half-size beams

8. PREDICTED RESULTS FROM THE FINITE ELEMENT MODEL (FEM)

The results from the ANSYS-FEM include the following:
1. Ultimate load capacity and failure modes
2. Ultimate shear stress and strain distribution
3. First shear and flexural cracking loads
4. Load deflection curve
5. Pattern of propagating cracks

9. ULTIMATE LOAD CAPACITY (FAILURE LOAD)

The theoretical ultimate load capacity (which was considered the last converged load in the FEM analysis) and the mode of failure for all the tested beams are listed in Table (2) and shown in Figures (7) and (8). The figures explain half of the loaded beam according to the symmetry section. Thus, one support and a loading point appear to show a failure region between the two points (loading point at the top and supporting point at the bottom of the beam).

The predicted load shows good agreement with the experimental results. The overall percentage of the experimental load to the predicated load (ANSYS model) was100%, thereby indicating indicates the perfect calibration of the ANSYS-FEM to perform the simulations close to reality.
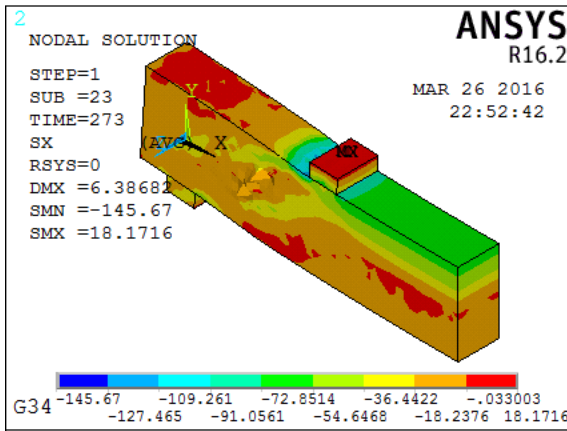
Figure (7): Shear compressive failure mode
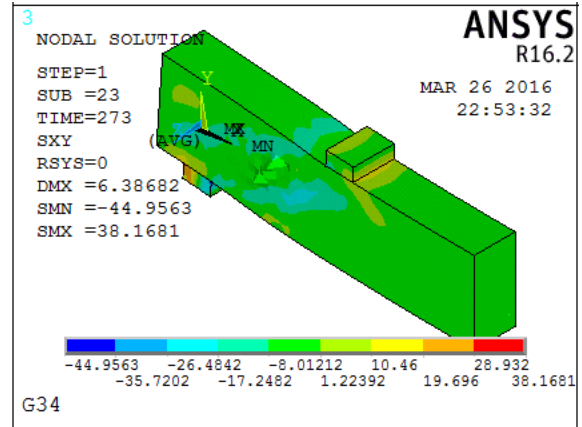
Figure (9): Shear stress distribution for beam (G34)
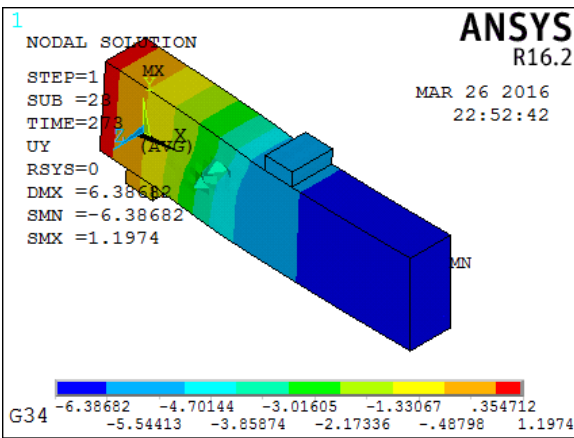
Figure (8): Diagonal tension failure mode
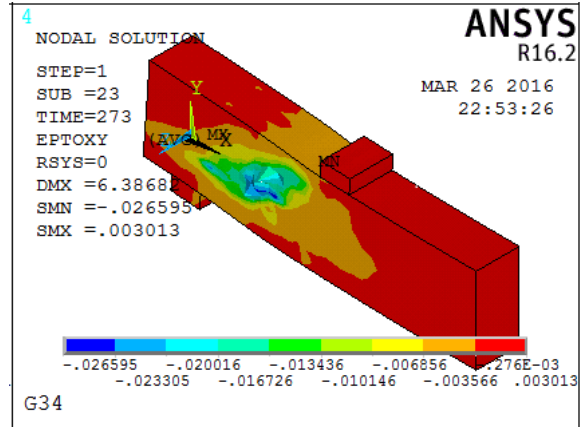
Figure (10): Strain intensity for beam (G34)

10. MAXIMUM SHEAR STRESS AND STRAIN INTENSITY

The maximum shear stress for all the tested beams is shown in Table (2). The maximum shear stress was considered as the (XY) shear stress at the last converged iteration before failure.

The overall theoretical results were higher than those from the experimental work by approximately 1%. The stress distribution across the side surface of the beam specimen (G3-4) shown in Figure (9) exhibited a maximum shear stress of 17.24MPa. The strain intensity for the beam specimen (G3-4) is shown in Figure (10), which clearly depicts the likelihood of diagonal tension failure.

11. FIRST CRACKING LOAD

The theoretical first (shear or flexural) cracking load is the load step where the first signs of cracking occur in concrete elements. Cracking became visible on the sides of the beam at 23%–33% of the ultimate load in the experimental data and at 19%–29% in the prediction model. As expected, this cracking consisted of inclined cracks in a region of shear load. The result of the first cracking load for the tested beams in the predicted model was compared with that from the experimental data, as shown in Table (2). The ratio of comparison between the experimental results and the predicted results was 108% for shear load and 111% for flexural load. The load needed in the first crack in the experimental data results was greater than that obtained by the predicted model. This outcome can be explained as

follows. The experimental cracking load is the load at which the first visible crack (shear or flexural) appeared, where as the theoretical cracking load is the load step in which one of the principal stresses in the concrete element reached the maximum limit.

12. LOAD-DEFLECTION CURVES

In the experimental beams, direct current displacement transducers were used to measure the deflections at mid-span at the center of the bottom face of the beams. In the ANSYS-FEM, mid-span deflection was calculated at the same location as that for the experimental beam. The load-deflection curves from the FEM and the experimental results for the beam specimens (G1-5), (G2-3), (G3-4), and (G4-3) are shown in Figures (11), (12), (13), and (14), respectively.

The graph shows that the load-taking capacity of the specimen in the predicted model was slightly greater than that of the experimental data for all the beam specimens. As a result, the predicted load-deflection curves show good agreement with those in the experimental work. The deflection capacity was improved in the model, and the cracks were reduced in all modeled specimens. The ANSYS model results were stiffer than the experimental results possibly because of the following:

> 1- The non-consideration of the micro-cracks in concrete (because of drying shrinkage)
> 2- The bond slip of the reinforcement and the assumed perfect bond between the concrete and the reinforcement bar in the FEM, which may not be true for actual beams
> 3- The first cracking loads obtained from the ANSYS-FEM being lower than those from the experimental results in the pre-cracking stages.

Considering Load-Deformation response, there is some discrepancy at the early stages;

> However, the overall trend of the ANSYS response is corresponding the experimental results.
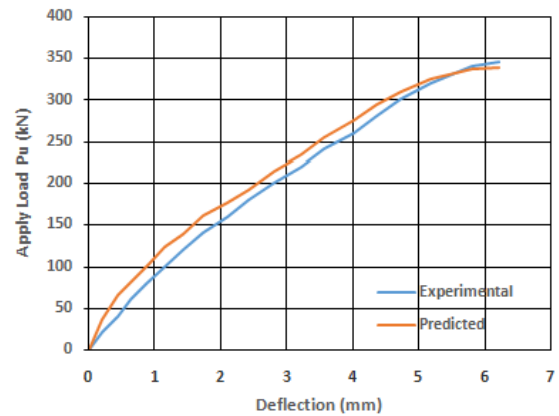
Figure (11): Experimental and predicted load-deflection curve for beam G2-3
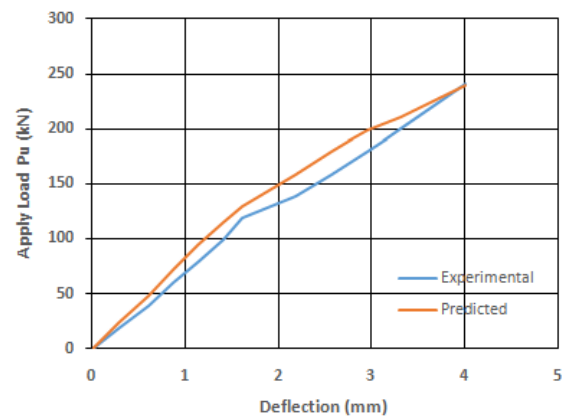
Figure (12): Experimental and predicted curve for beam G2-3
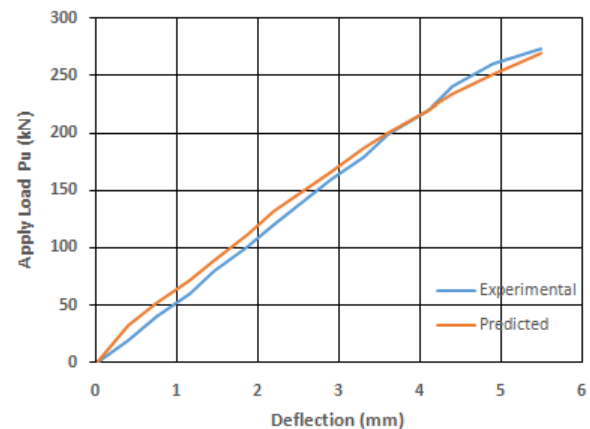
Figure (13): Experimental and predicted load-deflection load-deflection curve for beam G3-4
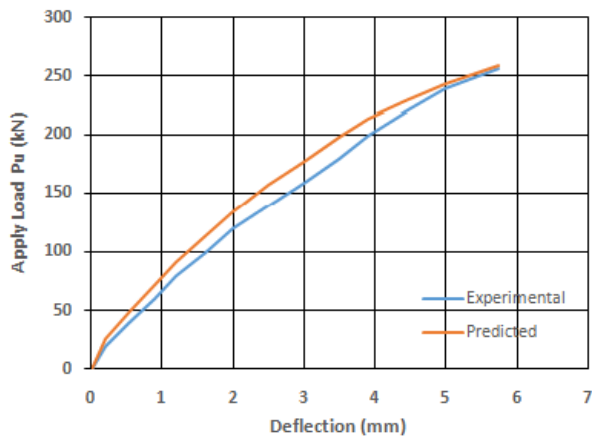
Figure (14): Experimental and predicted curve for beam G4-3

13. CRACK PATTERN

The ANSYS program records a crack pattern at each applied load step. A cracking sign represented by a circle appears when a principal tensile stress exceeds the ultimate tensile strength of concrete. The cracking sign appears perpendicular to the direction of the principal stress. In general, flexural cracks occur early at mid-span. When applied loads increase, vertical flexural cracks spread horizontally from the mid-span to the support. At a high applied load, diagonal tensile cracks appear. Increasing the applied load induces additional diagonal and flexural cracks. Given that the model is a shear beam model (deep beam), no compressive cracks appeared underneath the loading location.

An example of the predicted flexural crack pattern is shown in Figure (15) for beam (G1-1), and the predicted shear crack pattern is shown in Figures (16) and (17) for beams (G1-1) and (G1-2). The stress vector pattern was obtained from the solution of beam (G1-2). The amount of cracks from the ANSYS-FEM analysis is greater than that observed in the experimental test. No more than three cracks can be predicted in each Solid65 element for the FEM. Therefore, the amount of cracks shown is affected by the size of the mesh. Using a large mesh size for Solid65 elements would result in few elements and minimal cracks, whereas using a small mesh size would result in the opposite conditions.

**Table 2- Experimental and Predicted First Cracking Load, Ultimate Load Capacity,
Ultimate Shear Stress, and Mode of Failure for All Tested Specimens**

Beam No.	Experimental compressive Strength MPa	Experimental First Flexural Cracking Load M(kN)	Predicted First Flexural Cracking Load (kN)	% (Experimental/Predicted) First Flexural Cracking Load	Experimental First Shear Cracking Load MPa	Predicted First Shear Cracking Load MPa	% (Experimental/Predicted) First Shear Cracking Load	Experimental Failure Load (kN)	Predicted Failure Load (kN)	% (Experimental/Predicted) Failure Load	Experimental Ultimate Shear Stress MPa	Predicted Ultimate Shear Stress MPa	% (Experimental/Predicted) Ultimate Shear Stress	Experimental Mode of Failure	Predicted Mode of Failure
G1-1	43	43	39.5	109	51	45.2	113	130	132.5	98	3.8	3.97	98	Diagonal	Diagonal
G1-2	61	51	46.5	110	90	82.5	109	201	200.8	100	6.0	6.01	100	Diagonal	Diagonal
G1-3	79	52	51.8	100	104	90.4	115	264	258.9	102	7.9	7.75	102	Diagonal	Diagonal
G1-4	100	53	56.3	94	90	81.2	111	311	311.8	100	9.3	9.34	100	Diagonal	Diagonal
G1-5	119	55	60.4	91	97	88.7	109	345	338.4	102	10.	10.13	102	Diagonal	Diagonal
G2-1	97	117	102.8	114	160	137.	116	716	698.5	103	21.	20.91	103	Diagonal	Diagonal
G2-2	101	88	81.3	108	120	106.	112	520	531.5	98	15.	15.91	98	Diagonal	Diagonal
G2-3	101	44	40.2	109	44	42.3	104	241	239.4	101	7.2	7.17	100	Diagonal	Diagonal
G2-4	101	48	44.6	108	48	44.6	108	145	142.9	101	4.3	4.28	101	Diagonal	Diagonal
G3-1	101	47	39.4	119	83	70.4	118	380	378.9	100	11.	11.34	100	Diagonal	Diagonal
G3-2	101	50	44.6	112	70	61.8	113	340	342.6	99	10.	10.26	99	Diagonal	Diagonal
G3-3	101	48	43.5	110	44	38.5	114	284	284.8	100	8.5	8.53	100	Diagonal	Diagonal
G3-4	122	48	42.3	113	50	44.1	113	273	269.1	101	8.1	8.06	101	Diagonal	Diagonal
G4-1	122	49	46.8	105	73	69.8	105	170	171.5	99	5.0	5.13	99	Diagonal	Diagonal
G4-2	122	49	47.4	103	74	71.4	104	225	225.6	100	6.7	6.75	100	Diagonal	Diagonal
G4-3	118	60	49.2	122	80	75.6	106	257	259.6	99	7.6	7.77	99	Diagonal	Diagonal
Average				108			111			100			100		

Thus, the cracks shown as contours of the point at which the tensile stress exceeds the tensile strength of concrete are appropriate to consider.
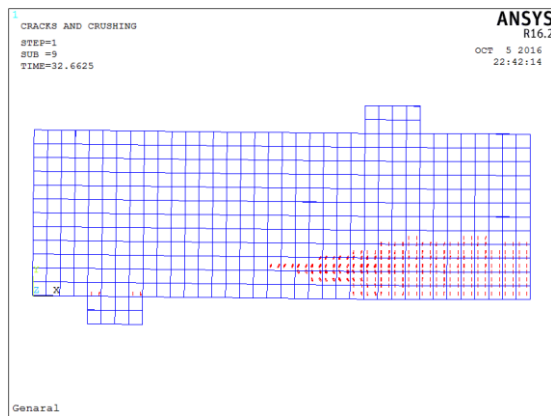
Figure (15): Flexural crack pattern for beam (G1-1)
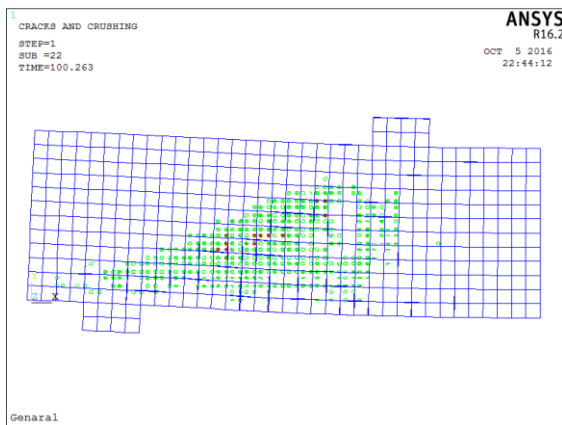
Figure (16): Shear crack pattern for beam (G1-1)
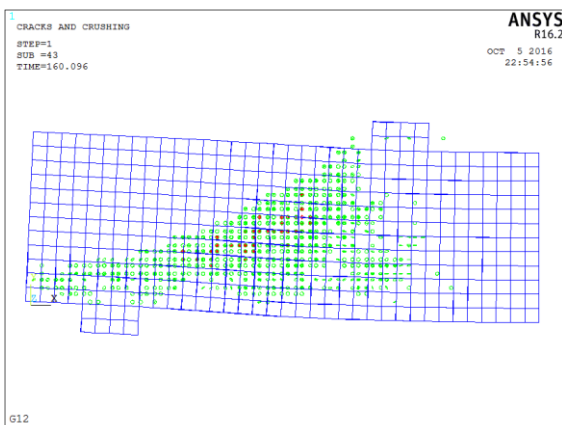
Figure (17): Shear crack pattern for beam (G1-2)
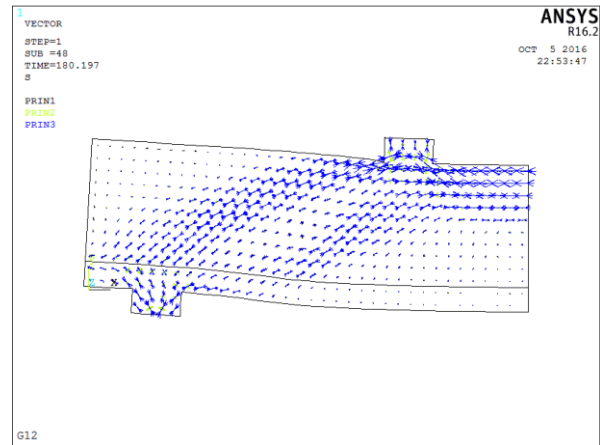
Figure (18): Stress vector pattern for beam (G1-2)

14. CONCLUSIONS

The following conclusions can be derived from the predicted models based on FEM:

1. The ultimate final deflection, load-deflection curves, and mode of failure predicted with the FEM show good agreement with the experimental results.

2. The effect of additional variables, such as loading type, the value of $\left(\frac{a}{d}\right)$, and the main reinforcement ratio, on the shear behavior of high performance reinforced concrete deep beams was considered in the FEM.

3. The experimental/predicted failure loads for all the tested beams were within 100%, whereas the FEM seemed stiffer than the experimental model during loading. This result is due to the absence of micro-cracks in the FEM and the assumed perfect bond between the concrete and the reinforcement bar.

4. The first (shear and flexural) cracking load predicted with the FEM for all the tested beams was lower than that from the experimental works tested with 108% shear load and 111% flexural load). The experimental first cracking load is the load at which the first visible crack (shear or flexural) appeared, where as the theoretical cracking load is the load step at which

one of the principal stresses in the concrete element reached the maximum limit.

5. The number of cracks in the FEM was greater than that observed in the experimental test because the amount of cracks shown is affected by the size of the mesh used.

6. The predicted crack pattern can be considered contours of points at which the tensile stress exceeds the tensile strength of concrete instead of as indicators of the number of cracks, crack spacing, or crack width.

7. The predicted ultimate shear stresses were higher than those from the experimental work by approximately 1% for all the tested beams.

8. The predicted shear stress intensity from the FEM can be used to study the shear stress distribution along the deep beam depth in various loading stages.

REFERENCES

ACI 2013a. COMMITTEE-363, State of the Art Report on High Strength Concrete. *ACI MANUAL OF CONCRETE PRACTICE.*

ACI 2013b. CT-13, ACI Concrete Terminology. *ACI STANDARD.*

ANSYS 2011. ANSYS User's Manual Revision 5.5. Canonsburg, Pennsylvania: ANSYS, Inc.

AZIZ O.Q. 2014. Shear strength and behavior of ultra high performance reinforced concrete deep beams with stirrups. *Zanco journal of pure and applied science,* 26(2).

BANGASH, M. Y. H. 1989. *Concrete and Concrete Structures: Numerical Modeling and Applications,* London, Elsevier Science Publishers Ltd.

BAZANT Z.P. , K. J. K. 1986. Size Effect in Shear Failure of Longitudinally reinforced beams. *ACI Journal Proceedings,* 83(2)**,** 456-468.

BERG F. J. 1962. Shear Strength of Reinforced Concrete Beams without Web Reinforcement. *Journal of ACI,* 59(11)**,** 1587-1599.

BORIS B. 1963. Shear Strength of Reinforced Concrete Beams. *Journal of the American Concrete Institute,* 60(1)**,** 51-72.

DESAYI P., K. S. 1964. Equation for the Stress-Strain Curve of Concrete *Journal of the American Concrete Institute,* 61(3)**,** 345-350.

DILEEP K. *RE: Shear Strength of R.C.C Beams without Web Reinforcement.*

FANNING P. 2001. Non-linear models for reinforced and post-tensioned concrete beams. *Electronic Journal of Structural Engineering,* 2**,** 111-119.

GAETANO RUSSO, R. V., AND MARGHERITA PAULETTA 2005. Reinforced Concrete Deep Beams-Shear Strength Model and Design Formula. *ACI Structural Journal,* 102(3)**,** 429-437.

SHYH-JIANN H., W.-Y. L., HUNG-JEN L., 2000. Shear Strength Prediction for Deep Beams. *ACI Structural Journal,* 97(3)**,** 367-376.

SUDHEER REDDY L., R. R. N. V., GUNNESWARA RAO T. D., 2011. Evaluation Of Shear Resistance Of High Strength Concrete Beams Without Web Reinforcement Using ANSYS. *ARPN Journal of Engineering and Applied Sciences,* 6(2).

TAYLOR R. 1960. Some Shear Tests on Reinforced Concrete Beams without Shear Reinforcement. *Magazine of Concrete Research.*

YASEEN S.A. 2016. An Experimental study on the shear strength of high performance reinforced concrete deep beams without stirrups. *Eng. & Tech. journal,* 34(11),PART (A).

ZSUTTY T.C. 1971. Shear Strength Predictions for Separate Categories of Simple Beam Tests. *ACI Journal, Proceedings,* 68(2)**,** 138-143.
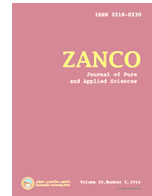
MTHFR C677T polymorphism and thyroid cancer risk in Duhok, Kurdistan Region –Iraq

Soleen Sardar Zuhdi[1], Ahmed Mohammed Salih [2], Zeki Ali Mohammad [3], Intisar Salim Pity [4]

1- Reporter of Duhok Medical Research Center, assistant lecturer of cytogenetic, college of medicine, university of Duhok, Kurdistan Region, Iraq

2- Head, Duhok Medical Research Center, assistant professor of molecular biology & immunology, college of medicine, university of Duhok, Kurdistan Region, Iraq

3- Director of hematology - oncology center, Azadi teaching hospital, lecturer, department of internal medicine, college of medicine, university of Duhok, Kurdistan Region, Iraq

4- Professor of histopathology, department of pathology, college of medicine, university of Duhok, Kurdistan Region

A R T I C L E   I N F O

A B S T R A C T

Thyroid malignant tumors are common endocrine cancers that increased in incidence worldwide during the last decade. The disease recurrence is high, despite the death rate due to thyroid cancer is low. The etiology of thyroid cancer is still controversial, however, numerous genetic alterations in various thyroid tumors have been identified. Mutations in a gene encoding folic acid metabolizing enzyme, (Methyl Tetra Hydro Folate Reductase), named as (*MTHFR*), particularly the single nucleotide polymorphism *MTHFR* C677T has attracted our concern as a potential cause implicated in thyroid cancer. Formalin-fixed paraffin-embedded (FFPE) thyroid specimens with papillary carcinoma of 52 patients (18 male and 34 female) were donated kindly by Duhok histopathologic laboratories (Health Central laboratory). A group of 55 apparently healthy subjects were recruited (30 male and 25 female), after getting their formal consent. The DNA was isolated from both of the FFPE thyroid specimens of the patients and the venous blood samples of the healthy controls. The *MTHFR* polymorphism C677T was examined using the PCR-RFLP method using *Hinf*I restriction enzyme. The thyroid cancer group consisted of 18 (34.6%) males and 34 (65.4 %) females, their age mean was 42.41 years. The cases were 3 (5.8%) anaplastic carcinoma, 43 (82.7%) papillary carcinoma, 4 (7.7%) follicular carcinoma and 2 (3.8%) medullary carcinoma. The control group consisted of 30 (54.5%) males and 25 (45.5%) females, their age mean was 43.6 years. The frequency of *MTHFR* C677T (CC, CT) heterozygous and TT homozygous variants among 52 thyroid cancer patients were 59.6%, 15.4% and 25% respectively, and the CT +TT combined variants were 40.4%. There was statistical significant difference between the *MTHFR* CC wild genotype and *MTHFR*C677T (CT,TT) variants. Among the 55 healthy controls, the *MTHFR* C677T genotype variants frequency of CC, CT heterozygous and TT homozygous were 85.%, 3.6% and 10.9% respectively, and the frequency of combined CT heterozygous +TT homozygous variants among the healthy controls was 14.5%. In conclusion, our results did not support a statistical association of the *MTHFR* C677T gene polymorphism variants with the risk of developing thyroid cancer neither with gender nor age adjustment.

1. INTRODUCTION

Thyroid cancer is a common endocrine malignancy that has rapidly increased in global incidence in recent decades, it forms 1-10% of all cancers in women, 1-3% in men and about 1.4% in children (Jamil *et al*.,2011; Howlader *et al*.,2012). In Iraq, the prevalence of thyroid cancer is 1.01/100,000. In Kurdistan Region-Iraq, thyroid cancer crude rates reported during 2007, 2008 and 2009 periods ranged from 0.28-0.57/100,0005 (Othman *et al*., 2011; World health organization WHO,2004; Othman, 2011). The recurrence rate of the disease is relatively high, but the death rate among thyroid cancer patients is low (Tuttle *et al*.,2010). Several histopathological types with various cellular origins and characteristics with prognostic importance are defined to be associated with thyroid cancer. (DeLellis *et al*.,2004), those cells are of two types, follicular thyroid cells and parafollicular C cells, and thyroid cancer cells are derived from them. The majority of malignant thyroid tumors are derived from follicular thyroid cells which include - anaplastic thyroid cancer, papillary thyroid cancer, follicular thyroid cancer, and poorly differentiated thyroid cancer, where as parafollicular C cell-derived medullary thyroid cancer (MTC) has a small proportion among thyroid malignancies(Howlader *et al*.,2012).

The exact cause of thyroid malignancies is yet unknown, but ionizing radiation could be regarded as the most verified cause of thyroid cancer, specifically when radiation exposure happens at younger ages, also iodine deficiency in diet has been found to be linked to this type of pathology (Ron *et al*., 1995; Lund *et al*., 1999). Molecular genetic changes that have a crucial role in the tumor formation of different thyroid cancers have been reported. The T1799A transverse point mutation of *BRAF* gene is an example of a mutated gene that

encodes BRAF-V600E mutant protein that leads to the activation of the serine/threonine kinase signaling pathway constitutively (Cohen *et al*., 2003;Fukushima *et al*.,2003). *BRAF*^{V600E} mutation occurs in approximately 45% of PTCs (Xing M, 2005). Few other rare mutations in *BRAF* gene are reported in papillary thyroid cancer that affect nucleotides around codon 600, which activate the BRAF serine/threonine kinase pathway constitutively (Hou P, 2007; Trovisco *et al*., 2005). RAS mutations are the second in the prevalence related to *BRAF* mutations associated with thyroid cancer. The other genes that are identified to be implicated in thyroid tumor-genesis are β-catenin (*CTNNB1*) (Garcia-Rostan *et al*., 1999 ; Garcia- Rostan *et al*., 2001), *TP53(*Fagin *et al*., 1993*;* Donghi *et al*., 1993*)*, isocitrate dehydrogenase 1 (*IDH1*) (Murugan *et al*., 2010; Hemerly *et al*., 2010), anaplastic lymphoma kinase (*ALK*) (Murugan *et al*, 2011) and epidermal growth factor receptor (*EGFR*) (Murugan, Dong J *et al*., 2011).It has also been suggested that individuals possessing a modified ability to metabolize carcinogens are at increased risk of cancer (Laverdiere *et al*, 2002; Matsuo *et al*, 2004). A gene encoding folic acid metabolizing enzyme, methylenetetrahydrofolate reductase *MTHFR* C677T mutation has attracted our concern as a potential cause implicated in thyroid cancer. The balances the pool of folate coenzymes is controlled by the *MTHFR enzyme,* which is a fundamental enzyme in the DNA synthesis and methylation, both processes are found to be implicated in carcinogenesis of many types of cancers. Studies concerning the *MTHFR* gene polymorphisms have suggested that the low activity of folate metabolizing enzyme is regarded as risk factor in carcinogenesis (Laverdiere *et al*, 2002; Matsuo *et al*, 2004). The *MTHFR* gene is located on chromosome 1p36.3 and gathers a 2 Kbp coding site with

eleven exons (Langevin *et al*, 2009). It plays an important role in the regulation of cellular methylation by assisting the conversion of 5, 10- methylene tetrahydro folate to 5-methyltetrahydrofolate (Lee *et al*, 2004), the latter aids in the remethylation of homocysteine to de novo methionine (Macis *et al*, 2007), which serves as a precursor for the S-adenosylmethionine, a universal methyl donor for methylation reactions (Hosseini *et al*, 2011). Low dietary folate intake, decreased metabolism with no auxiliary folate intake might results in broken DNA molecules, increasing the mutagenesis rate and changes in the methylation profile of the DNA, in turn, affect the expression pathways of many genes (Kotsopoulos *et al*, 2008; Chou *et al*, 2006).So far, there is a controversy over the association between *MTHFR* C677T mutation with the PTC. Furthermore, very few works have studied this gene mutation in PTCs. In our study, we attempted to analyze the relationship between *MTHFR* C677T mutation and PTCs in Duhok city population.

2. MATERIALS AND METHODS

2.1. Subjects and methods

This case control study has been conducted in Duhok Medical Research Center (DMRC) at the college of medicine, university of Duhok, Kurdistan region-Iraq. The readily formalin-fixed paraffin-embedded thyroid specimens containing papillary carcinoma of 52 patients (18 male and 34 female)were donated kindly by Duhok histopathologic laboratories (Health Central laboratory). The specimens were belonging to thyroid cancer patients that were diagnosed between the period of May 2011 and August 2015, and they have received no prior therapy at the time of biopsy taking. All of the histopathological diagnoses and thyroid tumor staging was conducted previously by Pity et

al(2015),briefly, a tissue section of four micron-thick was taken from each tumor specimen, stained with Hematoxylin and Eosin (H&E) for microscopic histopathologic diagnosis (Pity *et al*, 2015).DNA was extracted from the tissue sections using (Qiagen kit-USA) according to the manufacturer instructions. The DNA concentration and purity was measured with the use of nanodrop spectrophotometer. For the control group, a group of 55 apparently healthy subjects were recruited (30 male and 25 female), after getting their formal consent, a sample of 5 milliliter of venous blood was collected from each and the DNA was extracted from each sample. For the *MTHFR* gene polymorphism study, the *MTHFR* C677T was genotyped using the PCR-RFLP method according to Frosst *et al* (1995)with minor modifications. The primers targeting the *MTHFR* gene sequence flanking the regions close to C677T mutation prone point were designed with the help of NCBI software and provided by (Jena Bioscience, Germany), the primers were forward (5' GCCTCTCCTGACTGTCATCC3') and reverse 5'GGAGCTTATGGGCTCTCCTG3'). PCR of 14.4µl volume was conducted in 0.5 mL size PCR tubes consisting of 10 µl ready to use PCR master mix from Applied Bioscience, (containing *Taq* polymerase, dNTPs and PCR buffer), 0.8 µl each of the forward and reverse primers and 2.8 µl (40-60 ng) of genomic DNA from each sample. The PCR thermal cycling has been carried out in a thermal cycler (Applied bioscience) according to Abdul K. Siraj *et al*. 2008 with a few modifications, briefly the thermal conditions and cycling durations composed of: denaturation at 95°C for 5 minutes, followed by 40 cycles, denaturation at 95°C for 30 seconds, annealing at 66°C for 30 seconds, extension at 72°C for 30seconds, and a final extension at 72°C for 7 minutes(Abdul K. Siraj *et al*. 2008). The PCR products were digested

with *Hinf*I restriction enzyme in a total volume of 15.52μl consisted of: 14.4 μl PCR product, 1 μl restriction buffer (Promega, USA), 0.12 μl bovine serum albumin and 0.2 μl *Hinf*I restriction enzyme (Jena Bioscience, Germany). The digestion mix was incubated at 37 °C for 24 hours in a shaking water bath. The DNA fragments resulted from *Hinf*I enzymatic digestion were separated on a 2.0% agarose gel electrophoresis and observed by UV light.

2.2. Statistical analysis

Unpaired Student's *t* test was used to compare the differences of genotype and allelic frequencies between the cases and controls. The odds ratio and 95% confidence interval was depended to provide a measure for the strength of association. The SPSS statistical package (version 11.0)was used to calculate all of the statistical analyses at significant p value< 0.05 (Abdul K. Siraj *et al*. 2008).

3. RESULTS AND DISCUSSION

Study population characteristics are shown in Table 1. In this study, a total of 52 thyroid cancer cases and 55 healthy controls are involved. The thyroid cancer cases consisted of 18 (34.6%) males and 34 (65.4 %) females, their age mean was 42.41 years with age median of 41 years. The cases were 3 (5.8%) anaplastic carcinoma, 43 (82.7%) papillary carcinoma, 4 (7.7%) follicular carcinoma and 2 (3.8%) medullary carcinoma. The control group consisted of 30 (54.5%) males and 25 (45.5%) females, their age mean was 43.6 years. There was no significant difference (p value > 0.05) between the age means of both of the thyroid cancer group and the control group. There was statistically significant effect of gender on the rate of thyroid cancer cases, the female rate was significantly higher than the male thyroid cancer cases. The oligonucleotide primers used in the current study that target the *MTHFR* gene are producing a 254 base pair DNA band on agarose gel, for the RFLP, the *hinf*I restriction enzyme cuts the PCR products and yields two DNA bands on agarose gel with 147 and 107 bp size (figure 1).

The distribution of MTHFR C677T genotypes among the thyroid cancer patients and the healthy controls groups is shown in table 2. The frequency of MTHFR (C677T) CC, CT heterozygous and TT homozygous variants among thyroid cancer patients were 59.6%, 15.4% and 25% respectively, and the CT +TT combined variants were 40.4%. There was statistical significant difference between the MTHFR CC variants and MTHFRC677T (CT,TT) variants (P ‹ 0.005)

Table 2 also shows the distributions for MTHFR C677T genotype variants among healthy control group, the frequency of CC, CT heterozygous and TT homozygous variants was 85.%, 3.6% and 10.9% respectively, and the frequency of combined CT heterozygous +TT homozygous variants among the healthy controls was 14.5%. Using unpaired Student's *t* test, the odds ratio (Ors) and confidence intervals (CIs) to analyze the effect of CT genotype on the frequency of thyroid cancer frequency, it is shown that CT genotype has affected the frequency of the thyroid cancer cases among the case group, however the effected did not reach the statistical significance (OR = 0.9; 95% CI = 0.3-2.6; *t* test = 0.13; P = 0.89). Comparing the TT genotype variants between the disease group and the healthy control group, there was statistically no effect of the *MTHFR* C677T (TT genotype) mutation on the rate of the disease in the thyroid cancer group compare to the healthy group ((OR = 1.6; 95% CI = 0.6-4.45; *t* test = 1.02; P = 0.29). Comparison of the overall CT+TT combination genotype variants in thyroid cancer group with those in the healthy

control group, it is found that there was no significant effect of *MTHFR* C677T mutation on the frequency of thyroid cancer in the case group (OR = 1.3; 95% CI = 0.6-2.8; *t* test = 0.6; P = 0.533).

The frequency of the *MTHFR* C677T mutation (CT and TT genotypes) distribution regarding the gender in both the thyroid cancer and the healthy group is shown in table 3. In thyroid cancer group, the frequency of *MTHFR* C677T (CT,TT) in the females and males was 57.1% and 42.9% respectively, and in the healthy control group it was 47.4% in the females and 52.6% in the males. The unpaired Student's *t* test showed that there was no significant difference between both of the groups regarding gender, also there was no significant effect of gender on the frequency of *MTHFR* C677T in the same group.

The present case-control study that has been conducted on 52 thyroid cancer patients and 55 healthy controls, to the best of our knowledge, this the first study that examines the association between the thyroid cancer and *MTHFR* C677T polymorphism in Kurdistan region. Our findings demonstrate a significant effect of the gender on the rate of thyroid cancer among the patients group, there was a statistical significant difference between the males and female developed thyroid cancer, since the female rate of the disease was higher significantly among the disease group. Thyroid cancer is the most common malignancy of the endocrine system and the seventh most common malignancy in women (Ortega *et al*, 2004). Our results are consistent with the overall database of the incidence of thyroid cancer across different geographic and ethnic populations (Curado *et al*, 2007). The histologic subtypes of thyroid cancer are affected by gender variation. Anaplastic thyroid cancer and medullary thyroid cancer, which are the most aggressive types of thyroid cancer, are shown to have similar rates of incidence in men and women. Although, differentiated thyroid cancer such as follicular thyroid cancer and papillary thyroid cancer, are found to be more common in woman, since, the fluctuation of sex hormones during a woman's menstrual cycle and pregnancy has been hypothesized as the reason for the gender disparity in papillary thyroid cancer. In particular, the peak incidence of papillary thyroid cancer has been observed in women aged 40–49 years, this being the age group at which most women approach or enter menopause (Ortega J. *et al*, 2004; Kilfoy BA. *et al*, 2009).

. Other researchers have found that this disparity in gender is age-dependant, when women are found to have an earlier age of thyroid cancer onset but in men it is more aggressive at diagnosis. Moreover, in many studies, male gender is associated with a lower survival rate and higher mortality (Gilliland *et al*, 1997; Kilfoy *et al*,2009). Also in the present study, we found no significant contribution of *MTHFR* C677T (CT+TT variants) mutation in thyroid cancer in the disease group, since the *MTHFR* wild type CC genotype rate (59.6%) was significantly higher than the mutated CT, TT variants rate (40.4%). These results are in consistent with the results obtained by Abdul K. *et al* (2008) when they found that *MTHFR* polymorphism is of no importance to the thyroid cancer (Abdul K. Siraj *et al*. 2008). From the current results, it seems that subjects with *MTHFR* C677T single nucleotide mutation have about 1.5 times less risk getting thyroid cancer than those with the wild genotype of *MTHFR* (CC). Comparing our results with those obtained by others who investigated the association of *MTHFR* C677T polymorphism with other various tumors, they are consistent to an extent that no one strictly confirmed the association of the *MTHFR* C677T with thyroid cancer development. In an

Indian Caucasian population study, it has been shown that individuals with 677 C>T substitution in the *MTHFR* gene have a 3.5 fold lower risk of breast cancer (OR = 3.41, 95%CI = 3.1–3.7, P<0.02) (Mir *et al*, 2008). Also Cui et al (2011) found that the co- existence of 677 TT homozygous with 677 CT heterozygous of *MTHFR* shown to confer a protection effect against the risk of squamous cell carcinoma (Cui *et al*, 2011). But in some other studies, the lack of association between *MTHFR* variants and the risk of breast cancer has been reported in south Indian populations (Kalyankumar *et al*, 2006; Alberg *et al*, 2000). Furthermore, Cui et al (2011) found that the *MTHFR* 677 CT and TT variants conferred a weak protection from lung cancer (Cui *et al*, 2011). Also, there are conflicting data regarding the role of *MTHFR* in cervical cancer susceptibility and presentation of cervical cancer have been reported by series of case-control studies (Prasad *et al*, 2011; Kohaar *et al*, 2010; Nandan *et al*, 2008; Zoodsma *et al*, 2005; Lambropoulos *et al*, 2003). In table 3, the gender adjusted differences between both the thyroid cancer group and the healthy control group, there was no significant difference regarding the *MTHFR* C677T genotypes between both genders in both groups, in contrast to the findings in the current study a meta analysis conducted by Yan *et al* (2014), they found that *MTHFR* C677T polymorphism is associated with thyroid cancer both in Caucasians and Asians (Yan *et al*, 2014), this could be due to the larger population size they

compared in many studies as a meta analysis. Worldwide studies have emphasized that folate levels exerts a protective role in a different cancers. Based on the importance of *MTHFR* in maintaining the level of folate, the *MTHFR C677T* variants polymorphism has been explored in various types of cancer, included colorectal, thyroid, breast, ovarian, and cervical cancer (Prasad *et al*, 2011). Overall, our results did not support a statistical association of the *MTHFR* C677T polymorphism with the risk of developing thyroid cancer neither gender association with the gene variants, other researchers also stated that the *MTHFR* C677T is not a potential risk factor for developing thyroid cancer, also Parsad *et al* (2011) stated that the C677T mutation in the *MTHFR* gene plays as a risk factor for colorectal cancer but not the cervical, thyroid, and breast cancers and the variants are not gender-specific (Prasad *et al*, 2011). The small sample size investigated in this study is a limitation that could be affecting on the discrepancy of the results. Moreover, further studies with larger sample size of different populations are necessary to investigate the molecular contribution of *MTHFR* polymorphism in the thyroid cancer molecular pathology and its association with age and gender.

Table1. Characteristics of the study population

		Male	Female	Age range (year)	Age mean (Year)	Age median (Year)
Thyroid cancer cases	(*n*=52)	18(34.6%)	34(65.4%)	19-72	42.41	41
Anaplastic carcinoma	3 (5.8%)	1 (33.3%)	2 (66.7%)			
Papillary carcinoma	43(82.7%)	14(26.9%)	29(55.8%)			
Follicular carcinoma	4 (7.7%)	1 (1.9%)	3 (5.8%)			
Medullary carcinoma	2 (3.8%)	2 (3.8%)	0 (0.0%)			
Healthy Controls (***n*=55**)		30(54.5%)	25(45.5%)	20-70	43.6	43

Table2. MTHFR C677T distribution and their genotype (CT, TT and CT+TT) association with thyroid cancer

MTHFR C677T	Thyroid cancer *n* (%)	Control *n* (%)
CC (Wild type)	31 (59.6%)	36 (65.5%)
CT (Heterozygous)	8 (15.4%)	10 (18.2%)
TT (Homozygous)	13 (25%)	9 (16.3%)
CT+TT combination	21 (40.4%)	19 (34%)

Table3. Gender association with MTHFR C677T in thyroid cancer and controls

Group	MTHFR C677T (CT, TT genotypes) *n*(%)
Thyroid cancer group (*n*=52):	
- Females	12 (57.1%)
- Males	9 (42.9%)
Healthy control group (*n*=55):	
- Females	9 (47.4%)
- Males	10 (52.69)
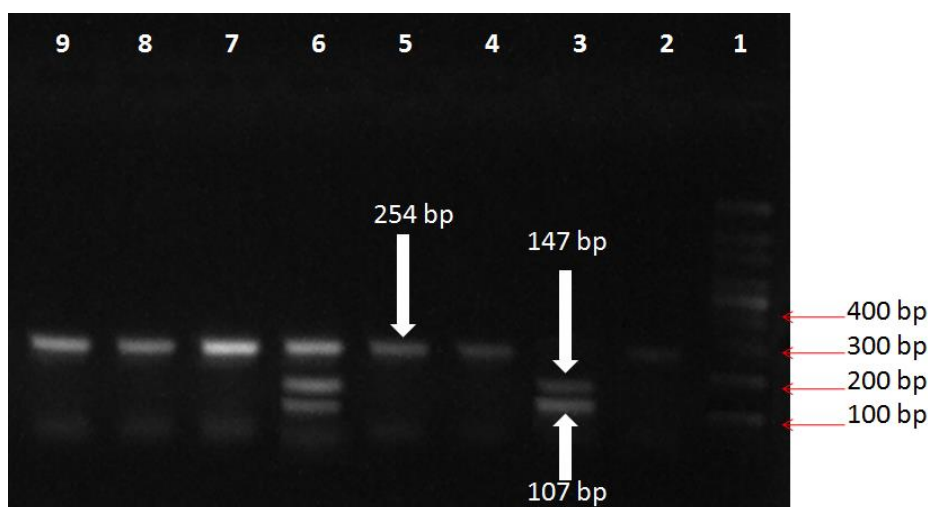
Fig.1: PCR- RFLP analysis: An agarose gel electrophoresis (2%) illustrating restricted fragments of *MTHFR* polymorphism (C677T). Lane1: 100 bp DNA ladder. Lane 2,4,5,7, 8 and 9 (254 bp fragment): *MTHFR* C/C wild genotype. Lane 3 (147 & 107 bp): *MTHFR* T/T homozygous genotype. Lane 6 (257, 147 & 107 bp): *MTHFR* C/T heterozygous genotype.

4. CONCLUSIONS

Our results in the present study did not support a statistical association of the *MTHFR* C677T gene polymorphism variants with the

risk of developing thyroid cancer neither with gender nor age adjustment.

Conflict of Interest

Nothing to declare.

REFERENCES

ABDUL K SIRAJ, MUNA IBRAHIM, MAHA AL-RASHEED, JEHAD ABUBAKER, RONG BU, SHAKAIB U *et al*. 2008. Polymorphisms of selected Xenobiotic Genes contribute to the development of Papillary Thyroid Cancer susceptibility in Middle Eastern population. BMC Medical Genetics, 9,61.

ALBERG AJ, SELHUB J, SHAH KV, et al. 2000. The risk of cervical cancer in relation to serum concentrations of volate, vitamin B$_{12}$, and homocysteine. Cancer Epidemiol Biomarkers Prev, 9, 761–4.

CHOU YC, WU MH, YU JC, LEE MS, YANG T. 2006. Genetic polymorphisms of the methylenetetrahydrofolate reductase gene, plasma folate levels and breast cancer susceptibility: a case-control study in Taiwan. Carcinogenesis, 27, 295–2300.

COHEN Y, et al. 2003. BRAF mutation in papillary thyroid carcinoma. J Natl Cancer Inst, 95, 625–627.

CUI LIAN-HUA, MIN-HO SHIN, HEE NAM KIM, HYE-RIM SONG, JIN-MEI PIAO, SUN-SEOG KWEON, JIN-SU CHOI, WOO-JUN YUN, YOUNG-CHUL KIM, IN-JAE OH, KYU-SIK KIM CUI *et al*. 2011. Methylenetetrahydrofolate reductase C677T polymorphism in patients with lung cancer in a Korean population. Medical Genetics, 12:28.

CURADO MP, EDWARDS B, SHIN HR *et al*. 2007. (Eds). *Cancer Incidence in Five Continents.* IARC Scientific Publications, *4,* 160. IARC.

DELELLIS, RA.; LLOYD, RV.; HEITZ, PU.; ENG, C. 2004. World Health Organization Classification of Tumours. Pathology And Genetics Of Tumors Of Endocrine Organs. IARC Press.

DONGHI R, et al. 1993. Gene p53 mutations are restricted to poorly differentiated and undifferentiated carcinomas of the thyroid gland. J Clin Invest., 91, 1753.

FAGIN JA, et al. 1993. High prevalence of mutations of the p53 gene in poorly differentiated human thyroid carcinomas. J Clin Invest.,91, 179–184.

FROSST P, BLOM HJ, MILOS R, GOYETTE P, SHEPPARD CA, MATTHEWS RG, BOERS GJ, DEN HEIJER M, KLUIJTMANS LA, VAN DEN HEUVEL LP, et al. 1995. A candidate genetic risk factor for vascular disease: a common mutation in methylenetetrahydrofolate reductase. Nature genetics, 10(1), 111-113.

FUKUSHIMA T, et al. 2003. BRAF mutations in papillary carcinomas of the thyroid. Oncogene., ;22, 6455–6457.

GARCIA-ROSTAN G, et al. 1999. Frequent mutation and nuclear localization of β-catenin in anaplastic thyroid carcinoma. Cancer Res, 59, 1811–1815.

GARCIA-ROSTAN G, et al. 2001. β-catenin dysregulation in thyroid neoplasms: down-regulation, aberrant nuclear expression, and CTNNB1 exon 3 mutations are markers for aggressive tumor phenotypes and poor prognosis. Am J Pathol., 158, 987–996.

GILLILAND FD, HUNT WC, MORRIS DM, KEY CR. 1997. Prognostic factors for thyroid carcinoma. A population-based study of 15,698 cases from the Surveillance, Epidemiology and End Results (SEER) program 1973–1991. Cancer, 79, 564–573.

HEMERLY JP, BASTOS AU, CERUTTI JM. 2010. Identification of several novel non-p. R132 IDH1 variants in thyroid carcinomas. Eur J Endocrinol,163, 747–755.

HOSSEINI M, HOUSHMAND M, EBRAHIMI A. 2011. MTHFR polymorphisms and breast cancer risk. Arch Med Sci, 7, 134–137.

HOU P, LIU D, XING M. 2007. Functional characterization of the T1799-1801del and A1799-1816ins BRAF mutations in papillary thyroid cancer. Cell Cycle, 6:377–379.

HOWLADER, N., et al. 2007. SEER Cancer Statistics Review 1975–2009. National Cancer Institute. 2012. [online], http://seer.cancer.gov/csr/1975_2009_pops09

IRAQI CANCER REGISTRY. 2004. Results of Iraqi cancer registry 1976-2004. World health organization, Ministry of Health (WHO), Baghdad, lraq.

JAMIL A, et al. 2011. Global cancer statistics. CA Cancer J Clin, 61,69–90.

KALYANKUMAR C, JAMIL K. 2006. Methylenetetrahydrofolate Reductase (MTHFR) C677T and A1298C Polymorphisms and Breast Cancer in South Indian Population. International Journal of Cancer Research, 2, 143–151.

KILFOY BA, DEVESA SS, WARD MH, et al. 2009. Gender is an age-specific effect modifier for papillary cancers of the thyroid gland. Cancer Epidemiol. Biomarkers Prev,18,1092–1100. [PubMed]

KOHAAR I, KUMAR J, THAKUR N, HUSSAIN S, NIYAZ MK, et al. 2010. Homocysteine levels are associated with cervical cancer independent of methylene tetrahydrofolate reductase gene (MTHFR) polymorphisms in Indian population. Biomarkers.,15, 61–68.

Kotsopoulos J, Zhang WW, Zhang S, McCready D, Trudeau M, Zhang P, et al. .2008. Polymorphisms in folate metabolizing enzymes and transport proteins and the risk of breast cancer. Breast Cancer Res Treat; 112, 585–593.

LAMBROPOULOS AF, AGORASTOS T, FOKA ZJ, CHRISAFI S, CONSTANTINIDIS TC, *et al*. 2003. Methylenetetrahydrofolate reductase polymorphism C677T is not associated to the risk of cervical dysplasia. Cancer Letters, 191, 187–191 .

LANGEVIN SM, LIN D, MATSUO K, GAO CM, TAKEZAKI T, STOLZENBERG-SOLOMOM RZ, et al. 2009. Review and pooled analysis of studies on MTHFR C677T polymorphism and esophageal cancer. Toxicol Lett, 184, 73–80.

LAVERDIERE C, CHIASSON S, COSTEA I, MOGHRABI A, KRAJINOVIC M. 2002. Polymorphism G80A in the reduced folate carrier gene and its relationship to methotrexate plasma levels and outcome of childhood acute lymphoblastic leukemia. Blood, 100,3832–4.

LEE SA, KANG D, NISHIO H, LEE MJ, KIM DH, HAN W, et al. Methylenetetrahydrofolate reductase polymorphism, diet, and breast cancer in Korean women. Exp Mol Med, 36, 116–121.

LUND E, GALANTI MR. 1999. Incidence of thyroid cancer in Scandinavia following fallout from atomic bomb testing: an analysis of birth cohorts. Cancer Causes Control, 10:181–7.

MACIS D, MAISONNEUVE P, JOHANSSON H, BONANNI B, BOTTERI E, IODICE S, et al. 2007. Methylenetetrahydrofolate reductase (MTHFR) and breast cancer risk: a nested-case-control study and a pooled meta-analysis. Breast Cancer Res Treat, 106,263–271.

MATSUO K, HAMAJIMA N, SUZUKI R, OGURA M, KAGAMI Y, TAJI H, YASUE T, MUELLER NE, NAKAMURA S, SETO M, MORISHIMA Y, TAJIMA K. 2004. Methylenetetrahydrofolate reductase gene (MTHFR) polymorphisms and reduced risk of malignant lymphoma. Am J Hematol,77,351–7

MIR MM, DAR JA, DAR NA, DAR MS, SALAM I. 2008. Combined impact of polymorphism of folate metabolism genes; glutamate carboxypeptidase, methylene tetrahydrofolate reductase and methionine synthase reductase on breast cancer susceptibility in Kashmiri women. Int J Health Sci,; 2, 3–14.

MURUGAN AK, BOJDANI E, XING M. 2010. Identification and functional characterization of isocitrate dehydrogenase 1 (IDH1) mutations in thyroid cancer. Biochem Biophys Res Commun, 393, 555–559.

MURUGAN AK, DONG J, XIE J, XING M. 2011. Uncommon GNAQ, MMP8, AKT3, EGFR, and PIK3R1 mutations in thyroid cancers. Endocr Pathol, 22, 97–102.

MURUGAN AK, XING M. 2011. Anaplastic thyroid cancers harbor novel oncogenic mutations of the *ALK* gene. Cancer Res. 71, 4403–4411.

NANDAN NK, WAJID S, BISWAS S, JUNEJA SS, RIZVI M, *et al*. 2008. Allelic variations in 5, 10-methylenetetrahydrofolate reductase gene and susceptibility to cervical cancer in Indian women. Drug Metab Lett., 2, 18–22 [PubMed]

ORTEGA J, SALA C, FLOR B, LLEDO S. 2004. Efficacy and cost–effectiveness of the UltraCision harmonic scalpel in thyroid surgery: an analysis of 200 cases in a randomized trial. J. Laparoendosc. Adv. Surg. Tech. A, 14, 9–12. [PubMed]

OTHMAN RT, ABDULLJABAR R, SAEED A, KITTANI SS, SULAIMAN HM, MOHAMMED SA, et al. 2011. Cancer Incidence Rates in the Kurdistan Region/Iraq from 2007-2009. APJCP, 12, 1261-64.

PITY IS, SALIH AM, HASSAN N. 2015. BRAF^{V600}gene mutation in thyroid cancer in Duhok-Iraq. DMJ, 1, 30-6.

PRASAD VVTS, WILKHOO H. Association of the functional polymorphism C677T in the methylenetetrahydrofolate reductase gene with colorectal, thyroid, breast, ovarian, and cervical cancers. Onkologie, 34, 422–426

RON E, LUBIN JH, SHORE RE, MABUCHI K, MODAN B, POTTERN LM, SCHNEIDER AB, TUCKER MA, BOICE JD., JR. 1995. Thyroid cancer after exposure to external radiation: a pooled analysis of seven studies. Radiat Res, 141, 259–77.

TROVISCO V, et al. 2005. Type and prevalence of BRAF mutations are closely associated with papillary thyroid carcinoma histotype and patients' age but not with tumour aggressiveness. Virchows Arch, 446, 589–595.

TUTTLE RM, et al. 2010. Thyroid carcinoma. J Natl Compr Canc Netw, 8, 1228–1274.

XING M. 2005.BRAF mutation in thyroid cancer. Endocr Relat Cancer, 1, :245–262.

YAN Y, HAN F, FU H, XIA W, QIN X. 2014. Association between MTHFR C677T polymorphism and thyroid cancer risk: a meta-analysis. Tumour Biol., ;35(8), 7707-12

ZOODSMA M, NOLTE IM, SCHIPPER M, OOSTEROM E, VAN DER STEEGE G, *et al*. 2005. Methylenetetrahydrofolate reductase (MTHFR) and susceptibility for (pre)neoplastic cervical disease. Hum Genet, 116, 247–254